



Rheology of Cross-linked Polymer Networks

Jensen, Mette Krog

Publication date:
2010

Document Version
Publisher's PDF, also known as Version of record

[Link back to DTU Orbit](#)

Citation (APA):
Jensen, M. K. (2010). *Rheology of Cross-linked Polymer Networks*. Technical University of Denmark.

General rights

Copyright and moral rights for the publications made accessible in the public portal are retained by the authors and/or other copyright owners and it is a condition of accessing publications that users recognise and abide by the legal requirements associated with these rights.

- Users may download and print one copy of any publication from the public portal for the purpose of private study or research.
- You may not further distribute the material or use it for any profit-making activity or commercial gain
- You may freely distribute the URL identifying the publication in the public portal

If you believe that this document breaches copyright please contact us providing details, and we will remove access to the work immediately and investigate your claim.

Rheology of Cross-linked Polymer Networks



Mette Krog Jensen

Ph.D. Thesis

2010

Rheology of Cross-linked Polymer Networks



METTE KROG JENSEN

DEPARTMENT OF CHEMICAL AND BIOCHEMICAL
ENGINEERING

TECHNICAL UNIVERSITY OF DENMARK

A THESIS SUBMITTED FOR THE DEGREE OF

Doctor of Natural Philosophy

OCTOBER 2009

Copyright © Mette Krog Jensen 2010
ISBN 978-87-92481-19-1

Printed in Denmark by
WWW.FRYDENBERG.DK
Baldersgade 12 - 16
DK-2200 Copenhagen N

Rheology of Cross-linked Polymer Networks

METTE KROG JENSEN

October 2009

Department of Chemical and Biochemical Engineering
Technical University of Denmark
DK-2800 Kongens Lyngby, Denmark

Preface

This thesis presents the results of my Ph.D. project carried out at the Danish Polymer Center (DPC), Department of Chemical and Biochemical engineering, Technical University of Denmark (DTU). The work was performed during the period from November 2006 to November 2009, under supervision of Professor Ole Hassager and Associate Professor Anne Ladegaard Skov, both at DTU Chemical and Biochemical Engineering and Dr. Anders Bach at Coloplast A/S. This project was financed 1/3 by the Technical University of Denmark, 1/3 by the Graduate School of Polymer Science and finally 1/3 by Coloplast A/S.

I have truly enjoyed my three years as a Ph.D. student, and have many to thank for that. First and foremost I would like to thank my three advisors, Ole Hassager, Anne Ladegaard Skov and Anders Bach.

To my supervisor, Ole Hassager, I would like to express my gratitude for giving me the opportunity to carry out this study at the Department of Chemical and Biochemical Engineering. I am very grateful for his inspiring guidance and helpful discussions, and for opening the doors for an international network, by encouraging me to participate in international conferences.

A thank to my co-advisor, Anders Bach, is given for his encouragement and guidance in experimental work. It has been a pleasure to learn from his overview within experimental rheology, and his endless amount of new ideas for new experimental procedures.

I am also truly grateful for the help, continuous encouragement and guidance from my other co-advisor, Anne Ladegaard Skov. I have truly enjoyed our meetings about network structures, seniorities, gels etc.

I would also like to express my gratitude to Associate Professor Henrik Koblitz Rasmussen for his enormous support within extensional rheometry. I have gained a lot from his enthusiastic approach to science and from our long discussions about rheology. Last but not least, it is also nice to have somebody who can tell you when not to have lunch break.

A special thank should also be given to Henning Koldbech from the departmental workshop, who has been the front runner in designing a new, and invaluable apparatus for my experimental work.

I would like to address my sincere gratitude to Professor Jay D. Schieber at Illinois Institute of Technology (IIT) for taking me into his group for 5 months, and giving me a new perspective on rheology. Also in this regard, I will thank the whole group at IIT who gave me a warm welcome to Chicago, in particular I

PREFACE

would like to mention Professor David Venerus, for encouraging comments and debates, and Renat Khaliullin and Teresita Kashyap, with whom I had many productive discussions (both scientific and not so scientific). In the realization of my external stay at IIT I received 5 grants, which I would like to mention here: *Ostenfelds fond*, *Aage Corrits legat*, *Otto Mønstedts fond*, *Knud Højgaards Fond* and *Fabrikant P.A. Fiskers Fond*. Additional support was provided by the Army Research Lab Grant W911NF-08-2-0058.

A thank should also be directed at my officemates at DPC, José Manuel Marín Román, Yanwei Wang and Kaijia Yu it has been a true pleasure to work with you all. To José thanks for the coffee.

To Kim Chi Szabo, thank you for helping me with polymer characterization and general lab guidance.

I have in general benefited from the many-body interactions with all the fellow students and staff members at DPC as well as at IIT, and I wish to express my thanks to all of them.

To my Tue, Thanks for supporting me during all the years, and for encouraging me during frustrating periods. Also a huge thank to my family and friends for their support.

Kgs. Lyngby, October

Mette Krog Jensen

Contents

Preface	iii
Synopsis	vii
Dansk Resumé	ix
1 Introduction	1
1.1 Pressure-Sensitive Adhesives	1
1.2 Peel	2
1.3 Polymer Networks	2
1.3.1 Seniority Principle	8
1.4 Rheology	11
1.4.1 Background	11
1.4.2 Dynamic Mechanical Analysis	12
1.4.3 Elongational Measurements	14
1.5 An Outline of this Thesis	16
2 Linear Rheology of Cross-linked PPO as a PSA	19
2.1 Introduction	19
2.2 Experimental	21
2.2.1 Sample Preparation	21
2.2.2 Linear Viscoelasticity	22
2.2.3 Peel	23
2.3 Results and Discussion	24
2.3.1 Small amplitude Oscillatory Shear Data	24
2.3.2 Peel Data	26
2.3.3 Dimensional Analysis	27
2.3.4 Viscoelasticity of PSAs	31
2.4 Conclusion	31
3 Planar Elongation of Soft Polymeric Networks	35
3.1 Introduction	35
3.2 The Planar Elongation Fixture	38
3.3 Sample Preparation and Characterization	39

3.4	Nonlinear Properties	41
3.5	Numerical modeling	45
3.6	Results and Discussion	47
3.6.1	Diameter Measurements	48
3.6.2	Particle Tracking	49
3.6.3	Numerical Results	51
3.6.4	Measured Stresses	53
3.7	Conclusion	55
4	Reversible Planar Elongation of Soft Polymeric Networks	57
4.1	Introduction	58
4.2	Materials and Methods	61
4.2.1	Samples	61
4.2.2	Experimental Setup	63
4.2.3	Nonlinear Analysis	63
4.2.4	Numerical Modeling	65
4.3	Results and Discussion	65
4.3.1	Diameter Measurements	66
4.3.2	Measured Stresses	66
4.4	Conclusion	72
5	Self-consistent modeling of entangled networks	75
5.1	Introduction	76
5.2	The Discrete Slip-link Model	78
5.2.1	Ideal Entangled Network	78
5.2.2	Entangled Network Strands and Entangled Dangling Strands	82
5.2.3	Constraint Dynamics spectrum	84
5.3	Results	87
5.3.1	BSW spectrum	87
5.3.2	Ideal Entangled Network	88
5.3.3	Entangled Network with Dangling Strands	91
5.4	Conclusion	99
6	Summarizing chapter	101
6.1	Concluding Remarks	101
6.2	Future Work	103
Appendix:		
Joint Author Declarations		105

Synopsis

This thesis deals with the mechanical and adhesive properties of soft polymeric networks, that is; polymer networks with different amounts of imperfections. These properties are of practical importance in a variety of applications including drug-delivery systems, implants and adhesives. Our primary interest is to provide an understanding between the sample preparation, and the mechanical properties of the end product.

At first we consider the adhesive properties by linking linear viscoelastic data to the peel force. The peel force is measured for a variety of network samples, where the interesting parameters are the stoichiometric imbalance of the networks, the molecular weight of the polymer and the functionality of the cross-linker. We relate the peel force to the fundamental linear viscoelastic parameters, and find an empirical relation. In particular when the elastic response is dominating, the relation seem independent on bulk composition, *i.e.*, stoichiometric imbalance, molecular weight and cross-linker functionality. While nonlinear effect becomes more important as the viscous character of the samples becomes more dominant.

The nonlinear network properties are measured using a filament stretch rheometer. A new planar elongation fixture has been designed as an add-on for this rheometer to measure planar elongation, and it is intended to exploit the sticky nature of the soft networks. The concept is to elongate an annulus without deforming the cylindrical probe. It is found to be a strong tool for measuring planar elongation on soft networks, since uniform planar elongation is obtained by simple means, that is; by solely adjusting the initial sample geometry.

The planar elongation fixture is used to measure steady and reversible planar elongational stresses. The results are analyzed with a finite element method (FEM), which is based on a combination of elastic and viscoelastic models described within the framework of the K-BKZ constitutive equation. A comparison between data and the FEM results show that the deformation on the cylindrical probe is highly dependent on the nonlinear strain behavior, in particular the weight on the lower convected strain tensor.

While steady elongation measurements give information about the strain-hardening nature of the materials, little information is obtained about the elastic nature. The reversible flow measurements give information about the amount of work stored in the sample during a loading and unloading cycle, and the elastic

storage is nearly independent of frequency. Additionally the softer the network, the more work is needed during the deformation cycle, which is because the networks become less elastic.

To interpretate our experimental results, we seek a molecular based model, to analyze the structural properties of the networks. We use a self-consistent mean-field slip-link model, to study the mechanical behavior of networks. We model both ideal entangled networks and entangled networks with dangling strands. The first approach gives a very basic description of the entanglement effect on the relaxation modulus, while we get a more diverse picture when adding dangling strands. Even though the network with dangling strands is an idealized picture of real networks, we are able to extract some important information about the network dynamics.

Dansk Resumé

Denne afhandling beskæftiger sig med de mekaniske egenskaber og klæbeevner for bløde polymere netværk, som kort beskrevet er; polymer netværk med forskellige grader af støkiometrisk ubalance. Disse egenskaber er af praktisk betydning i en række applikationer, herunder “drug-delivery”, implantater og plastre. Vores primære interesse er at give en forståelse mellem sammensætningen af prøverne, og de mekaniske egenskaber af slutproduktet.

For det første betragter vi klæbeevnerne ved at sammenholde lineær viskoelastiske data til peel data. Peel kraften er målt for en række netværk prøver, hvor de interessante parametre er den støkiometriske ubalance, molekylvægten af polymeren og funktionaliteten af kryds-binderen. Vi relaterer peel kraften til de linear viskoelastiske data målt ved peel frekvensen, og foreslår en empirisk sammenhæng. Især når det elastiske respons er dominerende, synes sammenhængen uafhængig af bulk-sammensætningen, dvs., den støkiometriske ubalance, molekylvægt og kryds-binder-funktionalitet. Mens ikke-lineære egenskaber bliver dominerende når det mekaniske respons bliver mere viskøst.

De ikke-lineære egenskaber måles med et filament stræk rheometer. Et nyt plan forlængelses fiksture er udformet som et add-on til dette rheometer, og er designet til at udnytte den klæbende egenskab af bløde netværk. Konceptet er at forlænge en hul cylinder uden at deformere den cylindriske form. Det viser sig at være et stærkt værktøj til at måle plan stræk på bløde netværk, da den ønskede deformation opnåes ved blot at justere de oprindelige dimensioner p prøven.

Plan forlængelses fiksturet bruges til at måle både stationær og reversibel plan forlængelse. Resultaterne analyseres med en Finite Element Metode (FEM), som er baseret på en kombination af elastiske og viskøse modeller beskrevet indenfor den K-BKZ konstitutive model. En sammenligning mellem data og FEM resultater viser, at materialerne er næsten neo-Hookean, og at deformation på den cylindriske form er meget afhængig af den ikke-lineære deformations tensor.

Mens stationær forlængelse giver oplysninger om graden af “strain-hardening” i materialerne, giver reversible målinger oplysninger om mængden af arbejde lagret i prøverne afhængigt af deformation og frekvens. På grund af materialernes dominerende elastiske karakter er energilagringen nær frekvensuafhængig.

Vi søger afslutningsvis en molekyl baseret model til at analysere de strukturelle egenskaber af netværkene. Slip-link modellen har vist sig anvendelig

til at studere den mekaniske opførsel af en række polymere systemer, som f.eks. lineære og forgrenede polymere, hvorfor vi benytter den til at analysere polymer netværk. Vi modellerer både ideelt sammenviklede (“entangled”) netværk og sammenviklede netværk med frie ender. Den første metode giver en meget basal beskrivelse af sammenviklingernes effekt på det relaxerende modul. Til trods for at netværket med frie ender er et idealiseret billede af virkelige netværk, giver resultaterne vigtige oplysninger om netværkenes dynamik.

List of Figures

1.1	Illustration of a cross-linked network. The black dots mark the cross-linkers. The circles mark the ends of dangling structures, <i>i.e.</i> structures that are connected to the network in one end only. The thick lines represent the soluble polymeric structures.	3
1.2	Inactive (A) versus active loops (B)	3
1.3	Illustration of temporary entanglements. (A) between two elastically active network strands and (B) between a network strand and a dangling strand and finally (C) stationary entanglements between two networks strands	4
1.4	Weight fractions of soluble (SS), network (NS) and dangling strands (DS) versus extent of reaction, p , for a three-functional cross-linker ($f = 3$).	6
1.5	Illustration of a network without loops on a Cayley tree with tri-functional cross-linkers.	7
1.6	Tetra-functional ($f = 4$) cross-linked network with dangling structures of different degree of branching. The branched strands are labeled with their respective seniority when looking from the root of the dangling strands to thei furthest branch end. The seniority counting fails for elastically active strands.	8
1.7	Bidirectional seniority distribution for different extent of reactions, p , of the linear polymer on a (A) linear-log scale and (B) log-log scale.	10
1.8	Relaxation time spectra for $p = 0.4$ and 0.6 . τ is made dimensionless with the Rouse time, τ_e , and $\tau(1) = 1$	11
2.1	A sketch of the linear vinyl terminated PPO.	21
2.2	A sketch of the f -functional polysiloxane cross-linker. At least three of the R-groups in the squared bracket are hydrogen such that $f \geq 3$. The rest of the groups are each independently selected from C_{1-12} -alkyl, C_{3-8} -cycloalkyl, C_{6-14} -aryl and C_{7-12} -arylalkyl.	21
2.3	Sketch of a 90° peel test setup, side-view of the xz -plane.	24

2.4	Dynamic moduli for SX.A1B2.03 obtained from SAOS experiments. Crosses represents the storage modulus while circles represents the loss modulus. The solid lines represent a fit of equations 2.6 and 2.7 to the data. The dashed lines represent the viscous and elastic contributions to the storage modulus respectively.	25
2.5	(A) G_0 (B) S and (C) n vs. r obtained from a least square fit of equations 2.6 and 2.7 to experimental SAOS data.	27
2.6	The peel force measured for the SX.A1B2 series. The force is plotted vs. sample thickness, d , and shown for each peel rate, V_{peel}	28
2.7	The measured peel force for the SX.A1B2 series divided by the sample dimensions, d and W . It is plotted vs. the loss modulus measured at the peel frequency, $G''(\omega_{peel})$	29
2.8	The normalized peel force vs. the loss tangent measured at the peel frequency. The data is from the SX.A1B2 series. The error-bars are smaller than the marker size, which is why these are not included.	30
2.9	The normalized peel force vs. the loss tangent measured at the peel frequency. (A) SX.A1B1 series, (B) SX.A2B2 series, and (C) SX.A2B1 series. The errorbars are smaller than the marker size, which is why these are not included.	31
2.10	The normalized peel force vs. the loss tangent measured at the peel frequency.	32
3.1	Sketch of the add-on fixture. It consist of two disks, an upper and a lower. A thin sample, of an initial thickness, d_0 , is wrapped around the two disks to form a hollow cylinder, with a radius of R_0 . The distance between the upper and lower contact perimeter, between the sample and fixture is h , where the initial distance is h_0	37
3.2	The Planar Extension Fixture (PEF)	38
3.3	Snapshots of test 1A at $t = \{0, 5, 10, 11, 13, 15, 20, 23, 25\}$ s, $\dot{\epsilon} = 0.097s^{-1}$	39
3.4	DMA spectra of the dynamic moduli of sample A at 25°C. The parameters G_0 , C and n are determined with a least square fit of the expression for $G'(\omega)$ to the measured data. $G_0 = 2500 \pm 60$ Pa, $C = 1800 \pm 60$ Pa s n and $n = 0.484 \pm 0.007$. The stoichiometric ratio, r , is equal to 0.57	42
3.5	DMA spectra of the dynamic moduli of sample B at 25°C. $G_0 = 5840 \pm 80$ Pa, $C = 3840 \pm 50$ Pa s n and $n = 0.435 \pm 0.002$. The stoichiometric ratio, r , is equal to 0.60	43
3.6	Illustration of the deformation on the cylindrical probe.	45
3.7	Axis-symmetric finite element mesh obtained with the modified MSF model. The dashed lines are the initial mesh. The solid lines are the mesh extended to a nominal Hencky strain of 2. Re-meshing has been applied in between these meshes.	47

3.8	$(D_0 - D(t))/D_0 = -\epsilon_\theta$ vs. the nominal Hencky strain, $\epsilon_N = \ln h(t)/h_0$. For details about the test conditions the reader is referred to tables 3.5 and 3.6	49
3.9	The true Hencky strain $\ln(l(t)/l_0)$ vs. the nominal strain, $\epsilon_N = \ln(h(t)/h_0)$. The data corresponds to the series given in figure 3.3 and the test conditions for test 1A (see table 3.5). The aspect ratio Λ_1 is equal to 24.8	50
3.10	True Hencky strain vs. nominal strain. $\Lambda_1 = 6.41$ and 12.7 for test 2A and 3A.	50
3.11	$\Lambda_1 = 4.81$ and 9.25 for test 1B and 2B. In test 2B the full and dashed lines are the modified Lodge and MSF model predictions from numerical simulations.	51
3.12	$\Lambda_1 = 26.8$ and 53.6 for test 3B and 4B. The full and dashed lines are the modified Lodge and MSF model predictions from numerical simulations.	51
3.13	$(D_0 - D(t))/D_0$ vs ϵ_N for TEST 2B, 3B and 4B. The dashed lines represent the numerical prediction based on the modified MSF model, while the full lines represent the numerical prediction based on the modified Lodge model	52
3.14	The measured stress difference, $\sigma_{zz} - \sigma_{xx}$, vs. the Hencky strain, $\epsilon = \epsilon_z$. The full lines are the ideal predictions of the modified Lodge model. The dashed lines are the classical predictions, where $\lambda = \lambda_z$	54
4.1	Sketch of the add-on fixture. It consist of two disks, an upper and a lower. A thin sample, of an initial thickness, d_0 , is wrapped around the two disks to form a hollow cylinder, with a radius of R_0 . The distance between the upper and lower contact perimeter, between the sample and fixture is h , Where the initial distance is h_0	59
4.2	The evolution of the relative outer diameter, $(D_0 - D(t))/D_0$ and logarithmic extension vs. time for $\Omega = 0.4 \cdot \pi$ rad/s and (A,C) $\Lambda = 1$ and (B,D) $\Lambda = 2.5$. The full line in (A) and (B) specifies the initial relative diameter, and buckling is assumed to occur when this line is crossed. The full curve in (C) and (D) corresponds to equation 4.1. The dots are the actual logarithmic plate separation (measured by the FSR), while the crosses are the strain validation made with particle tracking. All the results are obtained with sample A, with sample details specified in table 4.1	60
4.3	Snapshots of the experiment corresponding to the data shown in figure 4.2.B and D, at times $t \cdot \nu = \{0, 0.033, 0.067, 0.1, 0.127, 0.153, 0.2, 0.233, 0.267, 0.3, 0.333, 0.367, 0.433, 0.467, 0.533, 0.667, 1.027\}$	62
4.4	Normalized stress difference vs. normalized strain with $\Lambda = 2$, for sample A (A) and sample B (B). Sample details are specified in table 4.1.	63

4.5	(A) Evolution of the relative outer diameter vs. dimensionless time for $\Lambda = 2$ and three different angular frequencies. The dashed lines represent FEM simulations for the Lodge and DE network model. (B) Evolution of the relative outer diameter during steady elongation. The experimental data are the same as those in figure 3.13, the curves are obtained with FEM simulations with DE network model and the Lodge model. All the experimental data are obtained with sample B.	67
4.6	Measured stress differences obtained with sample B. $\Lambda = 2$, and $\Omega = 0.4 \cdot \pi$ rad/s. The blue and green line are the numerical FEM results, obtained with the Lodge and DE network model respectively. The red is ideal numerical planar oscillatory elongation obtained using the DE network model, <i>i.e.</i> , $\epsilon_\theta = 0$ and $I_1 = I_2$ by definition.	67
4.7	Work performed for sample B, when $\Omega = 0.4 \cdot \pi$ rad/s and $\Lambda = 2$. The red curve is the ideal Lodge prediction for two cycles, while the blue and green curves represent the FEM results obtained with the Lodge and the DE network models, respectively. The black crosses are experimental data.	69
4.8	(A) Work needed to elongate sample B at three different frequencies with $\Lambda = 2$. The red cures represent FEM predictions with the DE network model, while the cyan curves represent FEM results obtained with the Lodge model. (B) Work needed to elongate sample A at three different frequencies with $\Lambda = 2$ and (C) Work needed to elongate sample A at three different frequencies with $\Lambda = 1$	70
4.9	The relative amount of work performed by the samples upon flow reversal versus angular frequency.	71
4.10	The stress difference for sample B, when (A) $\Omega = 0.2 \cdot \pi$ rad/s and $\Lambda = 2$ and (B) $\Omega = 0.1 \cdot \pi$ rad/s and $\Lambda = 2$ and finally (C) $\Omega = 0.2 \cdot \pi$ rad/s and $\Lambda = 1$. The blue line is the FEM simulation with the Lodge model, while the green is obtained using the DE network model.	72
4.11	The stress difference for sample A, when $\Omega = 0.2 \cdot \pi$ rad/s and (A) $\Lambda = 1$ and (B) $\Lambda = 2$. The green is the ideal prediction of the DE network model.	73
5.1	Drawing of an ideal entangled network (IEN). All cross-linking points are reacted and no dangling ends, are present. The cross-linkers are represented as discrete points (black crosses) and gray circles are marking the trapped entanglements.	77
5.2	Illustration of a network with elastic active network strands and a dangling strand. Gray circles mark entanglements, where the trapped have been marked additionally with black rings. The cross-linking points are considered as discrete points and marked as black crosses.	78

5.3	A: A single network strand between two cross-links. B: A coarse-grained random walk chain (light gray) imaged above the real chain (dark gray). C: The primitive path chain (dark gray) imaged above the random walk chain. The primitive path is longer than the end-to-end distance between cross-links (black crosses) due to entanglements (gray circles).	79
5.4	Entangled network chain with primitive path statistics. The number of strands, Z , is 4. Kuhn steps can shuffle through the slip-links due to sliding dynamics.	79
5.5	A: An entangled dangling strand (EDS). B: An entangled network strand (ENS). Gray circles are marking the entanglements, while black crosses resembles the cross-links.	82
5.6	The fraction of destroyed entanglements by SD and CD. $N_K = 60$, $\beta = 20$ and $w_{DS} = 0.6$. The CD spectrum is that obtained in figure 5.7	85
5.7	$f_d(t)$ obtained from a simulation of the EDS model with $N_K = 60$ and $\beta = 20$ and an ensemble of 100 chains. The crosses are simulated data, while the full line is a fitted spectrum: $\tau_0 = 0.0498$, $\tau_1 = 1151$, $\tau_2 = 264451$, $\alpha_1 = 0.453$ and $\alpha_2 = -0.271$	86
5.8	Relaxation modulus produced by the IEN model with $N_K = \{60, 100, 120\}$ and $\beta = \{5, 10, 15, 20\}$. All the black lines are the BSW fits of each data set.	89
5.9	Equilibrium plateau modulus, G_0 , vs. the average number of entanglements, the line represents a linear fit to G_0 with $a = 0.74 \pm 0.05$.	90
5.10	Power-law exponent, α , and the relaxation time, τ_1 , vs. the average number of entanglements.	90
5.11	Dynamic relaxation spectrum for $N_K = 60$ and $\beta = 20$ obtained with the IEN model. G' is several orders of magnitudes larger than G'' , the shape of G' can be seen in the inset. The BSW parameters are listed in table 5.2.	91
5.12	G' and G'' obtained from small amplitude oscillatory shear experiments with a polypropylene oxide (PPO) network. We assume that the entanglement plateau, G_N^0 , is equal to 700 kPa, which is for the pure PPO melt [1].	92
5.13	Green-Kubo simulation results obtained with both model applications. $N_K^N = N_K^D = 60$, $\beta = 20$ and $w_{DS} = 0.6$.	93
5.14	G^* result for $N_K^N = N_K^D = 60$, $\beta = 20$ and $w_{DS} = 0.6$. The BSW parameters are listed in tables 5.3 and 5.4. The black horizontal line is $G_{0,ana} = w_{NS}G_{0,NS}$, where $G_{0,NS}$ is obtained from equation 5.28.	94

5.15	G^* results obtained for $w_{DS} = 0.83$. The solid curves are obtained for $\beta = 20$ and $N_K^N = N_K^D = 60$, the dashed for $\beta = 10$ and $N_K^N = N_K^D = 60$, and the dotdashed are for $\beta = 10$, $N_K^N = 60$ and $N_K^D = 120$. The BSW parameters are listed in tables 5.3 and 5.4. The thin black lines are representing the slope of G'' of the experimental data shown in figure 5.12 while the dashed horizontal lines represent the analytical estimation of the plateau.	96
5.16	G^* results obtained for $w_{DS} = 0.83$ (solid curves) and $w_{DS} = 0.90$ (dashed curves). The model parameters are in both cases $\beta = 20$ and $N_K^N = N_K^D = 60$. The thin black line shows the slope of G'' from the experimental data in figure 5.12. The BSW parameters are listed in tables 5.3 and 5.4.	99

List of Tables

2.1	Molecular weight distributions of the polymers A1 and A2, and the cross-linkers B1 and B2, measured with a SEC triple detector and GPC respectively.	22
2.2	Overview of the 15 test samples.	23
3.1	Molecular weight distributions of the linear PPO, and the PDMS cross-linker respectively. χ_i is the chemical functionality of each component reported by Kaneka Corp. in mmole/g	40
3.2	Horizontal shift factor, a_T	41
3.3	Characteristic parameters for sample A and sample B at 25 °C. .	41
3.4	Expressions for ϕ_1 and ϕ_2 for neo-Hookean strain measure and tube strain measure without instantaneous chain retraction. The Currie approximation is used for the tube model.	44
3.5	PEF test conditions for sample A. $\Lambda_1 = h_0/d_0$, $\Lambda_2 = R_0/h_0$. The Hencky strain rate is in all cases equal to 0.097 s^{-1}	48
3.6	PEF test conditions for sample B. $\Lambda_1 = h_0/d_0$, $\Lambda_2 = R_0/h_0$. The Hencky strain rate is in all cases equal to 0.1 s^{-1}	48
4.1	Characteristic parameters for sample A and sample B at 25 °C. .	63
5.1	Parameters and variables of the coarse-grained chain.	79
5.2	BSW parameters obtained by fitting equation 5.23 combined with equation 5.24 to the simulated data presented in figure 5.8. . . .	89
5.3	BSW parameters for EDS, $N_K^N = 60$ for the network strands . . .	94
5.4	BSW parameters for ENS, $N_K^N = 60$ for the network strands . . .	94
5.5	Kuhn parameters for the PEO chain. The monomer molecular weight, M_0 , is for a PPO chain.	95

Chapter 1

Introduction

In the health care sector, adhesives are used for a multitude of purposes including wound treatment and colostomy care. Often the desired adhesive should have a number of apparently conflicting properties: It should be easy to apply, it should stick without sliding once applied, and it should also be easy to remove without hurting the skin.

Despite the strong technical and economic interest in the design of adhesives with given properties, the underlying physics and chemistry is still poorly understood. Standard tests, include tests for the somewhat loosely defined properties of peel and tack. First of all there is the problem of relating tack and peel to well defined surface and bulk properties of the adhesive material. Secondly our understanding of the connection between molecular structure of typical adhesive materials and their macroscopic properties is still quite incomplete.

1.1 Pressure-Sensitive Adhesives

Pressure sensitive adhesives (PSA) are designed to stick to almost any type of surface by simple contact under light pressure, and not to undergo any physical transformation or chemical reaction during the bonding process. In more general terms PSAs are often classified as soft, deformable solids [2].

The advantage of PSAs over other adhesives is that they are easy and safe to use, molecular contact is usually established at room temperature, and the only interfacial forces active in PSA adhesion are van der Waals forces.

Polymer networks belong to a special class of PSAs which has gained increasing attention due to the use of gel-like materials as for instance matrices for drug-delivery systems, implants and skin adhesives [2–5]. The end product properties have been shown to be highly dependent on the material preparation [4, 6–8], and a need for improved understanding of the material behavior based on different initial compositions has appeared.

1.2 Peel

For many years the industrial formulation of PSAs proceeded mainly empirically, using a variety of trade tests designed to match the PSA conditions subjected to a particular application [2]. One of the most often measured characteristics of PSAs is the resistance to peel from a given substrate [3, 9–18]. The measured peel force is frequently used to compare different PSAs, and to evaluate the quality of the adhesive bonds. When dealing with peel experiments, it is common to distinguish between three types of failure modes [9, 10, 12]; 1) *Cohesive failure*, which occurs at high temperatures or low peel rates, and the deformation is primarily viscous, allowing the failure strain to be reached. This leads to a failure mode where residue of the adhesive will remain on the substrate. 2) *Adhesive failure* occurs at intermediate temperatures or peel rates, where the failure of strain will not be reached, and the adhesive will peel off cleanly from the substrate. 3) *Unstable failure* is observed at low temperatures or high peel rates. It is a stick-slip behavior related to the glassy response of the adhesive. It is considered unstable since oscillatory force variations are observed. Usually, failure modes other than *adhesive* are considered as faulty product design. However, the transition from one failure mode to another has proved to be very complex, and in some cases the same material can exhibit both *cohesive* or *adhesive* failure depending on the peel rate and temperature used [9].

The peeling process involves a strong deformation of the PSA at the peel front [3], and thus a complicated stress field [19], and the shape of the peel front is largely influenced by the sample thickness, the peel velocity and the bulk rheological properties [10, 12, 14].

As the demands for the PSA quality increases (*e.g.*, for skin adhesives), it is desired to gain a better understanding of the peel process, and in general the end product material behavior. Ideally we would like to be able to predict the material behavior from the initial PSA formulation.

1.3 Polymer Networks

Polymer networks are in general formed when linear end-functionalized polymers react with cross-linkers forming large clusters of hyper-branched polymers. At continuous reaction the clusters will react with each other, and at a certain critical extent of reaction, p_c , an infinite network spanning the entire volume is formed. This infinite polymer is called a gel, and is permeated with finite branched polymers acting as a solvent. The transition from a system with only finite branched (soluble) polymers, to a two-phase system with both a gel and soluble structures, is called gelation. The critical point where the gel first appears is called the gel-point [20]. An illustration of a cross-linked network is shown in figure 1.1. All the thin lines represent polymeric strands that are connected to the infinite network, while the thick lines represent soluble structures. The black dots are cross-linkers, while the circles mark the presence of dangling structures, that is structures connected to the network in one end only. Hence,

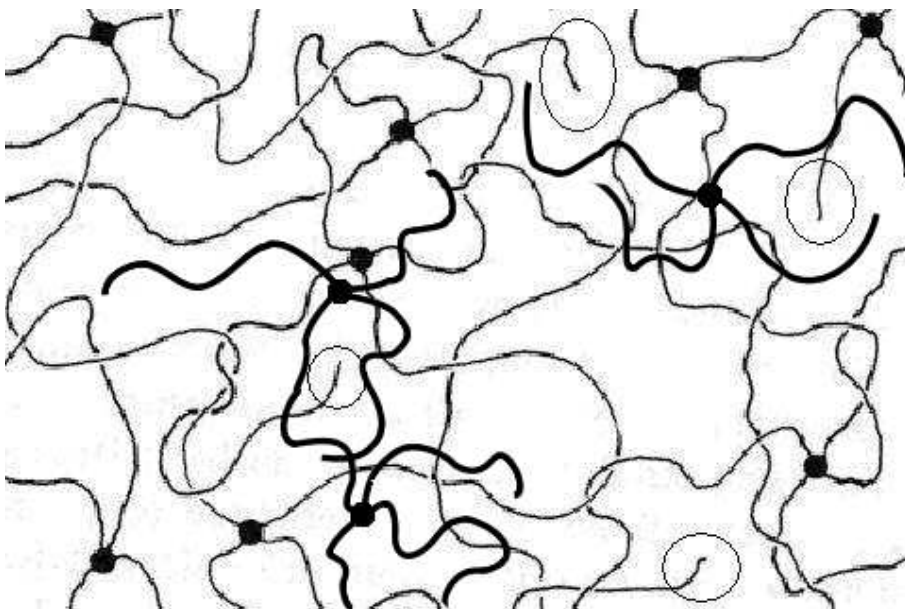


Figure 1.1: Illustration of a cross-linked network. The black dots mark the cross-linkers. The circles mark the ends of dangling structures, *i.e.* structures that are connected to the network in one end only. The thick lines represent the soluble polymeric structures.

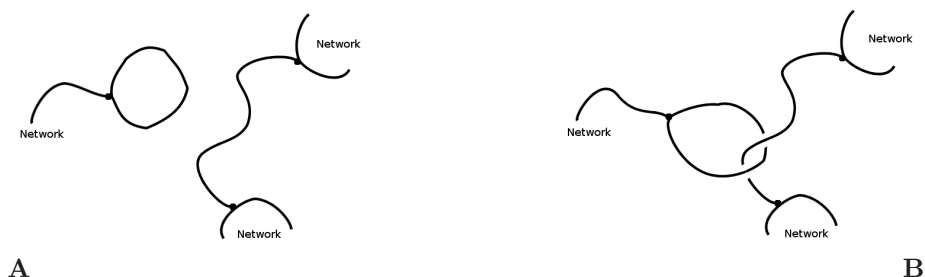


Figure 1.2: Inactive (A) versus active loops (B)

when looking at the whole system, which consists of a gel, solubles and dangling structures, it is obvious that it has a wide distribution of different structures.

A more detailed description of the network structures includes active, and inactive loop formation, which are illustrated in figure 1.2. Figure 1.2.B shows a loop entangled with the elastically active network. Since it is connected to the network through this topological link, called an entanglement, the loop itself will be elastically active and thereby contribute to the elastic modulus. Opposite, figure 1.2.A, shows an inelastic loop, and since there are no topological links to the elastically active network, the loop will merely act as a dangling structure.

When taking an even closer look at the network, we can divide the entangle-

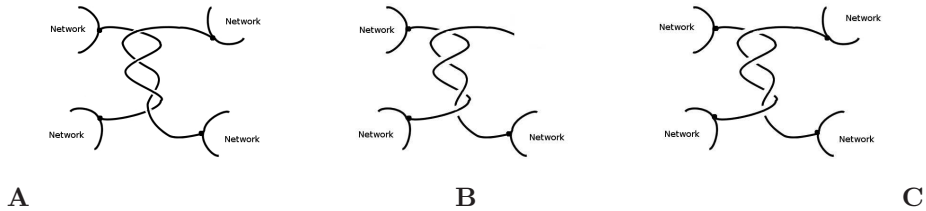


Figure 1.3: Illustration of temporary entanglements. (A) between two elastically active network strands and (B) between a network strand and a dangling strand and finally (C) stationary entanglements between two networks strands

ments into temporary and permanent (trapped) entanglements. Illustrations of these are shown in figure 1.3. Opposite to linear chains, where all entanglements are temporary due to reptation [21] and thus, subject to complete relaxation, polymer networks will, due to cross-links and closed loops, have permanent entanglements, as illustrated in figure 1.3.C. These entanglements will prevent complete relaxation by reptation. However, some relaxation will occur due to the temporary entanglements, for which two special examples are illustrated in figures 1.3.A and B. In case A, the network chains can disentangle by sliding off each other, while in case B, the free end of the dangling strand can diffuse freely along its path, and given enough time, all the initial entanglements on the dangling strand will be destroyed.

Active and inactive loops, as well as permanent and temporary entanglements, will contribute differently to the elastic modulus. We find that in particular the entanglements, both temporary and permanent, have a significant impact on the material properties [22–24]. It is therefore important to understand the connection between network preparation, and the resulting network structure. In the aim of doing so, Macosko and Miller [25, 26] presented a simple recursive method for calculating the weight fractions of soluble and dangling structures beyond the gel-point. The method is based on Flory’s [27] three simplifying assumptions:

1. All functional groups of the same type are equally reactive
2. All groups react independently of each other
3. No intra-molecular reactions occur in finite species

The methodology is [25–28]: Consider the polymerization of a difunctional linear polymer, B_2 , and a f functional cross-linker, A_f , where reaction occur exclusively between A and B units. The components can either be added in stoichiometric ratios, $f[A_f] = 2[B_2]^1$, or imbalanced ratios, with

$$r = f[A_f]/(2[B_2]) \quad (1.1)$$

¹[...] is molar concentration

defining the stoichiometric imbalance. p_A and p_B are the extent of conversion of A and B sites respectively, for convenience we define $p = p_B = rp_A$. Let the cross-linking reaction proceed until some fraction of the polymers have reacted. Then pick a polymer site B (or cross-linker site A) at random, and let F_B (or F_A) be the event that this site leads to a finite chain, *i.e.*, B (or A) is either unreacted or connected to a dangling structure. For a given functionality of the cross-linker, it is possible to derive a recursive formula for the probability of B being connected to a finite chain. At first the idea is to look either inwards or outwards from the chosen site, and then define the probability of being connected to a finite chain. In general we have the relation

$$P(F_i^{\text{in}}) = P(F_i^{\text{out}})^{k-1}, \quad (1.2)$$

with k as either the functionality, f , of the cross-linker or the functionality of the polymer, which is equal to 2. Hence,

$$P(F_B^{\text{in}}) = P(F_B^{\text{out}}) = P(F_B). \quad (1.3)$$

When looking out from an A or B site we have

$$\begin{aligned} P(F_A^{\text{out}}) &= p_A P(F_B) + 1 - p_A \\ P(F_B) &= p P(F_A^{\text{in}}) + 1 - p. \end{aligned} \quad (1.4)$$

Combining equations 1.2 to 1.4, and assuming that B sites are added in excess and $p_A = 1$, results in the following recursive formulation²

$$P(F_B) = pP(F_B)^{f-1} + 1 - p, \quad 0 \leq p < 1. \quad (1.5)$$

Equation 1.5 fails when $p = 1$, however, in this case $P(F_B) = 0$ by definition. The weight fractions of network strands (NS), dangling strands (DS) and soluble strands (SS) are thus:

$$\begin{aligned} w_{\text{NS}} &= (1 - P(F_B))^2 \\ w_{\text{DS}} &= 2P(F_B)(1 - P(F_B)) \\ w_{\text{SS}} &= P(F_B)^2. \end{aligned} \quad (1.6)$$

$P(F_B)$ can be determined numerically for given values of f and p . In figure 1.4 the weight fractions from equation 1.6 are shown versus p for $f = 3$. It is observed that below some critical extent of reaction, p_c , no network is formed. p_c can be determined analytically, by introducing the branching probability, α . That is the probability that a given cross-linker is connected to another cross-linker

$$\alpha = p_A p_B = r p_A^2 = p^2 / r. \quad (1.7)$$

By dividing the network into generations as illustrated in figure 1.5 we can derive the number of bonds on average in each generation based on α [20]. The

²For a more detailed derivation the reader is referred to references [25, 26].

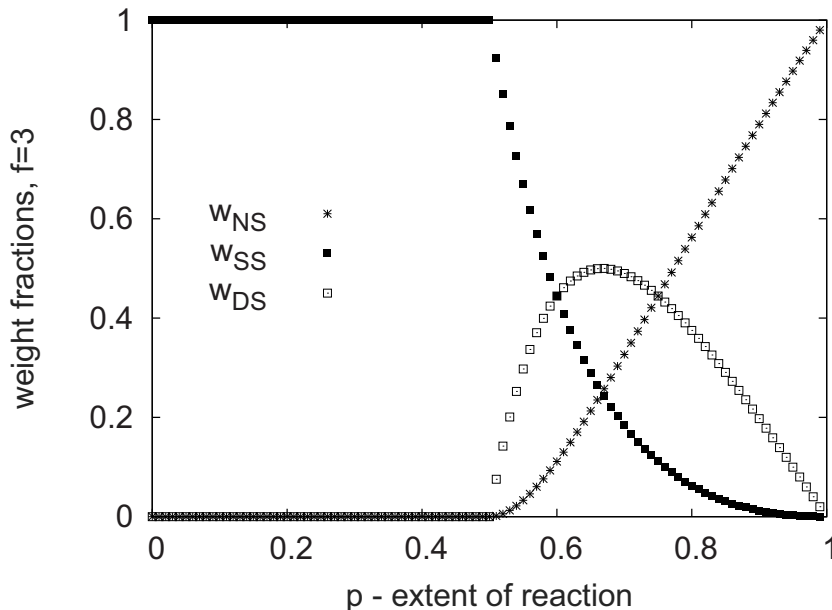


Figure 1.4: Weight fractions of soluble (SS), network (NS) and dangling strands (DS) versus extent of reaction, p , for a three-functional cross-linker ($f = 3$).

cross-linker to the right on the parent bond (generation 0) have two remaining cross-linking sites that can be connected to two other sites, hence, the average number of connections in the first generation is 2α . In the general case with a f functional cross-linker we have $(f-1)\alpha$ connections in the first generation, and the second will have $((f-1)\alpha)^{f-1}$ average number of connections. Continuing to the n^{th} generation we have

$$\left(\left((f-1)\alpha \right)^{f-1} \right)^{n-1},$$

connections on average. If $(f-1)\alpha < 1$ the number of connections in each generation will, on average, be smaller than the previous generation and as n increases we will eventually reach the ends of the structure, and no infinite network will be formed. In contrast if $(f-1)\alpha > 1$ the branched structure will continue growing to an infinitely large cluster as $n \rightarrow \infty$. Obviously, $(f-1)\alpha = 1$ is the critical condition for network formation, and the critical branching probability is thus

$$\alpha_c = \frac{1}{f-1}. \quad (1.8)$$

Expanding to the more general case where the polymer is no longer difunc-

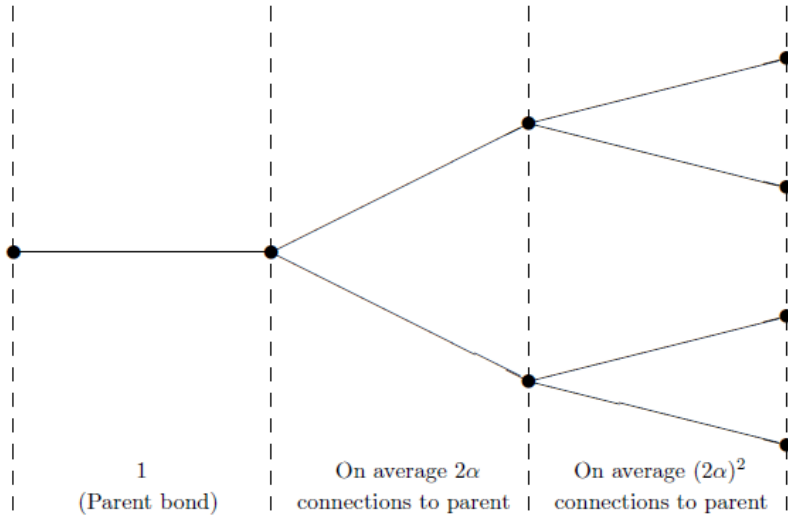


Figure 1.5: Illustration of a network without loops on a Cayley tree with tri-functional cross-linkers.

tional, but has some functionality g , the critical branching probability becomes

$$\alpha_c = \frac{1}{(f-1)(g-1)}. \quad (1.9)$$

There are three special cases when preparing polymer networks; The first case is when A and B sites are mixed in equal amounts ($r = 1$), and reacted to complete reaction. Then the critical extent of reaction is $p_c = \sqrt{\alpha_c}$. The second case, is when B is added in excess and $p_A = 1$, then $p_c = \alpha_c$. Finally when A is added in excess and $p = 1$, then the critical extent of reaction of A sites is $p_{A,c} = \alpha_c = 1/r$.

This recursive equation 1.5 suggests that a perfect network (*i.e.*, a network where all sites are ideally reacted, and no intra-molecular loops are formed) is formed when $r = 1$ and $p = 1$. For this to be correct pre-gel intra-molecular reactions must be negligible, and post-gel intra-molecular reactions should always lead to elastically active chains. The reality is somewhat different since pre-gel loop formation is difficult to avoid. Additionally it is expected that after some reaction time there will be remaining active A and B sites far away from each other. As molecules grow bigger they will diffuse more slowly, making it difficult for these sites to “find” each other on the time scale of the reaction, and it is thus, difficult to reach complete reaction. It is expected that these unreacted sites will cause the weight fractions of dangling strands and soluble strands to be bigger than predicted by equation 1.6. Nonetheless, the theory gives a reasonable estimate for the amount of solubles and dangling strands in

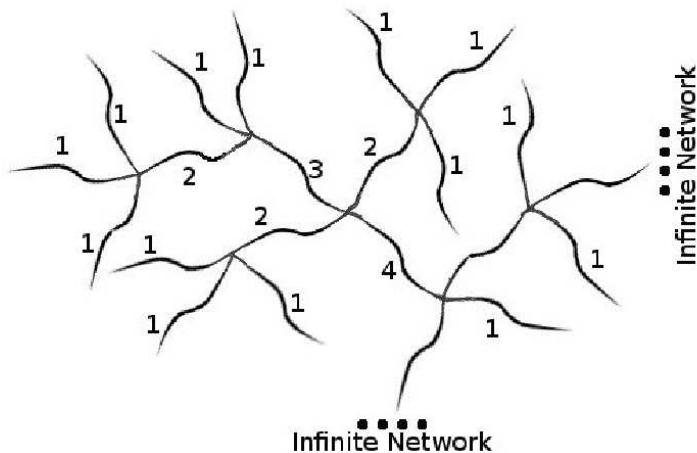


Figure 1.6: Tetra-functional ($f = 4$) cross-linked network with dangling structures of different degree of branching. The branched strands are labeled with their respective seniority when looking from the root of the dangling strands to their furthest branch end. The seniority counting fails for elastically active strands.

the systems considered.

A similar approach can be used to derive the *seniority distribution* of the network, which is described in next section. This distribution provides a more detailed structural description of the dangling and soluble structures.

1.3.1 Seniority Principle

The topological structure of hyper-branched molecules can be described by the seniority principle [29]. The seniority counts the number of segments that connects a given interior segment to the retracting chain end, which is responsible for its relaxation. It is used for the concept of hierarchical relaxation such that segments with seniority 1 will relax as star arms, hereafter, segments with seniority 2 will follow, and so forth [29].

The seniority principle can be transferred to cross-linked networks, which often, depending on the extent of reaction or stoichiometric imbalance, can be considered as hyper-branched systems. Caution should, however, be taken since the seniority counting fails for elastically active chains. This is illustrated in figure 1.6, where a part of a network structure is shown, and the strands connected to the infinite network in both ends are not assigned a seniority.

When assigning a seniority to a randomly chosen strand we count the number of strands to the furthest end looking out from both ends of the strand. The actual seniority is then defined as the smallest of the two. We call this the

bidirectional seniority. Hence, we start by defining the one-directional seniority distribution before the bidirectional distribution.

Since the seniority counting fails for elastically active network strands, we must define the event, Q , that the chosen strand is not connected to the infinite network in both ends, which has the probability

$$P(Q) = 1 - [1 - P(F_B)]^2 = 1 - w_{\text{NS}} = w_{\text{DS}} + w_{\text{SS}}. \quad (1.10)$$

Given this, we define the conditional cumulative one-directional seniority distribution

$$f_m = P(\text{one-side seniority} \geq m | Q), \quad (1.11)$$

where m is the seniority. We consider the special case of reacting a f -functional cross-linker, A_f , with an end-linked polymer, B_2 . The polymer is added in excess, and we assume that all cross-link sites have reacted, *i.e.*, $p_A = 1$. The statistics are thus, solely dominated by the extent of reaction with respect to B sites, p , as p_A and p are correlated. With these informations we can derive a recursive expression for f_m . That is, a strand is either unreacted with probability $1 - p$ or reacted with probability p . If it has reacted then the strand has seniority greater than or equal to m , only if all the $(f - 1)$ subsequent strands have seniority greater than or equal to $m - 1$. Hence,

$$f_m = (1 - p) + p[f_{m-1}]^{f-1}. \quad (1.12)$$

From equation 1.12 we can generate all the f_m by noting that the probability of having a loose end of seniority 1 is equal to the probability that a chain is unbranched, *i.e.*, $f_1 = (1 - p)$. Given f_m we can estimate the conditional one-directional probability of seniority m

$$s_m = f_m - f_{m-1} \quad (1.13)$$

The bidirectional seniority is m when the seniority in one direction equals m , and is less than or equal to m in the other direction (or opposite), hence,

$$s_m^B = 2s_m(1 - f_m) + s_m^2. \quad (1.14)$$

Since s_m^B is the actual seniority distribution, we will in the following omit the term bidirectional. The seniority distribution is shown in figure 1.7.A in a lin-log scale, and in figure 1.7.B in log-log scale, for various extent of reaction p with $f = 3$. Since we are interested in networks, we only use $p \geq p_c$. It is seen that there is a cross-over between exponential decay and power-law decay, and that the power-law dominates at low seniorities, or close to the critical extent of reaction ($p_c = 0.5$).

Figure 1.7 shows that we find the broadest structural distribution close to the critical extent of reaction, while it gets more narrow as p increases, *i.e.*, as more and more strands become elastically active.

When a segment has a finite seniority it is subject to relaxation. This occurs hierarchically in strand seniority [29]. The time scale for the relaxation of each

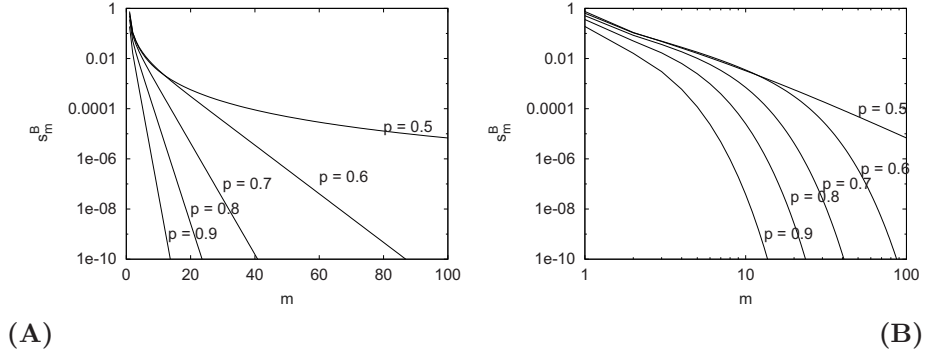


Figure 1.7: Bidirectional seniority distribution for different extent of reactions, p , of the linear polymer on a (A) linear-log scale and (B) log-log scale.

seniority is recursively dependent on the previous one, as proposed by Read *et al.*[29]

$$\tau(m+1) = \tau(m) \exp\left(\frac{15}{8} N_x [S(m)]^\alpha\right). \quad (1.15)$$

Here α is a dilution exponent arising from the tube model theory [29], where it is argued, that relaxed strands dilute unrelaxed strands with higher seniority, usually $\alpha = 4/3$ is used. N_x is the number of entangled segments on a strand, and $S(m)$ is the unrelaxed concentration of strands at the time scale corresponding to seniority m . We define the latter as the cumulative distribution of seniorities greater than or equal to m

$$S(m) = P(\text{one way seniority} \geq m) = w_{\text{NS}} + \sum_{k=m}^{m_{\text{max}}} s_k^B, \quad (1.16)$$

where m_{max} is the maximum finite seniority. It is known that the sum of all finite seniorities, should equal $P(Q)$. We can therefore estimate m_{max} from the following

$$P(Q) = \sum_{k=1}^{m_{\text{max}}} s_k^B. \quad (1.17)$$

For $f = 3$ and $p = 0.6$ and $m_{\text{max}} = 30$ we find that

$$\frac{P(Q) - \sum_{k=1}^{30} s_k^B}{P(Q)} = 1.5 \cdot 10^{-4}. \quad (1.18)$$

We generate the relaxation times for each seniority by setting $\tau(m=1) = 1$. The fundamental time scale used to non-dimensionalize the time is the Rouse time of a single entangled strand, τ_e . In figure 1.8 the relaxation time spectra for $f = 3$ and $p = 0.4, 0.6$ and 0.8 are shown. It is seen that for $p > p_c$, there is an exponentially large range of time scales, while this is not the case for $p = 0.4 < p_c$, which is a post-gel system.

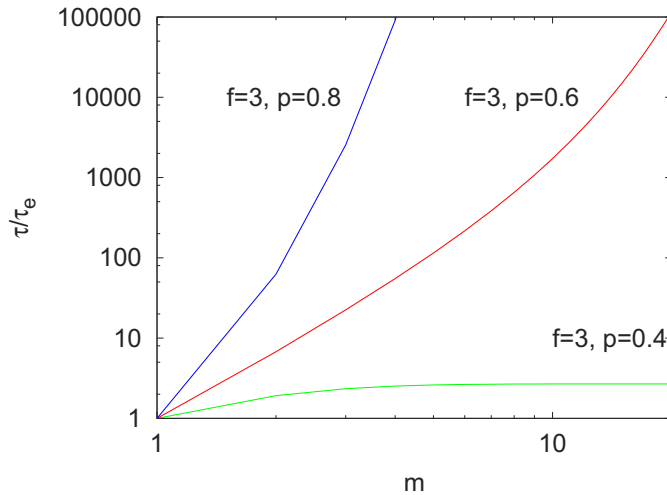


Figure 1.8: Relaxation time spectra for $p = 0.4$ and 0.6 . τ is made dimensionless with the Rouse time, τ_e , and $\tau(1) = 1$.

The seniority distribution provides us with some detailed information about how the network structure changes during gelation. We see how the amount of finite seniorities decreases as the network reaction proceeds above gelation in figure 1.7, and how this also slow down the relaxation process in figure 1.8. With this we can safely state that weakly cross-linked networks consist of a broad distribution of complicated structures, all with different relaxation times. This will evidently influence the rheological material behavior.

1.4 Rheology

1.4.1 Background

The term Rheology was inspired by the quotation *Panta rei*, “*everything flows*”, and it concerns the study of deformation and flow of complex fluids, *e.g.*, mud, bread dough, suspensions and polymers.

When studying the rheological behavior of a material, a relation between the material stress, that is force per area, and the resulting deformation is wanted. Two well-known material classes are Newtonian fluids and pure elastic solids also called Hookean solids. The stress-strain relations for these materials are very simple; In the Newtonian case the stress is proportional to the strain rate, while the stress is proportional to the strain for Hookean solids. Many materials exhibit both viscous and elastic behavior, and will therefore exhibit a time dependent strain. This group of materials are termed *viscoelastic*.

Polymer networks are categorized as elastomers, and are in principle solids. However, depending on the network preparation there will be components present

which are non-elastic of nature (*cf.* the two previous sections), and it is therefore, common to treat polymer networks as viscoelastic.

In the aim of establishing reliable structure-property relations for this special type of material, researchers have been studying the mechanical properties of elastomeric materials over several decades [6, 8, 10, 22–24, 30–36]. Several experimental techniques have been designed for this [37, 38], where common measures of the mechanical properties include; dynamic mechanical testing [32, 33, 39–44], and mechanical stress-strain measurements in elongation [8, 23, 30, 35, 36].

1.4.2 Dynamic Mechanical Analysis

This measuring technique involves small deformations of a sample in shear flow, and is also called *small amplitude oscillatory shear (SAOS)*. It measures the unsteady shear response of a sample contained between two parallel plates. The upper plate undergoes small-amplitude sinusoidal oscillations with frequency ω , while the lower plate is fixed. Assuming that the instantaneous velocity profile is linear the time-dependent shear strain and shear rate are given by [37]:

$$\gamma_{xy} = \gamma^0 \sin \omega t \quad (1.19)$$

$$\dot{\gamma}_{xy} = \frac{d}{dt} \gamma_{xy} = \gamma^0 \omega \cos \omega t = \dot{\gamma}^0 \cos \omega t \quad (1.20)$$

where γ^0 and $\dot{\gamma}^0$ are the amplitudes of the shear strain and shear rate oscillations, respectively. An interesting measure in SAOS experiments is the phase angle, δ . For Newtonian fluids $\delta = \pi/2$, *i.e.*, the measured shear stress is out-of-phase with the shear strain, while for Hookean solids the shear stress will be in-phase with the shear strain, with $\delta = 0$. For polymeric materials the shear stress will be out-of-phase with the shear strain or rate, with $0 < \delta \leq \pi/2$. The shear stress expressed in terms of the phase shift is given by

$$\sigma_{xy} = A(\omega) \gamma^0 \sin(\omega t + \delta(\omega)) \quad (1.21)$$

where $A(\omega)$ is the stress amplitude, which can be decomposed to display the in-phase and out-of-phase part of the shear stress. We define two equivalent viscoelastic material functions, G' and G'' , as

$$A(\omega) = \sqrt{G'^2 + G''^2}, \quad \tan \delta = G''/G' \quad (1.22)$$

The storage modulus, G' , is the in-phase component of the stress and gives information about the elastic energy storage that takes place during deformation, while the loss modulus, G'' , is the out-of-phase component of the stress and measures the loss of energy due to viscous dissipation. The shear stress can be rewritten in terms of G' and G''

$$\sigma_{xy} = G' \gamma^0 \sin \omega t + G'' \gamma^0 \cos \omega t. \quad (1.23)$$

G' and G'' are strain independent below some linear viscoelastic limit. Hence, for sufficiently small strain values, we refer to these functions as the linear viscoelastic moduli. In the limit of a Hookean solid or a Newtonian liquid the values for the moduli are

$$\begin{aligned} \text{Hookean Solid: } G' &= G, \quad G'' = 0 \\ \text{Newtonian Liquid: } G' &= 0, \quad G'' = \mu\omega \end{aligned} \quad (1.24)$$

where G is the elastic modulus and μ the Newtonian viscosity.

Linear Viscoelastic Predictions

When predicting the stress strain behavior it is common to use the *general linear viscoelastic model*

$$\boldsymbol{\sigma} = \int_{-\infty}^t G(t-t') \dot{\boldsymbol{\gamma}}(t') dt' = - \int_{-\infty}^t M(t-t') \boldsymbol{\gamma}(t, t') dt' \quad (1.25)$$

where $G(t-t')$ is the *relaxation modulus* and $M(t-t') = \partial G(t-t')/\partial t'$ is the *memory function*, $\dot{\boldsymbol{\gamma}}$ is the rate of strain tensor defined by the velocity gradient, $\nabla \boldsymbol{\nu}$

$$\dot{\boldsymbol{\gamma}} = \nabla \boldsymbol{\nu} + (\nabla \boldsymbol{\nu})^\dagger, \quad (1.26)$$

where \dagger denotes the transpose operation on a tensor. The fundamental idea of the model is that the stress at the present time, t , depends on the rate of strain at time t as well as the rate of strain at all past times t' , with a weighting factor given by the relaxation modulus. Since the relaxation modulus is a decreasing function, the memory is said to be *fading*. Relating equation 1.25 with 1.23 we find that

$$G'(\omega) = \omega \int_0^\infty G(s) \cos(\omega s) ds \quad (1.27)$$

$$G''(\omega) = \omega \int_0^\infty G(s) \sin(\omega s) ds, \quad (1.28)$$

where $s = t - t'$. Several versions of the general linear viscoelastic model exists, *e.g.*, the Maxwell model or Jeffreys model [37]. The only difference in these models is the expression for the relaxation modulus. Winter and Chambon [45, 46] proposed a simple form of the relaxation modulus for polymers undergoing gelation. Based on experimental observations they concluded that the transition from a liquid to a solid result in a power law behavior for G' and G'' , and they defined the relaxation modulus by

$$G(t) = Ct^{-n}, \quad 0 < n < 1 \quad (1.29)$$

The material parameter, C [Pa s ^{n}], is called the strength of the network at the gel-point and n is a power law exponent. Inserting equation 1.29 into equations 1.27 and 1.28 result in the corresponding dynamic moduli

$$\begin{aligned} G'(\omega) &= C\omega^n \pi / (2\Gamma(n) \sin(n\pi/2)) \\ G''(\omega) &= C\omega^n \pi / (2\Gamma(n) \cos(n\pi/2)), \end{aligned} \quad (1.30)$$

where $\Gamma(n)$ is the gamma function. It is observed that the loss tangent, $\tan \delta = G''/G'$, is independent of frequency, which is a characteristic for the gel-point [45, 46].

1.4.3 Elongational Measurements

In the application of PSAs as well as in the polymer processing industry it is often of much more importance to analyze the large-strain, high-rate behavior of polymers. For this reason different measuring techniques have been developed for such characterizations.

Three well established elongational flow types have been defined, that is; 1) uni-axial elongation, 2) biaxial stretching and 3) planar elongation. A characteristic feature of steady elongational flows is that neighboring fluid particles move relative to each other at an exponential rate, *i.e.*, the material undergoes very large deformations in elongation.

From the measured force, $F(t)$, needed to elongate the sample at a given elongation rate it is possible to estimate the stress difference³

$$\sigma_{zz} - \sigma_{xx} = \frac{F(t)}{A(t)} = \frac{F(t)}{A_0 \exp(-\dot{\epsilon}t)}, \quad (1.31)$$

where $\dot{\epsilon}$ is the strain rate. In ideal elongation the cross-sectional area, $A(t)$, decreases (or increases for biaxial flow where $\dot{\epsilon} < 0$) exponentially in time from the initial area, A_0 .

In uniaxial elongation the length, $L(t)$, of the sample will increase as

$$L(t) = L_0 \exp(\dot{\epsilon}t), \quad (1.32)$$

where L_0 is the initial length. When deforming a cylindrical sample with initial diameter D_0 , the diameter, $D(t)$, will decrease with time as

$$D(t) = D_0 \exp(-1/2\dot{\epsilon}t), \quad (1.33)$$

A number of experimental techniques have been constructed to measure different types of elongation. Among the most important we find the *polymer melt elongational rheometer* (RME) designed by J. Meissner [47], and the *filament stretch rheometer* (FSR) designed by Sridhar and coworkers [48]. A more recent development to measure elongational stresses, is the *dual wind-up drum rheometer*, which is developed by Sentmanat, and called the *Sentmanat Extensional Rheometer* (SER) [49].

³for incompressible fluids it is only possible to measure pressure differences and not absolute values, hence quantities of experimental interests are the stress differences $\sigma_{zz} - \sigma_{xx}$ and $\sigma_{yy} - \sigma_{xx}$ [37].

Nonlinear Predictions

In elongation the rate of strain tensor, $\dot{\boldsymbol{\gamma}}$, has three non-zero components

$$\dot{\boldsymbol{\gamma}} = \begin{pmatrix} -(1+b)\dot{\epsilon} & 0 & 0 \\ 0 & -(1-b)\dot{\epsilon} & 0 \\ 0 & 0 & 2\dot{\epsilon} \end{pmatrix},$$

where b is a factor defining the type of flow; for $b = 0$ and $\dot{\epsilon} > 0$ we measure uni-axial elongation, when $b = 0$ and $\dot{\epsilon} < 0$ we have biaxial stretching, and finally for $b = 1$ we have planar elongation. By assuming isotropic materials, the stresses and material functions in simple shear-free flows depend on $\dot{\epsilon}$ and b only.

The general linear viscoelastic model can be used to predict the stress difference in the linear regime, that is at low Hencky strains, $\epsilon = \dot{\epsilon}t$

$$\sigma_{zz} - \sigma_{xx} = \int_{-\infty}^t G(t-t')(2\dot{\epsilon} - (-(1+b)\dot{\epsilon}))dt' = (3+b)\dot{\epsilon} \int_{-\infty}^t G(t-t')dt'. \quad (1.34)$$

To model the nonlinear regime the general linear viscoelastic model must be generalized to describe flows with large displacement gradients. This is done by considering the strain, and the strain history [37, 38]. The methodology for this generalization is to consider a fluid particle, and then describe its trajectory through the three dimensional space occupied by the fluid, and from that introduce finite strain tensors. Say at some past time t' , the particle has position \mathbf{r}' , and at present time t , the particle has position \mathbf{r} . The motion of the particles may then be described by the two displacement gradient tensors

$$\boldsymbol{\Delta}(\mathbf{r}, t, t') = \frac{\partial \mathbf{r}'(\mathbf{r}, t, t')}{\partial \mathbf{r}} \quad , \quad \mathbf{E}(\mathbf{r}, t, t') = \frac{\partial \mathbf{r}(\mathbf{r}', t', t)}{\partial \mathbf{r}'} \quad (1.35)$$

From these we define the lower and upper convected finite strain tensors

$$\boldsymbol{\gamma}^{[0]} = \{\boldsymbol{\Delta}^\dagger \cdot \boldsymbol{\Delta}\} - \boldsymbol{\delta} \quad , \quad \boldsymbol{\gamma}_{[0]} = \boldsymbol{\delta} - \{\mathbf{E} \cdot \mathbf{E}^\dagger\}, \quad (1.36)$$

where $\boldsymbol{\delta}$ is the unit tensor. For small displacements both of these tensors reduce to the infinitesimal strain tensor, $\boldsymbol{\gamma}$, which is defined by the velocity gradient for small displacements.

The strength in using the finite strain tensors is that they are independent of rigid rotation [37], which does not apply to the infinitesimal strain tensor.

A common way to predict the nonlinear stress is through the *factorized K-BKZ equation*

$$\boldsymbol{\sigma} = - \int_{-\infty}^t M(t-t') \left[\frac{\partial W(I_1, I_2)}{\partial I_1} \boldsymbol{\gamma}_{[0]} + \frac{\partial W(I_1, I_2)}{\partial I_2} \boldsymbol{\gamma}^{[0]} \right], \quad (1.37)$$

where I_1 and I_2 are the first and second invariants of the *Finger strain tensor* $\mathbf{B} = \mathbf{E} \cdot \mathbf{E}^\dagger$. W is called the *potential function* for which the following is required

$$\left(\frac{\partial W}{\partial I_1} \right)_{3,3} + \left(\frac{\partial W}{\partial I_2} \right)_{3,3} = 1. \quad (1.38)$$

Since the K-BKZ class of equations is very broad [38], it is useful to consider the specific polymer structure before defining W . Hence, in the special case of polymer networks, it is very important to consider the presence of both, temporary and permanent entanglements and cross-linkers.

1.5 An Outline of this Thesis

The primary objective of this thesis is to analyze the mechanical behavior of soft polymer networks. The motivation for this arose from the adhesive industry, and their increased usage of polymer networks as PSAs. As the project progressed, it became obvious to make a more general rheological study of polymer networks, which incited the title of the thesis. The study will be primarily experimental, however, a theoretical approach has also been included.

In **chapter 2** we relate linear viscoelastic measurements of cross-linked networks to the debonding mechanism in peel experiments. The viscoelastic parameters obtained from SAOS measurements are used to define an empirical relation for the peel force.

As deformations of skin adhesives during removal are highly nonlinear, a need for analyzing elongational experiments appeared. Commonly uniaxial measurements are used for such analysis, however, there are some shortcomings for this type of deformation when looking at PSAs. We commonly divide elongational experimental techniques into three classes, that is; 1) Rotational clamp rheometry [50, 51], 2) filament stretch rheometry [48, 51] and 3) wind-up drum rheometry [49]. Due to the sticky nature of the PSAs the first technique with rotary clamps is found inconvenient. The second technique is often used with either dog-bone or cylindrical samples. Dog-bone samples are easily made with PSAs, however, as PSAs are very soft and flexible at room temperature, such samples are difficult to handle and mount in a FSR. On the other hand, cylindrical samples would be easier to handle, and have proven to give much more accurate results in uni-axial elongation. Unfortunately cylindrical samples must be molded, which is not possible for PSAs since they would stick to the mold. Finally we consider the wind-up drum technology. Using this technology we can measure elongational stresses with a small sample volume. However, an extensive analysis of this instrument has proven that it does not always measure uniform uniaxial elongation [52, 53], in particular the theoretical work done by Yu *et al* [53], shows that elastomeric materials result in a combined planar and uniaxial behavior.

To overcome these shortcomings a new fixture has been designed to measure uniform planar elongation, and we introduce this in **chapter 3**. Another reason for this alternative approach is that observations of the peel front in peel experiments indicate that the deformation is more planar than uniaxial. The fixture is called *Planar elongation fixture* (PEF) and is designed as an add-on to the FSR. It is constructed in such a way that we can exploit the sticky nature of the samples. The new measuring technique is validated using particle tracking, digital imaging and finite element simulations (FEM).

In **chapter 4** we use the PEF to analyze the elastic behavior of polymer networks, this is done using large-amplitude reversible elongational (LARE) flow. The analysis is motivated by the work done by Nielsen *et al.* [54] and Bejenariu *et al.* [55], who could measure the elastic recovery strain in reversible uniaxial elongation.

Finally a theoretical study of polymer networks has been initiated. This is introduced in **chapter 5**, where we use a self-consistent mean-field slip-link model as a theoretical approach to investigate the structural and entanglement influence on the mechanical properties. This work was performed in collaboration with Prof. J.D. Schieber at Illinois Institute of Technology.

A brief summary will be presented in **chapter 6** together with a discussion about the findings in the previous chapters. In particular we will elaborate on the observations that have lead to new and yet unanswered questions.

Chapters 2-5 are written in the format of scientific articles including separate abstracts and conclusions, to rationalize the process of publishing.

Chapter 2

Linear Rheology of Cross-linked PPO as a PSA

Soft polymer networks are commonly used as pressure sensitive adhesives (PSAs). This is due to their unique ability to deform and yet to resist flow. These contradictory requirements indicate that the mechanical properties are finely tuned, and that the types of deformation upon application are carefully considered. Two main mechanisms must be considered when studying adhesives, that is; the debonding and bonding mechanisms. Linear rheology is used to study the debonding mechanisms to gain better understanding of the peeling process of the PSAs. A variety of PSAs are prepared by mixing a linear vinyl terminated polymer with a silane terminated f -functional cross-linker, with $f > 2$. The stoichiometric imbalance, r (silane to vinyl ratio), the molecular weight of the linear polymer, M , and the cross-linker functionality, f , are used as adjustable parameters to tune the properties of the cross-linked networks. The adhesive performance was tested with 90 degree peel tests at three peel rates and thicknesses, and it was observed that the peel force varies with r , M and f and also the peel rate. The fundamental viscoelastic parameters that govern the PSA performance of cross-linked systems were used to state an empirical relation for the peel force. The relation is combining the peel force with the loss tangent at the peel frequency and the equilibrium modulus. Based on this, basic guidelines for selecting the appropriate polymer/cross-linker system to achieve the target performance are given¹.

2.1 Introduction

Pressure sensitive adhesives (PSAs) are probably the most common class of adhesives in consumer products. In fact self-adhesive tapes and labels of all

¹This part of the work has been published in Int. J. Adhesion and Adhesives 29 (2009) 687–693. Minor modifications have, however, been made here.

kinds are ubiquitous products in everyday life. However, the understanding of the rheological properties upon application is limited [2]. It is especially the rheological properties upon removal/debonding of the adhesive that remains as a challenge, and although several studies have focused on such relations there is still a lack of knowledge on the field of interfacial failure mode upon debonding [2, 3, 9, 11, 13, 15, 17, 36, 56, 57].

For medical purposes the PSAs should be soft viscoelastic solids. Soft, because they should be able to adapt to rough surfaces, for example human skin, and solid, because they should be able to resist flow to other parts than the predetermined contact area. Hence, PSAs should be designed with an adjusted balance between flow and resistance to flow. Most modern PSAs are therefore made of cross-linked polymers. The fundamental property is simply that there is a difference in the energy gained in forming the interfacial interactions and the energy dissipated during debonding [2].

One of the most often measured characteristics of PSAs is the resistance to peel, *i.e.*, the force required to peel a strip of adhesive from a given substrate [9]. Many researchers have studied the peel performance over the years, and it is especially the influence of peel rate and temperature that has been given much attention [9, 10, 14, 57, 58]. In standard peel tests the adhesive is peeled at constant rate, and it is expected to peel off cleanly from the substrate without leaving any noticeable residue. However, in some cases the adhesive breaks into fibrils that will elongate and fail cohesively, *i.e.*, the adhesive will break in the bulk. The first type of failure mode is called adhesive, while the latter one is called cohesive. Usually failure modes other than adhesive are considered as a sign of faulty product design.

The mechanisms for the two modes of failure are quite different, and the transition from one mode to another has been found to be very complex. For example some materials can exhibit both failure modes depending on the peel rate and temperature used, and the type of failure is thus, not only a matter of production design, but also a matter of application and usage [9].

This study will focus on the bulk rheological properties, *i.e.*, how changes in the bulk composition affect the resistance to peel and failure mode from a rheological perspective.

One way to test this is by changing the cross-link density in the bulk. Gent *et al.* [18] found that the peel force decreases as the cross-link density increases. They ascribed this decrease to a reduction of molecular inter-diffusion. This phenomenon will be examined further here by varying the cross-link density for different polymer/cross-linker systems. It will furthermore be shown how linear viscoelastic properties can be used to examine the PSA performance. This has already been done by Yang [32], who looked at the linear viscoelastic behavior of PSAs and the energy involved during peeling. He found that in the case where the surface energy is small, the peel strength is proportional to the ratio of G''/G' , where G'' is measured at the peel frequency and G' at the bonding frequency. Motivated by Yang's results a comparison between viscoelastic data and peel data will be performed. The approach and argumentation will, however, be slightly different.

2.2 Experimental

Two types of experiments are performed. One to determine the viscoelastic properties of the samples, and one to determine the resistance to peel from a given substrate. A description of these experiments will be given in section 2.2.2 and 2.2.3, while section 2.2.1 will be on the sample preparation.

2.2.1 Sample Preparation

The PSAs were prepared by mixing a linear vinyl terminated polypropylene oxide (PPO) manufactured by Kaneka Corp., with a silyl-terminated f -functional polysiloxane cross-linker with $f > 2$. Sketches of the polymer and cross-linker are shown in figures 2.1 and 2.2.

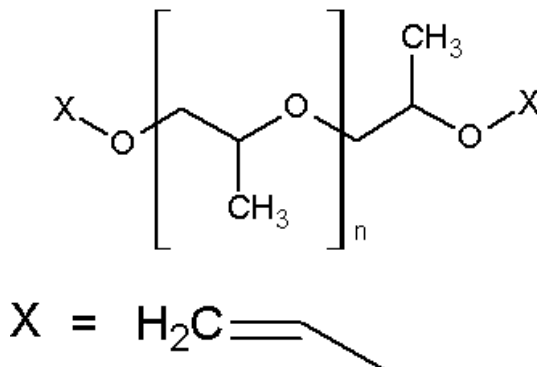


Figure 2.1: A sketch of the linear vinyl terminated PPO.

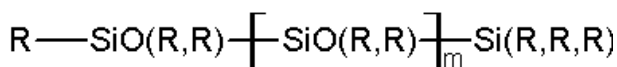


Figure 2.2: A sketch of the f -functional polysiloxane cross-linker. At least three of the R-groups in the squared bracket are hydrogen such that $f \geq 3$. The rest of the groups are each independently selected from C_{1-12} -alkyl, C_{3-8} -cycloalkyl, C_{6-14} -aryl and C_{7-12} -arylalkyl.

The reaction is catalyzed with a Pt catalyst. The molecular weight distribution of the linear polymers is measured with size exclusion chromatography (SEC) with triple detectors: Refractometer, light scattering photometer and viscometer. The instrument used is Viscotek Trisec model 302 and the pumping system is Viscotek GPCmax. Two sec columns, packed with 5 μm mixed pore size (mixed-D) PLgel particles from Polymer Laboratories were used in series. The cross-linkers were characterized by gel permeation chromatography (GPC), the system used was Viscotek model 200, and the columns were PLgel 5 μm mixed-D (as in the SEC). THF was used as the solvent, and a polystyrene

Table 2.1: Molecular weight distributions of the polymers A1 and A2, and the cross-linkers B1 and B2, measured with a SEC triple detector and GPC respectively.

Polymer	Name	M_n	M_w	PDI	f
PPO	A1	16046	18930	1.18	~ 2
	A2	10492	15122	1.44	~ 2
Polysiloxane	B1	1890	3050	1.61	~ 8
	B2	1310	1790	1.36	~ 5

calibration curve was used for characterization. The measured molecular weight distributions are listed in table 2.1.

Test samples were prepared with different ratio of functional groups, r . This is a very important network parameter also defined as the stoichiometric imbalance:

$$r = \frac{\text{no. of silane groups}}{\text{no. of vinyl groups}} = \frac{f[A_f]}{2[B_2]}, \quad (2.1)$$

f is the cross-linker functionality and $[\dots]$ denotes molar concentrations. The samples should be soft viscoelastic solids. For this reason, r is chosen to be close to, but larger than the lower critical degree of cross-linking, r_c , given by equation 2.2 [25–27]. For a more general discussion on the influence of r on the rheological properties, see Larsen *et al.* [23].

$$r_c = \frac{1}{f-1}. \quad (2.2)$$

All the samples are named SX followed by the abbreviations for the polymer and cross-linker respectively. These are listed in table 2.1. Finally the samples names are terminated with a number specifying the ratio, r . An overview of all the samples is given in table 2.2.

The samples were prepared in a static mixer to avoid air bubbles, hereafter they were pressed in desired thicknesses in a 100°C hot-press between two sheets of release liner for dynamic mechanical testing, or one sheet of release liner and a backing foil for peel tests. All samples were then cured at 100°C for one hour to make sure that the mixture has fully reacted before further analysis.

2.2.2 Linear Viscoelasticity

Small amplitude oscillatory shear (SAOS), were measured in a controlled stress rheometer (AR2000, TA instruments), set to a controlled strain mode with 10% strain, which has been chosen based on strain sweep tests. The linear spectra were measured with parallel plate geometry of 25 mm in diameter, and the experimental temperature and frequency range were 32 to 100°C and 0.01 to 100 Hz respectively. Time-temperature superposition (TTS) was used to

Table 2.2: Overview of the 15 test samples.

(A1/B2) $M_n = 16$ kDa $f \simeq 5$		(A1/B1) $M_n = 16$ kDa $f \simeq 8$	
Name	r	Name	r
SX.A1B2.01	0.46	SX.A1B1.01	0.41
SX.A1B2.02	0.50	SX.A1B1.015	0.43
SX.A1B2.03	0.53	SX.A1B1.02	0.45
SX.A1B2.04	0.56	SX.A1B1.03	0.48

(A2/B2) $M_n = 10$ kDa $f \simeq 5$		(A2/B1) $M_n = 10$ kDa $f \simeq 8$	
Name	r	Name	r
SX.A2B2.01	0.54	SX.A2B1.01	0.41
SX.A2B2.02	0.56	SX.A2B1.02	0.44
SX.A2B2.03	0.59	SX.A2B1.03	0.47
SX.A2B2.04	0.62	-	-

obtain rheological master-curves over a wide frequency range with $T = 32^\circ\text{C}$ as the reference temperature. The master-curves are obtained by plotting $G_r^* \equiv G^*(T) \cdot b_T$ vs. $\omega_r \equiv a_T \cdot \omega$, where the vertical shift factor b_T is given by T_{ref}/T and a_T is given by an Arrhenius dependency:

$$a_T = \exp \left[\frac{-\Delta \bar{H}}{R} \left(\frac{1}{T} - \frac{1}{T_{ref}} \right) \right] \quad (2.3)$$

$\Delta \bar{H} < 0$ is the activation energy for flow, R the ideal gas constant, T the temperature in Kelvin and T_{ref} the reference temperature in Kelvin. The shift factor a_T from 333 K is found to be 0.25, while the shift factor from 373 K is 0.07.

2.2.3 Peel

The adhesive performance was investigated using 90° peel experiments on a texture analyzer (TA.TX.plus). The adhesive was applied to a stainless steel plate with slight pressure using a 2 kg roller, and left at rest for 30 min. The flexible backing foil was supported by an extra tape to avoid deformation of the backing during peel.

The adhesive strip was attached to a force transducer that moves in the z -direction with velocity V . The substrate was located in the xy -plane, and displaced in the x -direction with velocity V , as the force transducer moves upwards with the same velocity. A 2D sketch of the xz -plane is shown in figure 2.3 where the peel is being peeled off the substrate in the vertical z -direction to obtain a 90° peel.

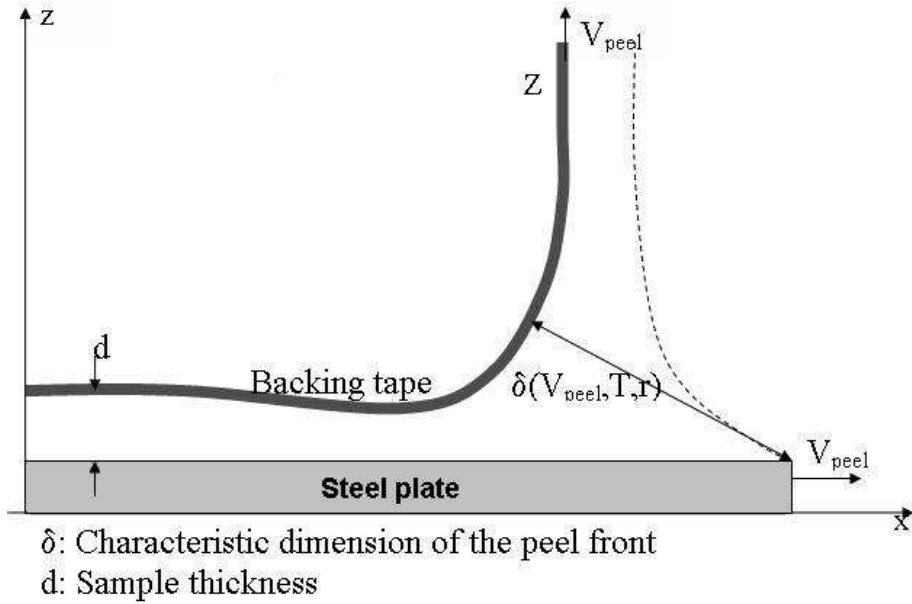


Figure 2.3: Sketch of a 90° peel test setup, side-view of the xz -plane.

2.3 Results and Discussion

2.3.1 Small amplitude Oscillatory Shear Data

The SAOS result obtained for SX.A1B2.03 are shown in figure 2.4. It is seen that the sample is a viscoelastic solid, since it behaves like an elastic solid at low frequencies, where G' reaches a plateau and is orders of magnitudes larger than G'' , while the response is viscoelastic at higher frequencies, where G' and G'' are of the same order of magnitude. The low frequency plateau for G' is a signature of cross-linked systems as opposed to uncross-linked systems. The general trend is that the plateau reached by G' at low frequencies increases as the value of r increases, but it also depends on the polymer/cross-linker system used. The plateau modulus, G_0 , is also known as the equilibrium modulus.

Winter and Chambon [45, 46] proposed that the relaxation modulus for

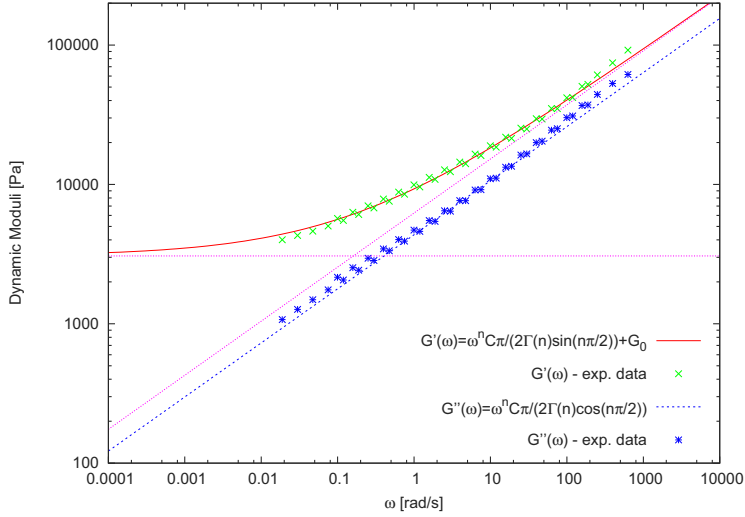


Figure 2.4: Dynamic moduli for SX.A1B2.03 obtained from SAOS experiments. Crosses represents the storage modulus while circles represents the loss modulus. The solid lines represent a fit of equations 2.6 and 2.7 to the data. The dashed lines represent the viscous and elastic contributions to the storage modulus respectively.

polymers at the transition between a viscoelastic liquid and a viscoelastic solid is given by

$$G(t) = St^{-n} \quad (2.4)$$

This transition state is called the gel point (GP), and equation 2.4 is commonly referred to as the gel equation. The corresponding dynamic moduli have been found to be congruent over a large frequency range in the stoichiometrically balanced case ($r = 1$) [45] and parallel in the stoichiometric imbalanced case ($r \neq 1$) [46] and the viscosity is infinite while the equilibrium modulus is zero. Hence, an elastic response at low frequencies such as the one in figure 2.4 will not be observed. It is thus necessary to add an additional term to the gel equation to fit the experimental data so that

$$G(t) = St^{-n} + G_0 H(t). \quad (2.5)$$

The additional term is defined as a step function, where $H(t)$ is the Heaviside step function. In this way it only carries a non-zero and positive value at times above zero. This positive value is given by the plateau modulus, G_0 . Besides the plateau modulus, equation 2.5 consists of two material constants, n and S . n is a critical relaxation exponent and makes $G(t)$ drop faster the higher it is, *i.e.*, the relaxation process increases with n . S is commonly called the gel stiffness. It is, however, important not to confuse it with the chemically cross-linked network. It is rather a measure of the number of entanglements present, and thus more sensitive to the molecular weight of the linear polymers than to the functionality of the cross-linkers, which we will see later.

From equation 2.5 it is possible to derive the corresponding expressions for G' and G'' :

$$G'(\omega) = \omega \int_0^\infty G(s) \sin(\omega s) ds = \frac{S\pi\omega^n}{2\Gamma(n) \sin \frac{n\pi}{2}} + G_0 \quad (2.6)$$

$$G''(\omega) = \omega \int_0^\infty G(s) \cos(\omega s) ds = \frac{S\pi\omega^n}{2\Gamma(n) \cos \frac{n\pi}{2}} \quad (2.7)$$

The red line and blue dashed line in figure 2.4 represent a fit of equations 2.6 and 2.7 to the measured dynamic moduli. The pint lines represent the individual contributions from the two terms given in equation 2.6. It is seen that G' and G'' would be parallel if the second term was not included.

The fitted results for G_0 , S and n vs. r are shown in figure 2.5. In figure 2.5.A it is observed that G_0 increases as r and f increases. This is assigned to the expectation that the number density of cross-links increases as r and f increases. It is also seen that G_0 increases as the molecular weight of the linear polymer increases, this is because the number of trapped entanglements, which perform as artificial cross-links, are increased. The story is different for S . It is seen that the circles and pluses as well as the asterisks and crosses in figure 2.5.B seem to follow two curves, one for each molecular weight of the linear polymers. This indicates that f has little influence on S , while it is highly dependent on the molecular weight of the polymers. n seems to behave in the same way as S , *i.e.*, it also divides into two separate curves for each molecular weight, as seen in figure 2.5.C. However, it does not increase with molecular weight, but decreases at corresponding values of r . Hence, the softer the network is, the higher n , which corresponds to a faster relaxation process. For $r = 1$ and at the gel point, $n = 0.5$ [45]. It is thus, observed that n can be increased, compared to a stoichiometrically balanced gel-point, by adjusting r , and then still have a gel.

It is evident from figure 2.5, that the 15 test samples cover a broad spectrum of rheological properties. The task is now to see how the rheological parameters affect the PSA performance.

2.3.2 Peel Data

The peel force is measured at three peel rates, $V = \{0.1, 1, 5\}$ mm/s, and three sample thicknesses, $d = \{100, 300, 1000\}$ μm , for each of the 15 test samples. In figure 2.6 the peel forces, F_{peel} , measured for the SX.A1B2 series are shown. It is seen that F_{peel} increases with both, increasing thickness and peel rate, which was expected according to refs. [3, 9, 10, 14, 57–59]. It is furthermore seen that SX.A1B2.01 have lower peel forces than SX.A1B2.02, 03 and 04 at corresponding values of the peel rate, and it was noted during the experiments that SX.A1B2.01 peeled off cohesively, while SX.A1B2.02, 03 and 04 peeled off adhesively. Different failure modes result in very different peeling mechanisms, and the results for SX.A1B2.01 are therefore, not directly comparable to the others in the same series. From the remaining three samples, which exhibit

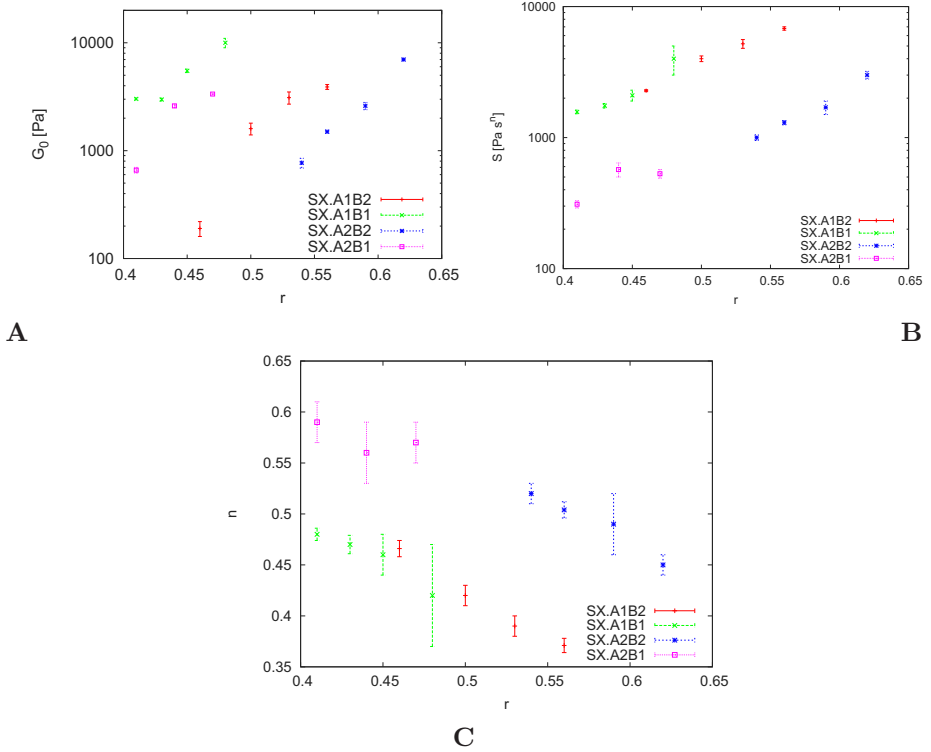


Figure 2.5: (A) G_0 (B) S and (C) n vs. r obtained from a least square fit of equations 2.6 and 2.7 to experimental SAOS data.

adhesive failure, it is observed that the peel force decreases as the value of r increases.

2.3.3 Dimensional Analysis

It is desired to address the linear viscoelastic properties to the peel process. We initialize this by considering the debonding mechanism. The focus will thus, be on how the gels deform when peeling from a substrate. Clearly the sample will be stretched at the peel front, and it was observed during the peel experiments that the characteristic dimension, δ (see figure 2.3), of the peel front increases with peel rate. This change in δ relates to the viscoelastic character of the sample. It is common to argue that this work performed during stretching, is proportional to the dissipated energy due to the viscous nature of the samples. The loss modulus, $G''(\omega)$, is a measure of the dissipated energy, and the force needed to peel of the adhesive is therefore, proportional to $G''(\omega)$ measured at the peel frequency, ω_{peel} . It has furthermore been observed [3, 9, 59] that the peel force scales with the sample dimensions, *i.e.*, the thickness, d , and width, W , of the sample. The following proportionality can therefore be stated for the

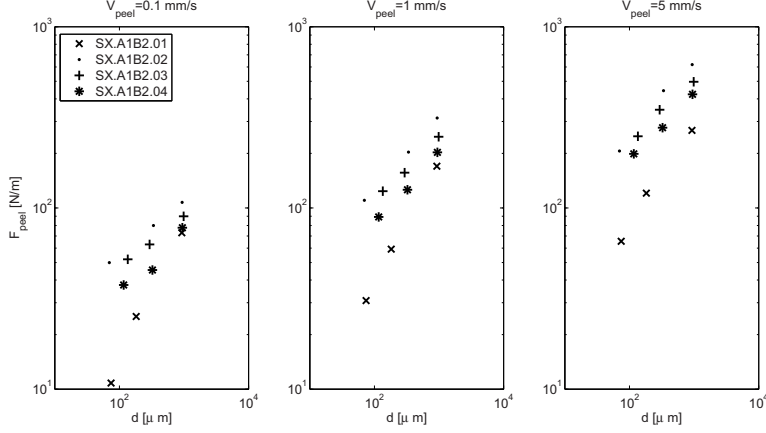


Figure 2.6: The peel force measured for the SX.A1B2 series. The force is plotted vs. sample thickness, d , and shown for each peel rate, V_{peel} .

peel force:

$$\frac{F_{peel}}{dW} \propto G''(\omega_{peel}), \quad (2.8)$$

where ω_{peel} is defined as V_{peel}/d . In figure 2.7 the peel force measured for series SX.A1B2 is plotted versus the loss modulus at the peel frequency. It is seen that for each stoichiometric ratio the data show a nice correlation between F_{peel} and $G''(\omega_{peel})$. However, the slope of the lines, changes with r .

As r is changing, the balance between the viscous and elastic parts of the sample is shifted. It is evident from figure 2.7, that the elastic network also affects the PSA performance, why equation 2.8 should be rewritten to include both viscous and elastic contributions. A very good measure for the balance between the two dynamic moduli is the loss tangent, $\tan \delta$. Hence, the loss modulus measured at the peel frequency is replaced with the loss tangent, measured at the same frequency, in equation 2.8. It is, however, not certain that the peel force is directly proportional to the loss tangent. It should therefore be written as a function: $g(\tan \delta_{\omega_{peel}})$. The loss tangent is a dimensionless measure and it is therefore convenient to normalize the peel force with the plateau modulus, G_0 , such that both sides of the following equation become dimensionless. G_0 is the dominant rheological response at low frequencies, and thus, a measure for how well the sample adapts to a given substrate. Hence, by including G_0 , both bonding and debonding mechanisms are included, and the relation given in equation 2.9 represents a finely tuned balance between the elastic and viscous properties.

$$\frac{F_{peel}}{dWG_0} \propto g(\tan \delta_{\omega_{peel}}) \quad (2.9)$$

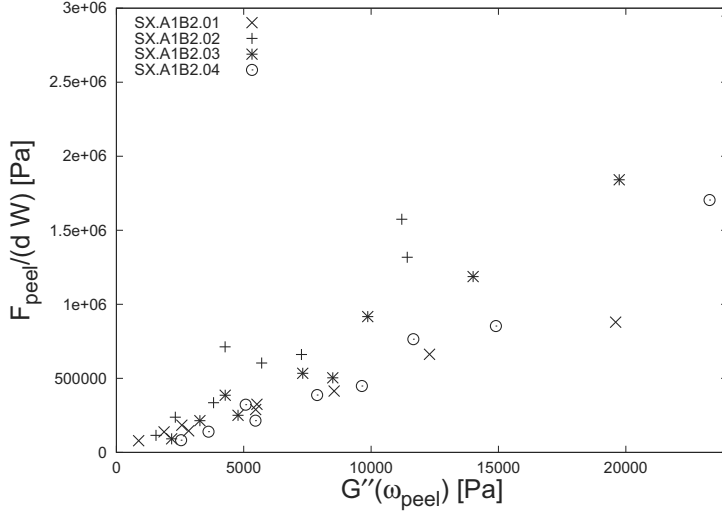


Figure 2.7: The measured peel force for the SX.A1B2 series divided by the sample dimensions, d and W . It is plotted vs. the loss modulus measured at the peel frequency, $G''(\omega_{peel})$.

SX.A1B2

Figure 2.8 shows the normalized peel force for the SX.A1B2 series vs. the loss tangent measured at the peel frequency. The standard deviation computed from three supposedly identical samples is less than the size of the markers, hence, no error-bars are drawn. It is seen that the data divide into two separate universal curves: One for cohesive debonding and one for adhesive debonding. Hence, there is a very nice correlation between the peel force, the loss tangent, and the plateau modulus, and it seems like the relation distinguishes between failure modes. Figure 2.9 show the equivalent results for the remaining three series. The results are comparable to those observed in figure 2.8, however with some deviations, which will be discussed in the following.

SX.A1B1

All the samples in the SX.A1B1 family showed adhesive failure during experiments. The results obtained using the empirical equation 2.9 are seen in figure 2.9.A. The data collapse into one curve, except those measured for the SX.A1B1.01 samples. For systems peeling adhesively it is expected that the peel force decreases as r increases. It is thus not clear why the crosses in figure 2.9.A lies below the others. To clarify this matter it is necessary to perform a chemical characterization of the network, for example by swelling. This will not be done in this study and for this reason the SX.A1B1 data will not be included in the final comparison.

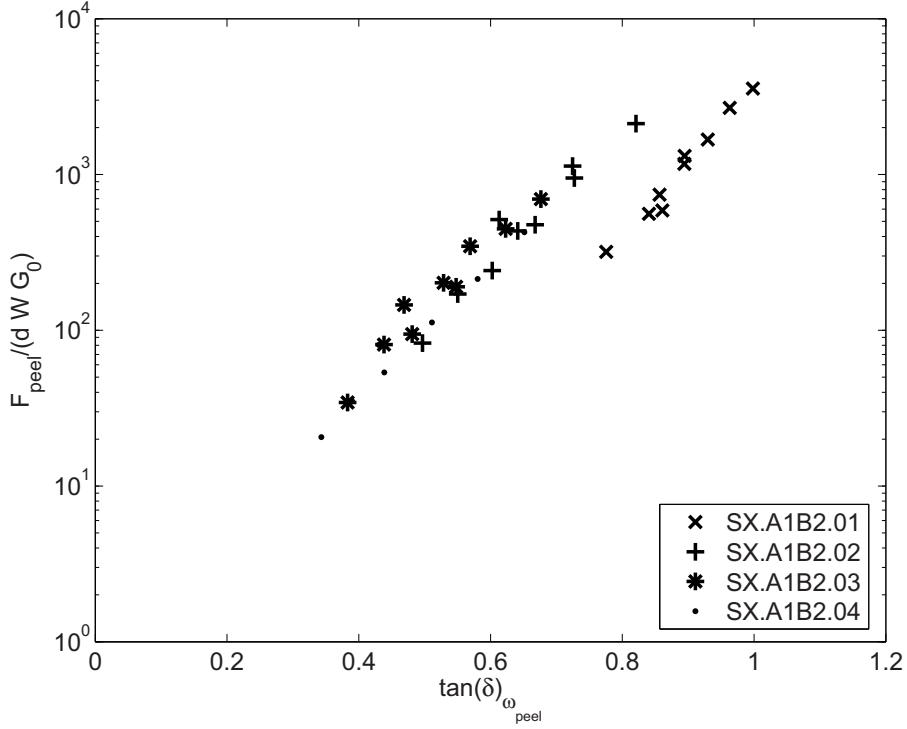


Figure 2.8: The normalized peel force vs. the loss tangent measured at the peel frequency. The data is from the SX.A1B2 series. The error-bars are smaller than the marker size, which is why these are not included.

SX.A2B2 and SX.A2B1

The data for family SX.A2B2 and SX.A2B1 show good correlation between the peel force, loss tangent and plateau modulus as seen in figure 2.9.B and C.

Summary

To summarize the results from the four previous sections it is seen that each sample family show a good correlation between $\tan \delta_{\omega_{peel}}$ and the normalized peel force. It is however necessary to distinguish between adhesive and cohesive failure mode. All the data obtained for the samples performing adhesive failure are compared in figure 2.10. It is seen that for $\tan \delta_{\omega_{peel}} \rightarrow 0$ all the data seem to collapse into one curve, while as $\tan \delta_{\omega_{peel}}$ increases the data spread out for each family of test samples. This indicates that a universal curve can be obtained with linear rheology for this particular chemistry at low $\tan \delta_{\omega_{peel}}$, while more information is needed to account for the differences at higher $\tan \delta_{\omega_{peel}}$.

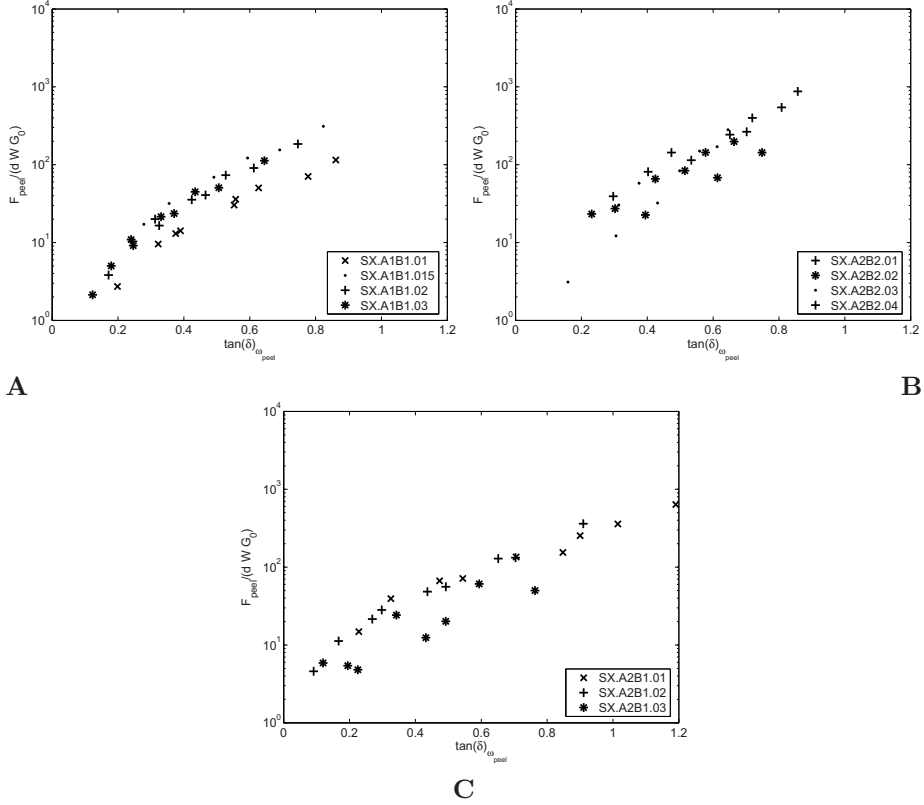


Figure 2.9: The normalized peel force vs. the loss tangent measured at the peel frequency. (A) SX.A1B1 series, (B) SX.A2B2 series, and (C) SX.A2B1 series. The errorbars are smaller than the marker size, which is why these are not included.

2.3.4 Viscoelasticity of PSAs

Equation 2.9 indicates that in order to improve peel strength, it is necessary to increase the loss tangent at the peel frequency, *i.e.*, increase G'' relative to G' . Furthermore the equation might give the impression that F_{peel} could be increased by increasing G_0 . However, $\tan \delta$ and G_0 are dependent variables, which mean that by increasing G_0 , $\tan \delta$ will decrease. In reality F_{peel} increases by decreasing G_0 , since the sample then becomes more soft and adapts better to the substrate.

2.4 Conclusion

An empirical relation between the viscoelastic parameters and the PSA peel properties has been developed. The relation was developed by considering the viscoelastic behavior during debonding, and it was found that the resistance

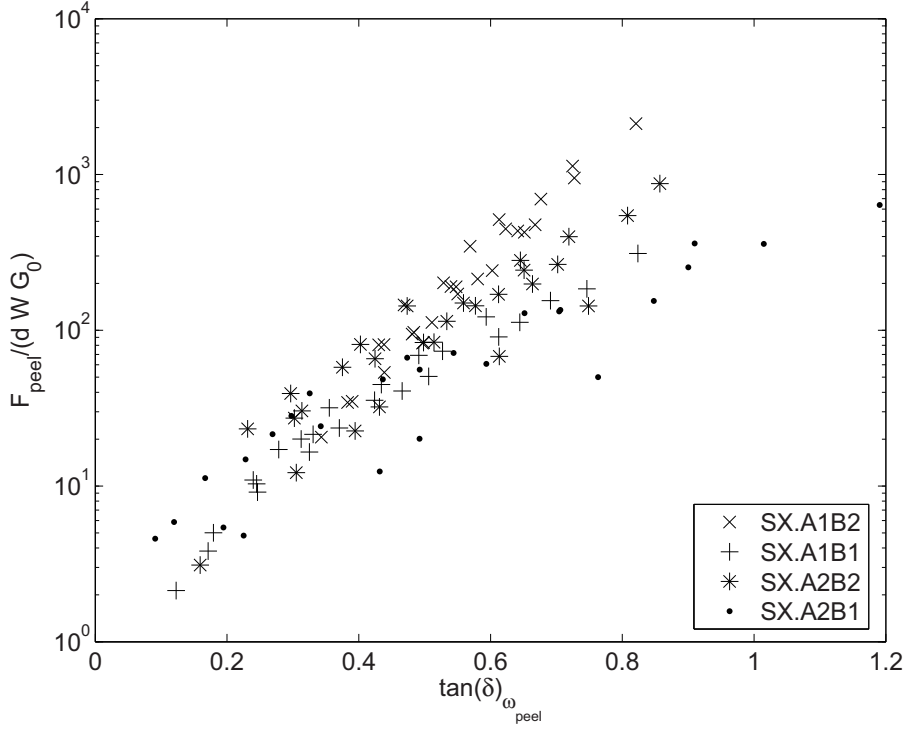


Figure 2.10: The normalized peel force vs. the loss tangent measured at the peel frequency.

to peel is proportional to the peel strip dimensions, *i.e.*, thickness and width, and to the loss modulus at the peel frequency. However, the motivation was to connect the bulk rheological properties to the peel data as well. This was done by replacing the loss modulus with the loss tangent, such that the energy stored in the elastic network was included as well. The peel force was furthermore normalized with G_0 . By this normalization the peel data, showing adhesive failure shifted into one universal curve, for each series of PPO networks.

The empirical relation was tested with four sets of experimental data, for which the molecular weight of the linear polymer or the cross-linker functionality were used as adjustable parameters. It showed a very nice correlation between the peel data and the viscoelastic data for each set and it furthermore separated the data into different failure modes. A comparison between all the data sets performing adhesive failure showed a congruency as $\tan \delta_{\omega_{peel}} \rightarrow 0$, while they separated into four curves of exponential nature at intermediate values of $\tan \delta_{\omega_{peel}}$. The exponents of these curves varied in size depending on the molecular weight or cross-linker functionality respectively. We believe that the behavior observed for intermediate $\tan \delta_{\omega_{peel}}$, is related to the nonlinear behavior of the material, namely strain hardening. This believe is based on comparisons between the normalized peel force at corresponding loss tangents,

where it is observed that, as the cross-link density decreases the normalized peel force increases. It is therefore, of natural importance to investigate the nonlinear rheological behavior of the PPO networks, which will be done in the following chapters.

Chapter 3

Planar Elongation of Soft Polymeric Networks

A new test fixture for the filament stretch rheometer (FSR) has been developed to measure planar elongation of soft polymeric networks with application towards pressure-sensitive adhesives (PSAs). The concept of this new geometry is to elongate a tube-like sample by keeping the perimeter constant. To validate this new technique, soft polymeric networks of poly(propylene oxide) (PPO) were investigated during deformation. Particle tracking and video recording were used to detect to what extent the imposed strain rate and the sample perimeter remained constant. It was observed that, by using an appropriate choice of initial sample height, perimeter, and thickness, the planar stretch ratio will follow $\lambda(t) = h(t)/h_0 = \exp(\dot{\epsilon}t)$, with $h(t)$ being the height at time t and $\dot{\epsilon}$ the imposed constant strain rate. The perimeter would decrease by a few percent only, which is found to be negligible. The ideal planar extension in this new fixture was confirmed by finite element simulations. Analysis of the stress difference, $\sigma_{zz} - \sigma_{xx}$, showed a network response similar to that of the classical neo-Hookean model. As the Deborah number was increased, the stress difference deviated more from the classical prediction due to the dynamic structures in the material. A modified Lodge model using characteristic parameters from linear viscoelastic measurements gave very good stress predictions at all Deborah numbers used in the quasi-linear regime¹.

3.1 Introduction

Polymer networks are well-known in many applications, ranging from hard and brittle rubbers to soft and fragile gels. The area of soft polymer networks has

¹This part of the work has been published in Rheol. Acta, published online: 2 September 2009. Minor modifications have been made here.

obtained increasing attention due to the use of the gel-like materials as e.g., matrices for drug-delivery systems and implants [4, 5].

Soft polymer networks are, from a physical point of view very interesting materials since they possess properties of both viscous and elastic character, and the dominating behavior depends on the applied time scale. However, soft polymer networks close to the critical gel condition are very difficult to handle, and experiments have to be carefully designed in order to avoid destruction of the material. Melts can usually be measured repeatedly if allowed enough time to equilibrate while soft networks can easily be irreversibly destroyed.

Soft networks can be regarded as imperfect networks where the completion of the cross-linking reaction is either hindered by stoichiometry (i.e., an excess of one of the components) or inhibition of the cross-linking reaction [45]. The softness of the network is a result of a large fraction of dangling substructures, dangling arms, and soluble structures not connected to the infinite network. These species give rise to dynamics of the network not encountered for highly cross-linked networks such as rubbers. Depending on the stoichiometry of the system, the dangling sub-structures and soluble sub-structures (also called the sol fraction) will have a range of compositions of linear and branched molecules [33]. For a detailed description of stochastic models describing this composition, see references [22, 25–27].

Wagner and Schaeffer [60] argued that rubbers and polymer melts generally have similar mechanical properties. However, real elastomers are inhomogeneous in network structure due to the permanent ordering of polymeric chains around the cross-linking points, whereas melts of long chain polymers have uniform network-like structures on short time scales, although the network structures are not permanent but transient. Soft networks, which consist of both permanent cross-links and transient entanglements, may be expected to behave as an entangled melt at certain time scales, but on long time scales, they will behave as rubbers.

The aim of this work is to construct an apparatus that can measure planar elongation stresses of soft polymeric networks as pressure sensitive adhesives (PSAs), without the application of rotary clamps [61]. The reason for this is the sticky nature of the samples, which makes rotary clamps unsuitable. Planar elongational measurements on relatively soft silicone networks have been performed by Mark *et al.* [7] and Urayama [35] by deforming a thin film fixed by clamps. These clamps will keep one dimension fixed during deformation. This is however, a measurement that is very hard to perform since the samples can adhere to the clamps and because it is hard to limit the deformation to two directions only.

A new fixture has been designed as an add-on to the filament stretch rheometer (FSR) [48]. This was done in such a way that we exploit that the samples are sticky. The concept for the test method is motivated by the work of Laun and Schuch [62], who introduced an apparatus for measuring planar elongation viscosities by drawing of a tube-like sample. Here, the perimeter of the sample is kept constant by pumping oil from a syringe into the core of the tube, while the outer pressure is controlled by a surrounding oil bath. The work done by

Laun and Schuch will be simplified here such that no surrounding media is used, nor is the diameter fixed by pumping oil into the cylinder. Details about the FSR can be found in the work done by Bach *et al.* [63].

To evaluate the performance of this new test fixture, we use particle tracking, as well as imaging the deviation from an ideal cylinder extension. The experiment will furthermore be analyzed with finite element simulations to study the consequences of operating the device without imposing a pressure difference on the inner and outer sides of the cylinder.

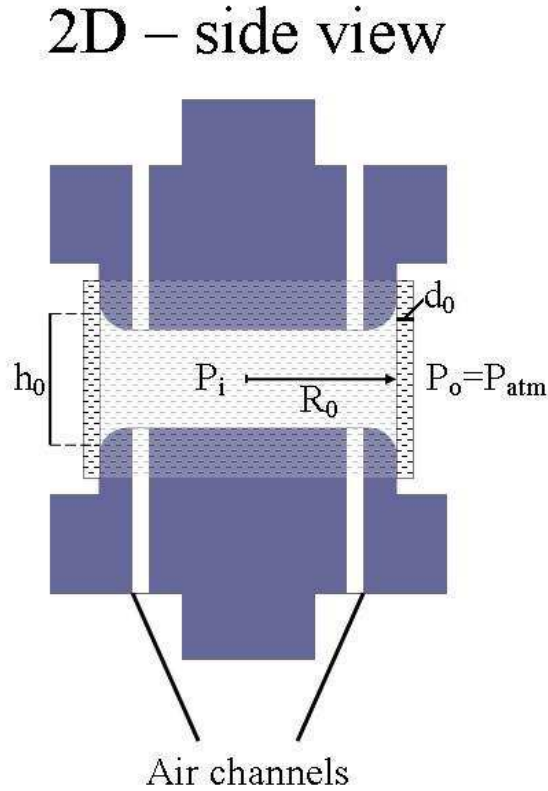


Figure 3.1: Sketch of the add-on fixture. It consist of two disks, an upper and a lower. A thin sample, of an initial thickness, d_0 , is wrapped around the two disks to form a hollow cylinder, with a radius of R_0 . The distance between the upper and lower contact perimeter, between the sample and fixture is h , where the initial distance is h_0 .

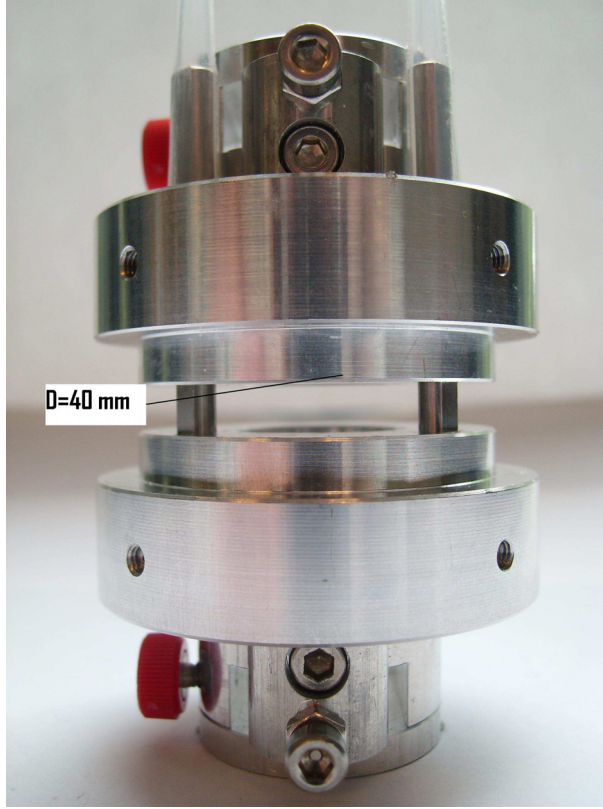


Figure 3.2: The Planar Extension Fixture (PEF)

3.2 The Planar Elongation Fixture

A sketch of the test fixture is shown in figure 3.1, while a photo of it is shown in figure 3.2. A thin sample strip, of initial thickness, d_0 , height, h_0 , and length L_0 is wrapped around the two disks to form a hollow cylinder with an inner radius of R_0 . The length, L_0 , of the sample is slightly larger ($\sim 7\%$) than the perimeter ($2\pi R_0$). This is to ensure an overlap where the two sample ends meet so the cylinder is properly sealed. The fixture is built to measure elongational stresses on self-adhesive materials, and in most cases, no extra clamps are needed to hold the sample strip in place. However, in some cases, the force needed to elongate the sample exceeds an upper limit for what the adhesive can withstand, and the PSA will begin to slide on the fixture surface. In such cases a rubber band can be used to prevent slippage between the fixture and the PSA. There are two air channels in both disks to allow airflow into the cylinder to equalize the inner and outer pressures.

During an experiment, the disks are pulled apart by moving the upper disk with a specified velocity profile.

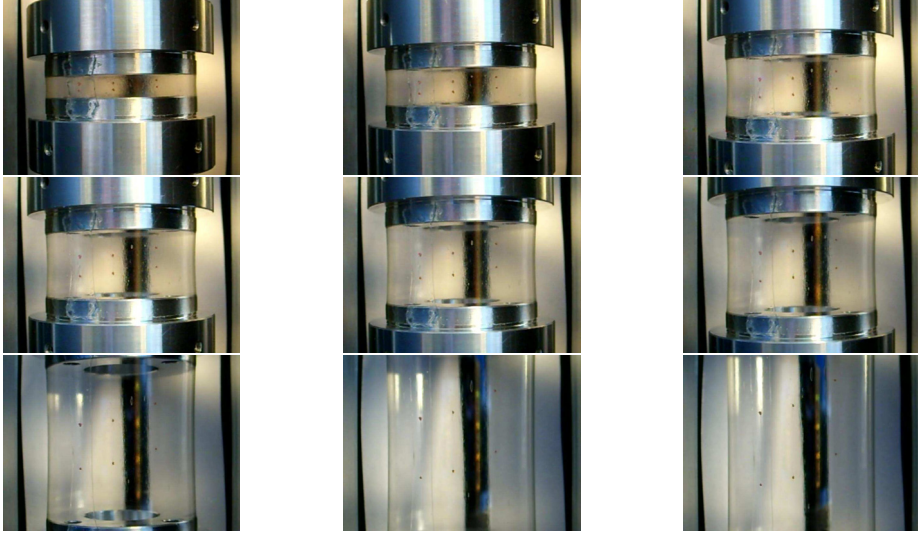


Figure 3.3: Snapshots of test 1A at $t = \{0, 5, 10, 11, 13, 15, 20, 23, 25\}$ s, $\dot{\epsilon} = 0.097s^{-1}$.

In the realization of ideal steady planar elongation, the perimeter should remain constant and the cross-sectional area must decrease exponentially as $A(t) = A_0 \exp(-\dot{\epsilon}t)$. $A_0 = d_0 L_0$ is the initial cross-sectional area, $\dot{\epsilon}$ the constant strain rate, and t the time. An evaluation of the actual decrease in the cross-sectional area is based on digital imaging. Here, particles placed on the sample surface are traced over time, and from this, it is possible to determine the local Hencky strain $\ln(l(t)/l_0)$, where l_0 is the initial distance in the axial direction between two particles and $l(t)$ is the axial distance at time t . Figure 3.3 shows a series of digital images from an extensional measurement. In addition, the mid-plane outer diameter, $D(t)$, will also be measured and compared to theoretical expectations. The aspect ratios, $\Lambda_1 = h_0/d_0$, and $\Lambda_2 = R_0/h_0$, are dimensionless geometrical parameters that will be used as adjustable parameters in the evaluation of the test method.

3.3 Sample Preparation and Characterization

The network samples are prepared by mixing a linear vinyl terminated poly(propylene oxide) (PPO) manufactured by Kaneka Corp., with a silane terminated hydride f -functional polydimethyl siloxane (PDMS) cross-linker with $f > 2$ supplied by Kaneka. The cross-linking reaction is catalyzed with a Pt catalyst. The characterization of the linear polymer as well as the cross-linker is the same as in chapter 2 section 2.2.1, where it is described in details. Here, we will merely list the obtained molecular weight distributions in table 3.1.

Test samples were prepared with different values of the stoichiometric im-

Table 3.1: Molecular weight distributions of the linear PPO, and the PDMS cross-linker respectively. χ_i is the chemical functionality of each component reported by Kaneka Corp. in mmole/g

Polymer	M_n [g/mole]	M_w [g/mole]	PDI	χ_i [mmole/g]
PPO	10492	15122	1.44	0.22
PDMS	1310	1790	1.36	3.4

balance, r , defined below.

$$r = \frac{\text{no. of silane groups}}{\text{no. of vinyl groups}} = \frac{\chi_{PDMS} \cdot \text{Wt}\%_{PDMS}}{\chi_{PPO} \cdot \text{Wt}\%_{PPO}}, \quad (3.1)$$

where χ_i denotes chemical functionalities, which are reported by Kaneka in mmole/g and listed in table 3.1, while Wt% is the weight fraction of each component. To obtain a self-adhesive material, the samples should be soft viscoelastic solids. For this reason, r is chosen to be close to, but larger than, the lower critical degree of cross-linking, r_c . This is defined as the stoichiometry where a critical gel is obtained, i.e., the transition from a liquid to a solid state. Independent studies of this chemical composition of pre-polymer and cross-linker have shown that r_c is equal to 0.46. This was done by constructing a series of networks with different stoichiometric imbalances and measure $\tan \delta$ in small-amplitude oscillatory shear experiments for each r . We characterize the linear viscoelastic spectrum as in chapter 2, where the storage and loss modulus are given by

$$G'(\omega) = C\omega^n \pi / (2\Gamma(n) \sin(n\pi/2)) + G_0 \quad (3.2)$$

$$G''(\omega) = C\omega^n \pi / (2\Gamma(n) \cos(n\pi/2)) \quad (3.3)$$

The linear viscoelastic properties were obtained using small amplitude oscillatory shear measurements on an AR2000 rheometer from TA Instruments. A 25-mm plate-plate geometry was used and G' and G'' were measured at temperatures ranging from 5°C to 100°C. The data were converted to 25°C using time-temperature super positioning (TTS). The horizontal shift factor a_T was determined by manually shifting data-sets to 25°C, hereafter it was found to follow the form of the Arrhenius equation (equation 3.4), where $\Delta \bar{H}$ is the activation energy for flow and R is the ideal gas constant. T and T_{ref} are the temperature and reference temperature in Kelvin respectively ($T_{\text{ref}} = 298$ K). The values for a_T at the six temperatures used are listed in table 3.2, and from these values, $-\Delta \bar{H}/R$ was found to be 5448 K. The vertical shift factor, b_T , is given by equation 3.5.

$$a_T = \exp \left[-\frac{\Delta \bar{H}}{R} \left(\frac{1}{T} - \frac{1}{T_{\text{ref}}} \right) \right] \quad (3.4)$$

$$b_T = \frac{T_{\text{ref}}}{T} \quad (3.5)$$

Table 3.2: Horizontal shift factor, a_T

T [°C]	5	15	25	50	75	100
a_T	3.7	2	1	0.25	0.1	0.04

Two samples with different values of r were prepared for this study. The experimental results for G' and G'' are shown in figures 3.4 and 3.5, together with the best fit of equations 3.3 and 3.2. The parameters G_0 , C , n and r for both samples are listed in table 3.3. Sample A have more dangling and soluble substructures compared to sample B, which makes sample A more sticky than sample B. A more detailed analysis of n , C , and G_0 can be found in chapter 2.

The value of G_0 is very low compared to the plateau modulus of the pure pre-polymer, G_N^0 , which Fetters *et al.* [1] have reported to be 700 kPa for PPO. We would expect $G'(\omega)$ to approach this value for much longer frequencies than investigated here. This agrees with the results of [22] who studied the influence of pendant chains on the viscoelastic properties.

Also listed in table 3.3 is the characteristic time, τ . It is a measure for the time scale where the material behavior changes from a time-independent response to a more dynamic response. Obviously, this time scale increases as the cross-link density decreases, i.e., when r decreases.

Table 3.3: Characteristic parameters for sample A and sample B at 25 °C.

	sample A	sample B
r	0.57	0.60
G_0 [Pa]	2500 ± 60	5840 ± 80
C [Pa·s n]	1800 ± 60	3840 ± 50
n	0.484 ± 0.007	0.435 ± 0.002
$\tau = (C/G_0)^{1/n}$ [s]	0.5072 ± 0.0007	0.3814 ± 0.0002
w_{ss}	0.57	0.36

The weight fraction of soluble structures, w_{ss} , also listed in table 3.3, is obtained from swelling experiments. The PPO networks are swelled and washed in heptane and the swelled samples are dried until constant weight.

3.4 Nonlinear Properties

The tendency for the cylindrical probe to deform in ideal planar extension depends critically on the nonlinear elastic properties of the network. To describe these properties, we use a combination of elastic and viscoelastic models described in the framework of the K-BKZ constitutive equation [64, 65]. This may be written as an integral over the linear viscoelastic memory function, and

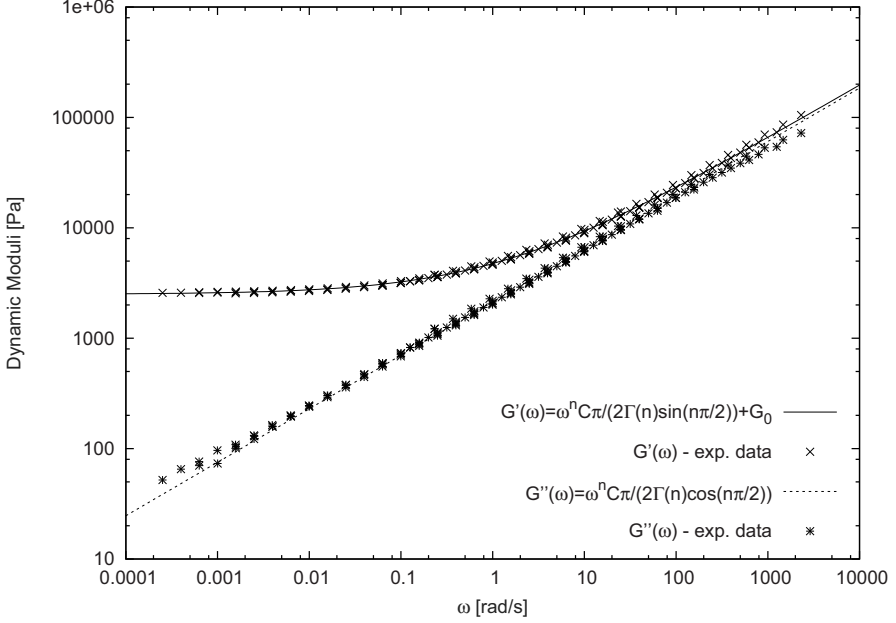


Figure 3.4: DMA spectra of the dynamic moduli of sample A at 25°C. The parameters G_0 , C and n are determined with a least square fit of the expression for $G'(\omega)$ to the measured data. $G_0 = 2500 \pm 60$ Pa, $C = 1800 \pm 60$ Pa s n and $n = 0.484 \pm 0.007$. The stoichiometric ratio, r , is equal to 0.57

a combination of nonlinear strain tensors,

$$\boldsymbol{\sigma} = - \int_{-\infty}^t M(t-t') \left(\frac{\partial V}{\partial I_1} \boldsymbol{\gamma}_{[0]} + \frac{\partial V}{\partial I_2} \boldsymbol{\gamma}_{[0]}^{[0]} \right)_{t,t'} dt' \quad (3.6)$$

$$= - \int_{-\infty}^t M(t-t') \left(\phi_1 \boldsymbol{\gamma}_{[0]} + \phi_2 \boldsymbol{\gamma}_{[0]}^{[0]} \right)_{t,t'} dt'. \quad (3.7)$$

Here, $V(I_1, I_2)$ is a potential function depending on the first, I_1 , and the second invariants, I_2 , of the Finger strain tensor, \mathbf{B} . The functions ϕ_1 and ϕ_2 designate the partial derivatives. The relative strain tensors $\boldsymbol{\gamma}_{[0]}(\mathbf{x}, t, t')$ and $\boldsymbol{\gamma}_{[0]}^{[0]}(\mathbf{x}, t, t')$, as well as the Finger strain tensor, $\mathbf{B}(\mathbf{x}, t, t')$ are given as

$$\boldsymbol{\gamma}_{[0]} = \boldsymbol{\delta} - \mathbf{B}, \quad \boldsymbol{\gamma}_{[0]}^{[0]} = \mathbf{B}^2 - I_1 \mathbf{B} + (I_2 - 1) \boldsymbol{\delta} \quad \text{and} \quad \mathbf{B} = \mathbf{E} \cdot \mathbf{E}^\dagger \quad (3.8)$$

respectively. The subscripts t, t' in equations 3.6 and 3.7 signify that the preceding combination of strain tensors relate to the strain from t' to t . The particle dependence of the strain tensors is omitted for brevity. In Cartesian coordinates, the components of the displacement gradient tensor \mathbf{E} are given

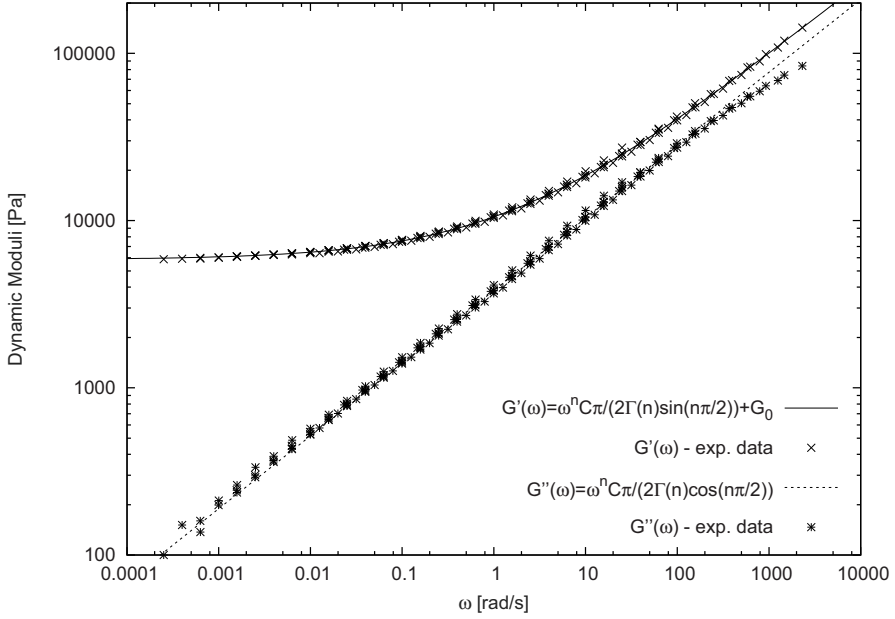


Figure 3.5: DMA spectra of the dynamic moduli of sample B at 25°C. $G_0 = 5840 \pm 80$ Pa, $C = 3840 \pm 50$ Pa sⁿ and $n = 0.435 \pm 0.002$. The stoichiometric ratio, r , is equal to 0.60

as $E_{ij}(\mathbf{x}, t, t') = \partial x_i / \partial x'_j$, $i=1,2,3$, and $j=1,2,3$. This definition is based on a Lagrangian kinematics description, where (x_1, x_2, x_3) and (x'_1, x'_2, x'_3) are positions of the same particle at time t and t' , respectively. The memory function $M(t-t')$ is related to the relaxation modulus as $M(t-t') = dG(t-t')/dt'$. We follow the notation of Bird *et al.* [37] with the exception that our stress tensor $\boldsymbol{\sigma}$ is the negative of their stress tensor $\boldsymbol{\tau}$. Here, we use the memory function,

$$M(s) = C n s^{-(1+n)} + G_0 \delta(t-s), \quad (3.9)$$

$\delta(\dots)$ is the delta function, and $C > 0$ and $0 < n < 1$ are constants obtained from the modified gel equations 3.3 and 3.2 (table 3.3). The part involving the delta function describes an elastic material, while the gel-part becomes a viscoelastic material.

$$\begin{aligned} \boldsymbol{\sigma} = & -Cn \int_{-\infty}^t (t-t')^{-(1+n)} \left(\phi_1 \boldsymbol{\gamma}_{[0]} + \phi_2 \boldsymbol{\gamma}_{[0]} \right)_{t,t'} dt' \\ & -G_0 \left(\phi_1 \boldsymbol{\gamma}_{[0]} + \phi_2 \boldsymbol{\gamma}_{[0]} \right)_{t,0}. \end{aligned} \quad (3.10)$$

We use two specific choices for the nonlinear strain behavior, the classical neo-Hookean model derived for a permanently cross-linked network with affine deformation of the cross-links and the molecular stress function (MSF) model

Table 3.4: Expressions for ϕ_1 and ϕ_2 for neo-Hookean strain measure and tube strain measure without instantaneous chain retraction. The Currie approximation is used for the tube model.

	ϕ_1	ϕ_2
neo-Hookean	1	0
MSF model	$\frac{5}{7}$	$\frac{5}{7\sqrt{I_2 + \frac{13}{4}}}$

[66] for tube networks without chain retraction in an entanglement network. The latter model corresponds to the Doi-Edwards melt model in the Currie form [67] but multiplied by $I_1 + 2(I_2 + (13/4))^{-1/2}$ to account for molecular stretching. The corresponding expressions for ϕ_1 and ϕ_2 are shown in table 3.4. Other models for permanently cross-linked networks include the slip-link [68] and the phonon fluctuation [69] model. In a recent analysis [70], these models have been shown to give a very accurate description of the deviation from neo-Hookean behavior for a near stoichiometric poly-dimethyl-siloxane network.

Before proceeding to detailed finite element simulations of the planar extensional process, we illustrate in an approximate way the influence of the relative magnitude of ϕ_1 and ϕ_2 on the deformation of the sample. If we approximate the extended cylindrical sample by thin membrane theory we find the following equation of equilibrium [71]

$$\kappa_z t_z + \kappa_\theta t_\theta - \Delta p = 0. \quad (3.11)$$

Here, κ_z and κ_θ are the principal curvatures in the axial and circumferential directions, respectively. Also, Δp is the trans-membrane pressure, t_z is the axial traction (force per unit length in circumferential direction), and t_θ the circumferential traction. Exact expressions for the curvatures are given in [71]². In the present situation, $\Delta p = 0$. Provided the deformation from the cylindrical shape of radius R_0 is small, the circumferential curvature is approximately $\kappa_\theta = -1/R_0$. Hence, if we denote the radius of curvature in the axial direction by R_z , it follows that

$$\frac{R_0}{R_z} = \frac{t_\theta}{t_z} = \frac{\sigma_{\theta\theta} - \sigma_{rr}}{\sigma_{zz} - \sigma_{rr}}. \quad (3.12)$$

To illustrate the relative influence of ϕ_1 and ϕ_2 , we assume that the stress is given by the elastic part alone (*i.e.*, that $C = 0$). Let the overall stretch ratio be λ . The respective material stretch ratios in planar extension are then $\lambda_z = \lambda$, $\lambda_\theta = 1$ and $\lambda_r = \lambda^{-1}$. This gives the simple estimate

$$\frac{R_0}{R_z} = \frac{\phi_1(1 - e^{-2\epsilon_N}) + \phi_2(e^{2\epsilon_N} - 1)}{(\phi_1 + \phi_2)(e^{2\epsilon_N} + e^{-2\epsilon_N})}. \quad (3.13)$$

Analogously, the deformation on the cylindrical probe can be approximated in terms of R_z and R_0

$$\frac{D_0 - D(t)}{D_0} = \frac{R_z - R_z \sqrt{1 - (h(t)/(2R_z))^2}}{R_0}. \quad (3.14)$$

²The τ_{ij} in reference [71] are the negative of σ_{ij} here.

This approximation is visualized in figure 3.6, where we show the deformation on the cylinder, and define it as $s = R_0 - R(t)$. $h(t)$ in equation 3.14 is the height of the sample during extension. Assuming that $R_z \gg h(t)$ we can derive the following estimate

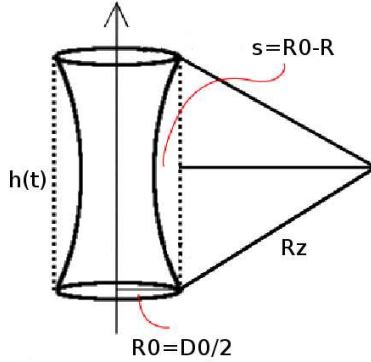


Figure 3.6: Illustration of the deformation on the cylindrical probe.

$$\frac{D_0 - D(t)}{D_0} = \frac{1}{8} \left(\frac{h_0}{R_0} \right)^2 \frac{(e^{2\epsilon_N} - 1)(\phi_1 + \phi_2 e^{2\epsilon_N})}{(\phi_1 + \phi_2)(e^{2\epsilon_N} - e^{-2\epsilon_N})}, \quad (3.15)$$

with h_0 as the initial sample height. Equation 3.15 shows that neo-Hookean materials ($\phi_2 = 0$) will show very little deformation of the cylindrical probe, especially if $R_0 \gg h_0$ since $(D_0 - D(t))/D_0 \rightarrow (h_0/R_0)^2/8$ for $e^{2\epsilon_N} \rightarrow \infty$, but the deformation is highly sensitive to positive values of ϕ_2 . In fact, for $\lambda \gg 1$ the estimate become $(D_0 - D(t))/D_0 \sim e^{2\epsilon_N} = \lambda^2$ for the tube model. Since the plate separation grows with λ , this simple estimate suggests that materials described by the neo-Hookean model will show negligible deviation from the axial cylindrical shape (the radius of curvature in the axial direction is much larger than the plate separation), while materials described by the tube model will show substantial deviation from the cylindrical shape (the radius of curvature in the axial direction is comparable to the plate separation). It also suggests that the aspect ratio $\Lambda_2 = R_0/h_0$ should be large to prevent significant cylindrical deformation.

3.5 Numerical modeling

To study the deformation of the cylindrical probe quantitatively, we perform a finite element simulation of the stretching process without the thin membrane assumption. We use the non-dimensional variables $\mathbf{x}^* = \mathbf{x}/R_0$, $t^* = t \cdot \dot{\epsilon}$,

$\sigma^* = \sigma/G_0$, and $p^* = p/G_0$, where p is the pressure. The mass conservation equation is without dimensions [72], while the dimensionless equation of motion is given by:

$$\nabla^* \cdot \sigma^* + \nabla^* p^* = 0, \quad (3.16)$$

where

$$\begin{aligned} \sigma^*(t^*) &= -n\text{De}^n \int_{-\infty}^{t^*} (t^* - t'^*)^{-(1+n)} \left(\phi_1 \gamma_{[0]} + \phi_2 \gamma^{[0]} \right)_{t^*, t'^*} dt'^* \\ &\quad - \left(\phi_1 \gamma_{[0]} + \phi_2 \gamma^{[0]} \right)_{t^*, 0}. \end{aligned} \quad (3.17)$$

The Deborah number, De , is given by $\dot{\epsilon} \cdot \tau$ where τ is the viscoelastic time scale relative to the elasticity listed in table 3.3. Note that the Deborah number operates on the viscoelastic part only. Thus, the Deborah number describes departure from a purely elastic behavior. This is different from the role of the Deborah number for the original Lodge and MSF models. Hence, we describe them as the modified Lodge and modified MSF models, respectively, the modification being the addition of a purely elastic contribution and the application of the Winter Chambon modulus.

The adopted numerical method, allowing deformation calculations with the described integral constitutive equation, is the time-dependent finite element method developed by Rasmussen [73–75] and Marín *et al.* [76]. Details about the performance and accuracy of the method can be found in these references. The numerical method is a finite element method based on a Lagrangian kinematics description, and therefore, time dependent. The geometry and mesh will be a two-dimensional cylindrical coordinate system, (r, z) , although the finite element mesh is essentially three-dimensional (see reference [73] for more details). We perform extension simulations similar to the planar extension studies presented in the following section. The initial shape of the test specimen is an annulus with inner radius R_0 , outer radius $R_0 + d_0$ and length L_0 . Furthermore rotational symmetry is assumed as well as symmetry in the mid-sample. Moreover, the boundary conditions used in the simulations on the inner surface are stick conditions on the fixture and no stress on the free surface. The simulations are all performed at creeping flow conditions with surface tension and gravity being neglected.

There are several ways of performing the extension simulations. Here, the nodes sticking to the fixture are moved in the z -direction as $(r, z) = (r_0, z_0 \exp(\dot{\epsilon} \cdot t))$, where (r_0, z_0) is the initial position of a node. Figure 3.7 shows an example of an initial axis-symmetric finite element mesh, as well as a mesh extended to a Hencky strain of 2. Since the finite element mesh becomes distorted during extension, re-meshing has been applied when needed.

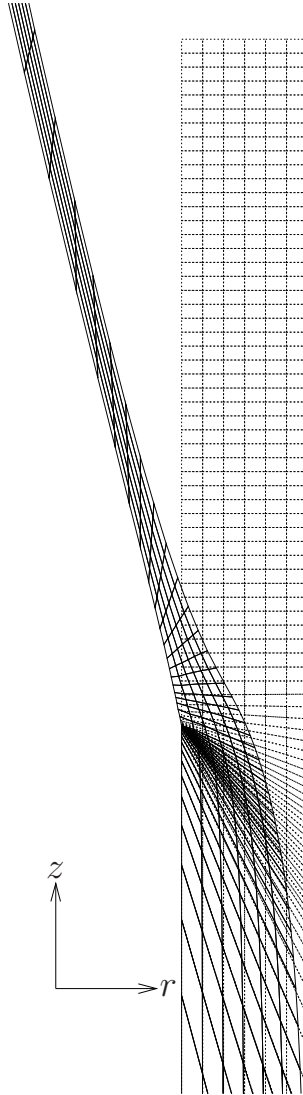


Figure 3.7: Axis-symmetric finite element mesh obtained with the modified MSF model. The dashed lines are the initial mesh. The solid lines are the mesh extended to a nominal Hencky strain of 2. Re-meshing has been applied in between these meshes.

3.6 Results and Discussion

The influence of Λ_1 and Λ_2 will be studied in several experiments with the Planar Elongation Fixture (PEF). The test conditions are listed in tables 3.5 and 3.6 for sample A and B respectively.

Table 3.5: PEF test conditions for sample A. $\Lambda_1 = h_0/d_0$, $\Lambda_2 = R_0/h_0$. The Hencky strain rate is in all cases equal to 0.097 s^{-1}

	TEST 1A	TEST 2A	TEST 3A
$d_0 [\mu\text{m}]$	~ 200	~ 850	~ 850
$h_0 [\mu\text{m}]$	5450	5450	10450
Λ_1	24.8	6.41	12.7
Λ_2	3.7	3.7	1.9

 Table 3.6: PEF test conditions for sample B. $\Lambda_1 = h_0/d_0$, $\Lambda_2 = R_0/h_0$. The Hencky strain rate is in all cases equal to 0.1 s^{-1}

	TEST 1B	TEST 2B	TEST 3B	TEST 4B
$d_0 [\mu\text{m}]$	~ 1000	~ 1000	~ 200	~ 200
$h_0 [\mu\text{m}]$	5450	10450	5450	10450
Λ_1	4.81	9.25	26.8	53.6
Λ_2	3.7	1.9	3.7	1.9

3.6.1 Diameter Measurements

We will assume ideal elongational flow in the symmetry mid-plane as well as isotropic deformation and incompressibility. The three material stretch ratios are given by:

$$\lambda_r = \frac{d(t)}{d_0} \quad , \quad \lambda_\theta = \frac{D(t)}{D_0} \quad \text{and} \quad \lambda_z = \frac{l_z(t)}{l_{z0}}. \quad (3.18)$$

$\lambda_r \cdot \lambda_\theta \cdot \lambda_z = 1$ due to incompressibility. The corresponding Hencky strains are defined as

$$\epsilon_r = \ln(\lambda_r) \quad , \quad \epsilon_\theta = \ln(\lambda_\theta) \quad \text{and} \quad \epsilon_z = \ln(\lambda_z), \quad (3.19)$$

where $\epsilon_r + \epsilon_\theta + \epsilon_z = 0$. The definition of planar elongation is that the sample will only deform in two directions, hence $\lambda_\theta = 1$ or $\epsilon_\theta = 0$. For later validation of the PEF method it is convenient to use an approximation of ϵ_θ as $\epsilon_\theta = \ln(\lambda_\theta) \approx \lambda_\theta - 1$ for ϵ_θ in the vicinity of 0. Hence,

$$\epsilon_\theta \approx \frac{D(t)}{D_0} - 1 = \frac{D(t) - D_0}{D_0}. \quad (3.20)$$

This serves as a rough approximation for the deviation from ideal planar extension in terms of Hencky strain units.

In figure 3.3 a series of digital images from test 1A are shown. The images are recorded each second from $t = 0 \text{ s}$ to $t = 25 \text{ s}$ (only nine are shown here).

From the digital imaging the outer mid-plane diameter, $D(t)$, was measured and the results from all the experiments listed in tables 3.5 and 3.6 are shown in figure 3.8. Here $(D_0 - D(t))/D_0 \approx -\epsilon_\theta$ is shown versus the nominal Hencky strain, ϵ_N , which is the imposed strain

$$\epsilon_N = \ln(h(t)/h_0), \quad (3.21)$$

with $h(t)$ as the distance between the upper and lower contact perimeter and h_0 as the initial distance. If the deformation is ideal ϵ_N is equal to ϵ_z defined in equation 3.19.

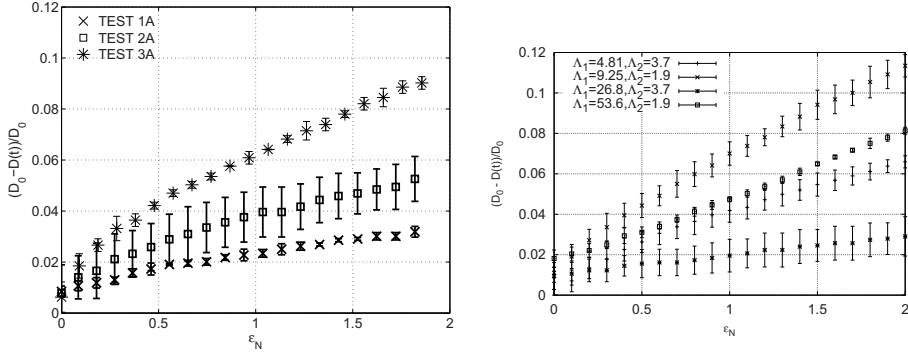


Figure 3.8: $(D_0 - D(t))/D_0 = -\epsilon_\theta$ vs. the nominal Hencky strain, $\epsilon_N = \ln h(t)/h_0$. For details about the test conditions the reader is referred to tables 3.5 and 3.6

It is seen that $(D_0 - D(t))/D_0$ is non-zero in all the experiments. By comparing the results of tests 2B and 4B, it is obvious that $|\epsilon_\theta|$ is reduced by increasing Λ_1 . The same trend is observed when comparing test 1B to test 3B and test 1A to test 2A. However, it is also seen that it is not necessarily the highest value of Λ_1 that gives the lowest $|\epsilon_\theta|$. Tests 1B and 3B, which have the lowest absolute value of ϵ_θ , have higher values of Λ_2 than tests 2B and 4B. This shows that one should aim for $\Lambda_1 > 10$ and $\Lambda_2 > 3$ to obtain planar extension for the two test materials. Test 1A and test 3B seem to give the best results of all the experiments. A comparison between $|\epsilon_\theta|$ and ϵ_N in test 1A and 3B shows that $|\epsilon_\theta|$ is only about 1.5% of ϵ_N and is therefore assumed to be negligible.

3.6.2 Particle Tracking

Particle tracking is used to determine the local Hencky strain on the sample surface. This is to compare the true Hencky strain, ϵ_z , defined in equation 3.19, and ϵ_N . If the deformation is not ideal at the mid-plane, the true Hencky strain based on particle tracking will deviate from the nominal Hencky strain. 3×2 particles are placed on the surface facing the camera, and the distance, $l(t)$, between each particle pair is determined. $\langle \epsilon_z \rangle = \ln \langle l_z(t)/l_{z0} \rangle$, is calculated ($\langle \dots \rangle$ denotes sample averages). A comparison of ϵ_z to ϵ_N is shown in figure 3.9, and it is seen that the slope is 1, corresponding to ideal elongation, within the error bars. The error-bars are calculated from the variance: $\text{Var}(l_z(t)/l_{z0}) = \langle l_z(t)/l_{z0} - \langle l_z(t)/l_{z0} \rangle^2 \rangle$.

Figure 3.10 shows the particle tracking results from tests 2 and 3A. It is seen that the more Λ_1 drops the more the results will deviate from the ideal deformation with a slope of 1. The same trend is observed for sample B in figures 3.11 and 3.12. Hence, the local strain on the sample surface is highly

sensitive towards Λ_1 , and ideal planar deformation can only be obtained for $\Lambda_1 > 10$.

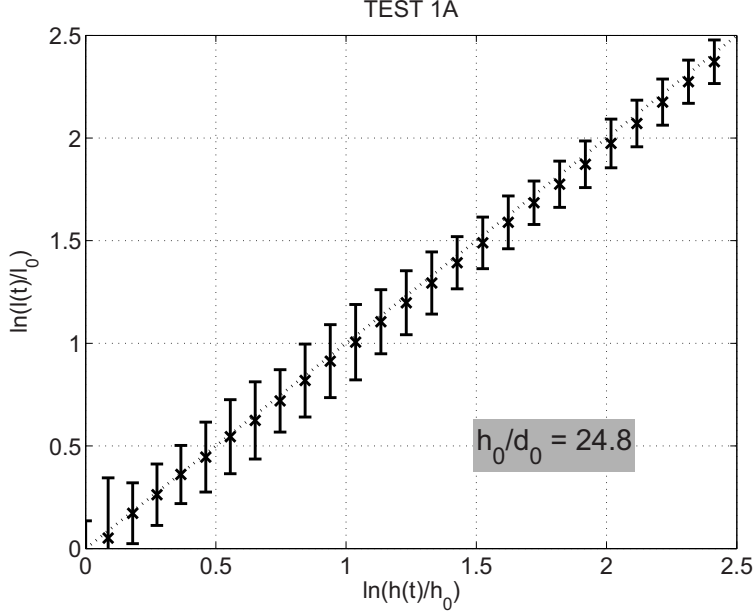


Figure 3.9: The true Hencky strain $\ln\langle l(t)/l_0 \rangle$ vs. the nominal strain, $\epsilon_N = \ln(h(t)/h_0)$. The data corresponds to the series given in figure 3.3 and the test conditions for test 1A (see table 3.5). The aspect ratio Λ_1 is equal to 24.8

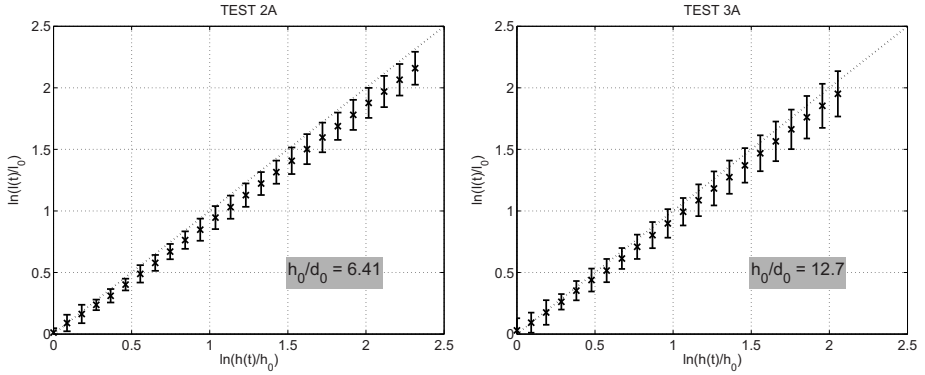


Figure 3.10: True Hencky strain vs. nominal strain. $\Lambda_1 = 6.41$ and 12.7 for test 2A and 3A.

To perform ideal particle tracking, two particles should be placed above and below the mid plane of the sample, and the distance between them should be considerably smaller than h_0 and, ideally, the particles should be infinitely small

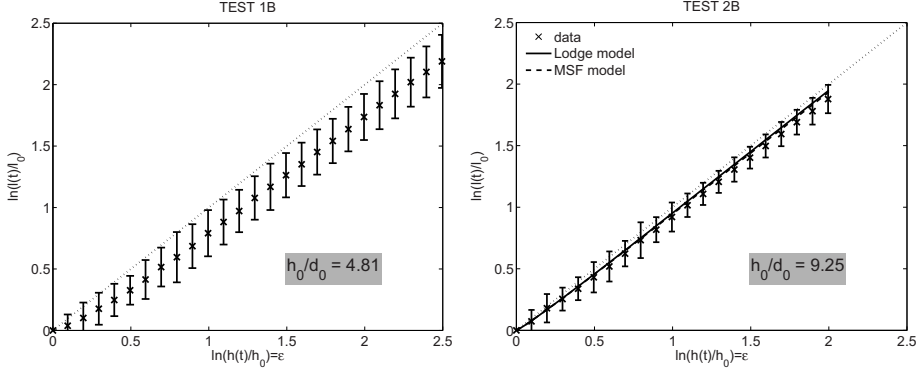


Figure 3.11: $\Lambda_1 = 4.81$ and 9.25 for test 1B and 2B. In test 2B the full and dashed lines are the modified Lodge and MSF model predictions from numerical simulations.

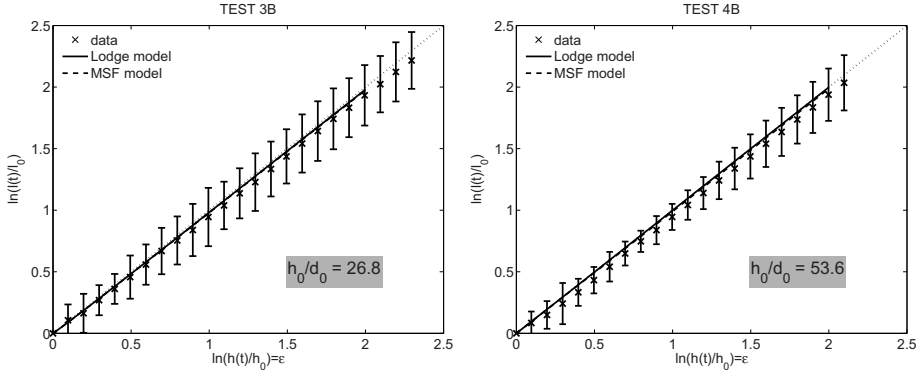


Figure 3.12: $\Lambda_1 = 26.8$ and 53.6 for test 3B and 4B. The full and dashed lines are the modified Lodge and MSF model predictions from numerical simulations.

since they are considered as discrete points. Real particle tracking may deviate somewhat from this, and it is important to test whether this has an influence on the results. Finite-element simulations corresponding to tests 2–4B have therefore been made, and the results for ϵ_z are shown in figures 3.11 and 3.12 together with the experimental results. The dashed lines represent the modified MSF model predictions and the full lines the modified Lodge predictions. It is seen that there is a very good agreement with the numerical predictions and the experimental particle tracking data, which confirms that the data are indeed reliable. These results furthermore state that $\epsilon_z = \epsilon_N$.

3.6.3 Numerical Results

The numerical results for $-\epsilon_\theta$ are shown in figure 3.13 together with the corresponding experimental data from figure 3.8. It is seen that the simulations

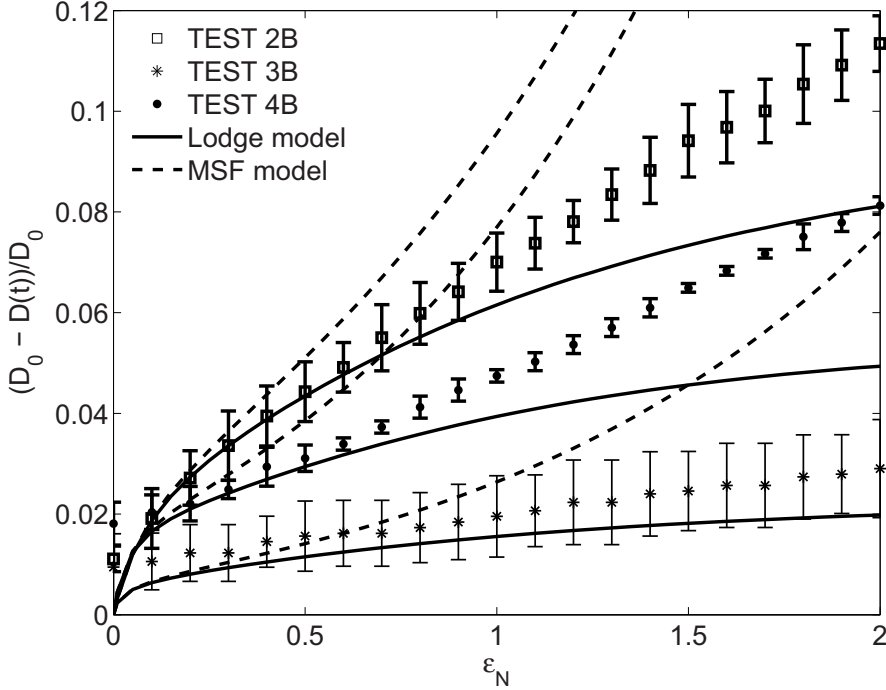


Figure 3.13: $(D_0 - D(t))/D_0$ vs ϵ_N for TEST 2B, 3B and 4B. The dashed lines represent the numerical prediction based on the modified MSF model, while the full lines represent the numerical prediction based on the modified Lodge model

represent the data well up to a Hencky strain of about 0.5, especially those of the modified Lodge model. At higher Hencky strains, the modified MSF model overestimates $-\epsilon_\theta$ to a large extent, while the modified Lodge model gives a slight underestimation. However, the modified Lodge model seems to capture the trend of the experimental data well, since it levels off to a plateau as the experimental data, and it furthermore captures the order of magnitude of $-\epsilon_\theta$. These results confirm the analysis made in section 3.4 based on equation 3.15, which states that materials described by neo-Hookean-type models show little deformation on the cylindrical probe opposite to tube models. Moreover, the results indicate that the non-linear properties of these materials are well described by the classical neo-Hookean behavior. The numerical results indicate that, while the simple estimate in equation 3.15 correctly predicts the general influence of Λ_2 and the deviation from neo-Hookean behavior it does underpredict the deviation by a factor of 2.

In addition to a judicious choice of aspect ratios, the near ideal planar extension obtained is also tied to the somewhat unexpected fact that the non-linear behavior of the networks is almost neo-Hookean. The fact that the simulations for the modified MSF model show much larger deviation from ideal planar ex-

tension may indicate that the PEF without pressure compensation may be less applicable for polymer melts described by the modified MSF model [77].

3.6.4 Measured Stresses

While the deformation of the sample from an ideal cylinder depends critically on the deviation from neo-Hookean behavior, the same is not necessarily true for the measured stresses. In fact, provided the deformation is (forced to be) planar extension, the additional term in the Mooney–Rivlin model does not deviate from the neo-Hookean prediction. From measurements of the force, $F(t)$, we calculate the stress difference

$$\sigma_{zz} - \sigma_{xx} = \frac{F(t)}{A(t)}. \quad (3.22)$$

$A(t)$ is the cross-sectional area assumed to decrease exponentially in time: $A(t) = A_0 \exp(-\dot{\epsilon}t)$, A_0 is the initial cross-sectional area.

In figure 3.14, we compare the measured stresses for test 1A and test 3B with the ideal prediction of the modified Lodge model. It is seen that the modified Lodge model predict the linear regime very well, which indicates that the extensional measurements correspond to the LVE measurements. It is furthermore noticed that the model predicts the data beyond the linear regime, even up to a Hencky strain of 2 for sample B. The modified Lodge model does not include finite extensibility and we ascribe this as the reason for the deviation between model and data above 2 Hencky strains.

An estimation for the finite extensibility of the pre-polymer chains can be obtained from the number of Kuhn steps, n_k , in the pre-polymer chain as $\lambda_{\max} = n_k^{1/2}$. The Kuhn length, l_k , is assumed to be similar to that of a PEO chain [78]; hence, $l_k = 11 \text{ \AA}$. $\langle R_0^2 \rangle = 6285 \text{ \AA}^2$ is obtained from Fetters *et al.* [1]. Hence, $n_k = \langle R_0^2 \rangle / l_k^2 \simeq 52$, and thus, λ_{\max} to 7.2. This corresponds to approximately 2 Hencky strain ($\ln(\lambda_{\max})$), which confirms the above statement.

It is observed that the stress differences are time-dependent, i.e. the strain rate matters. As the Deborah number goes toward zero the material behavior is well described by the classical neo-Hookean or Mooney–Rivlin, solid, while for increasing Deborah numbers, the stress difference increases. The time-dependency is more pronounced at small Hencky strains, while the curves seem to collide at large Hencky strains. The reason for this is that the dangling and soluble structures, which have time dependent dynamics, will have a dominating effect at small Hencky strains, while the elastically active network, which is time-independent, will be dominating at large deformations. The dashed line in figure 3.14 represents the classical neo-Hookean or Mooney–Rivlin prediction. A very interesting observation is that the modified Lodge model captures the time-dependencies of the material responses at low to intermediate Deborah numbers (*i.e.*, for $De < 1$).

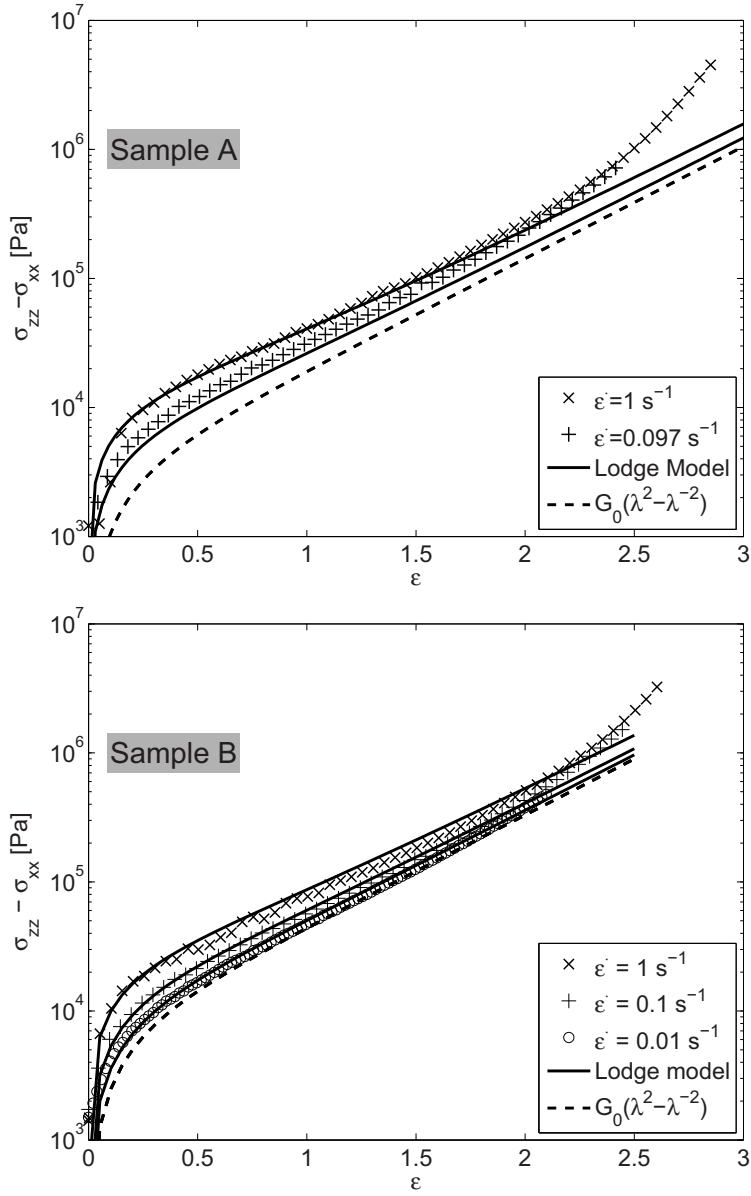


Figure 3.14: The measured stress difference, $\sigma_{zz} - \sigma_{xx}$, vs. the Hencky strain, $\epsilon = \epsilon_z$. The full lines are the ideal predictions of the modified Lodge model. The dashed lines are the classical predictions, where $\lambda = \lambda_z$

3.7 Conclusion

A new test method for planar elongation has been developed for soft polymer networks with application towards pressure-sensitive adhesives. It was proven that planar extension is obtained by measuring the change in the mid-plane diameter during extension and, from that, calculate $-\epsilon_\theta$ given by equation 3.20. It was shown that, by adjusting the aspect ratios $\Lambda_1 > 10$ and $\Lambda_2 > 3$, it was possible to keep $|\epsilon_\theta|$ below 0.04 even when $\epsilon_z = 2$. Additionally, particle tracking results showed that the local strain rate on the sample surface was equal to the nominal strain rate, however, only when $\Lambda_1 > 10$.

It was furthermore shown that the material behavior at low to intermediate Deborah numbers show small deviations from the classical neo-Hookean behavior, and that the near ideal planar extension is a result of the neo-Hookean behavior.

Chapter 4

Reversible Planar Elongation of Soft Polymeric Networks

The newly developed planar elongation fixture, designed as an add-on to the filament stretch rheometer, is used to measure reversible large amplitude planar elongation on soft elastomers. The concept of this new fixture is to elongate an annulus, by keeping the perimeter constant. The deformation on the cylindrical probe is measured using digital imaging, and it is found that the diameter drops a few percent only compared to the initial diameter. Additionally it is found that a new approximation to the Doi-Edwards (DE) model, without independent alignment, captures the experimental data very well. In particular it is observed that this new approximation reproduces the order of magnitude of the deformation on the cylindrical probe, and by that we confirm our previous statement; that the deformation on the cylindrical probe is highly sensitive towards the choice of strain tensor.

When analyzing the measured stress data, it is observed that there is some elastic recovery when reversing the flow. This is analyzed calculating the amount of work needed during the deformation, and it is observed that the sample itself contributes with work upon flow reversal.

The stress is well described by both the modified Lodge model and the new approximation to the DE model, which leads to the conclusion that the stress is time-strain separable. This demonstrates that the energy loss is due to linear viscoelastic relaxation, and can be determined solely from linear viscoelastic measurements.

4.1 Introduction

When tuning the elastic properties of polymeric networks, it is common to consider the applied stoichiometry [46]. By using an imbalanced stoichiometry it is possible to introduce dangling and soluble structures, *i.e.*, structures that are not elastically active. Imbalanced networks can possess both purely elastic as well as viscoelastic behavior, where the dominating behavior depends on the applied time scale; at short times we observe a behavior that resembles that of a polymer melt, while at long time scales we see that of a rubber.

In this work we would like to elaborate more on the elastic character of polymer networks, when exposed to large deformations. A unique way of doing so is to measure large amplitude oscillatory elongation (LAOE), as introduced by Nielsen *et al.* [79] by using the filament stretch rheometer (FSR), and further developed by Bejenariu *et al.* [55] to polymeric networks. Such experiments give information about the elastic recovery in a loading and unloading cycle, and the entropic state of the material, as it mounts the work performed by the polymer. In the work done by Bejenariu *et al.* [55] the extension is defined as

$$\epsilon(t) = \Lambda/2[1 - \cos(\Omega t)], \quad (4.1)$$

where $\Omega = 2\pi/T$ is the angular frequency with period T of the cycle, and Λ is the strain amplitude.

In this work we will introduce a method to measure reversible planar elongation on a FSR. We will use the same approach as Bejenariu *et al.* [55], who measured uniaxial oscillatory flow on the same FSR, using feed back control of the sample diameter (for details about the feed back control on the FSR see Bach *et al.* [51]). We will use the newly developed planar elongation fixture (PEF) to measure reversible planar elongation on soft (sticky) elastomers. It is designed as an add-on to the FSR, and was discussed in chapter 3, to find the optimal test conditions for ideal planar elongation. The PEF cannot use the feed-back control of the strain normal to the stretching direction, but is limited to just measuring the strain development with time. This is, however, not of major concern, since it is found that nearly ideal planar extension can be achieved by adjusting the initial sample geometry as observed in chapter 3.

An illustration of the fixture with a sample is shown in figure 4.1. The concept is to measure planar elongation forces on a tube-like sample, which is shaped by the upper and lower plate of the fixture. The PEF is mounted on the FSR, and the upper plate will be pulled upwards with a strain rate given by $\dot{\epsilon}(t) = d\epsilon(t)/dt$, with the Hencky strain specified in equation 4.1. The key concern is to keep the perimeter constant during deformation. For a more detailed description of the PEF, the reader is referred to chapter 3.

As pointed out by Bejenariu *et al.* [55], thin non-cylindrical samples tend to buckle in reversed deformations. Hence, it is not possible to perform a full cycle, as the measurements become unreliable when the sample buckles. We will thus, perform reversible flow until this point only.

Figure 4.2.A and B shows the relative evolution of the outer diameter versus dimensionless time, $t\nu$. ν is the frequency in units of s^{-1} and is equal to $\Omega/(2\pi)$.

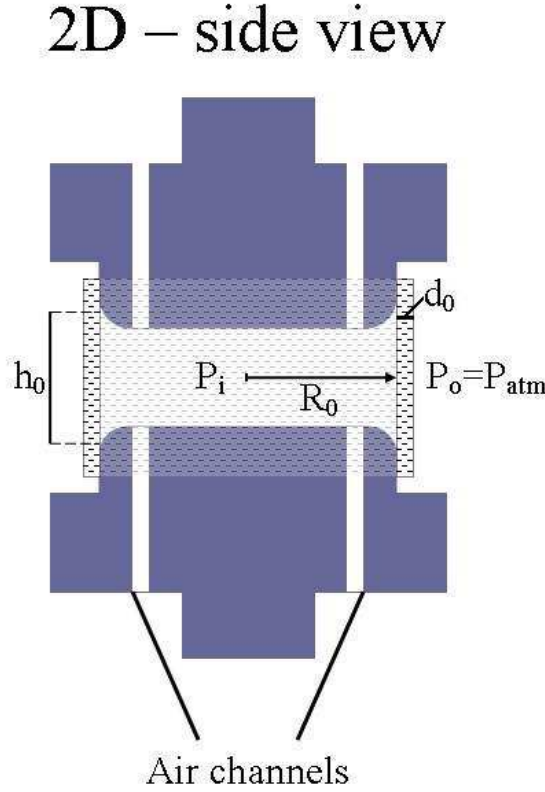


Figure 4.1: Sketch of the add-on fixture. It consist of two disks, an upper and a lower. A thin sample, of an initial thickness, d_0 , is wrapped around the two disks to form a hollow cylinder, with a radius of R_0 . The distance between the upper and lower contact perimeter, between the sample and fixture is h , Where the initial distance is h_0 .

The angular frequency and strain in figure 4.2.A and B are $\Omega = 0.4 \cdot \pi$ rad/s and $\Lambda = 1$ and 2.5, respectively. The relative outer diameter is defined as

$$\frac{D_0 - D(t)}{D_0}, \quad (4.2)$$

where $D_0 = 2(R_0 + d_0)$ is the initial outer diameter, with R_0 as the radius of the fixture (see figure 4.1), and d_0 the initial sample thickness. In Figure 4.2.A and B, it is seen that the relative initial diameter is larger than zero in both cases. The reason for this is that the sample initially bended slightly inwards making $D(t = 0)$ less than D_0 . We will discuss this problem later. The data reaches a maximum while stretching, hereafter they at some point will drop dramatically, and the sample will start to buckle. The overall observation is that the diameter of the cylindrical probe drops a few percent only from its

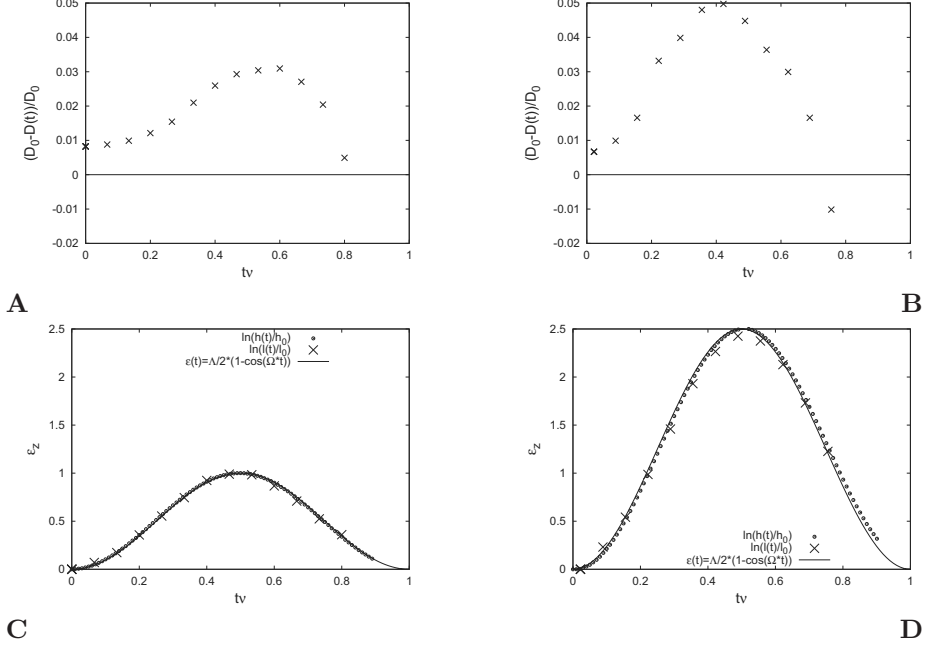


Figure 4.2: The evolution of the relative outer diameter, $(D_0 - D(t))/D_0$ and logarithmic extension vs. time for $\Omega = 0.4 \cdot \pi$ rad/s and (A,C) $\Lambda = 1$ and (B,D) $\Lambda = 2.5$. The full line in (A) and (B) specifies the initial relative diameter, and buckling is assumed to occur when this line is crossed. The full curve in (C) and (D) corresponds to equation 4.1. The dots are the actual logarithmic plate separation (measured by the FSR), while the crosses are the strain validation made with particle tracking. All the results are obtained with sample A, with sample details specified in table 4.1

initial state, which suggests that the deformation is nearly planar. Another more general observation is that, as the Hencky strain rate increases the deformation of the cylindrical probe increases.

In the realization of planar elongation, the perimeter must remain constant, and the cross-sectional area, $A(t)$, must decrease exponentially in time from its initial value, A_0 .

Figure 4.2.C and D shows the expected Hencky strain based on equation 4.1, as well as the strain measured by the FSR, and based on the plate separation, $h(t)$, represented by circles. The crosses are obtained from particle tracking, where the distance between particles placed on the sample surface, are traced over time. The plate separation measured by the instrument, and the particle separation, both follow nicely the theoretical line. We define the Hencky strain based on plate separation as

$$\epsilon(t) = \ln \frac{h(t)}{h_0}, \quad (4.3)$$

with h_0 as the initial sample height.

The Hencky strain based on the particle tracking is given by

$$\epsilon_z(t) = \ln \frac{l(t)}{l_0}, \quad (4.4)$$

where $l(t)$ is the particle distance at time t , and $l_0 = l(t = 0)$. For ideal elongation we require that $\epsilon_N = \epsilon_z$. As this is nearly the case we will in the following denote the Hencky strain as $\epsilon_z(t)$, and we know that

$$A(t) = A_0 \exp(-\epsilon_z(t)). \quad (4.5)$$

Snapshots of the experiment corresponding to the data in figure 4.2.B and D, are shown in figure 4.3. Here, it is possible to follow the evolution of the extension, until the sample buckles. An interesting observation is that after buckling, the sample will *unbuckle* when left at rest for some time, as seen in the last three snapshots.

We calculate the stress difference from the measured force, $F(t)$ as

$$\sigma_{zz} - \sigma_{xx} = \frac{F(t)}{A(t)}, \quad (4.6)$$

and the stress differences at different experimental conditions are shown in figure 4.4. It is seen that the stress does not become negative after reversing the flow, but instead slowly approaches zero. The reason for the non-negative stress, in the reversing flow, is that the samples buckles instead of squeezing. Due to this, it is not possible to determine the recovery strain, ϵ_R , to be the strain where the stress becomes 0 after reversing the flow, as defined by Nielsen *et al.* [54]. We will merely focus on the overall energy loss in the loading and unloading cycle.

4.2 Materials and Methods

4.2.1 Samples

We use the same two sample as in chapter 3, with the characteristic parameters listed here in table 4.1. The parameters, G_0 , S and n , are obtained by fitting the modified gel equation to the linear viscoelastic data

$$G'(\omega) = C\omega^n \pi / (2\Gamma(n) \sin(n\pi/2)) + G_0 \quad (4.7)$$

$$G''(\omega) = C\omega^n \pi / (2\Gamma(n) \cos(n\pi/2)) \quad (4.8)$$

The weight fraction of solubles are obtained from swelling experiments. The stoichiometric imbalance, r , is defined as the ratio of cross-linker reactive sites to polymer reactive sites. The polymer is added in excess to get soft and sticky networks.

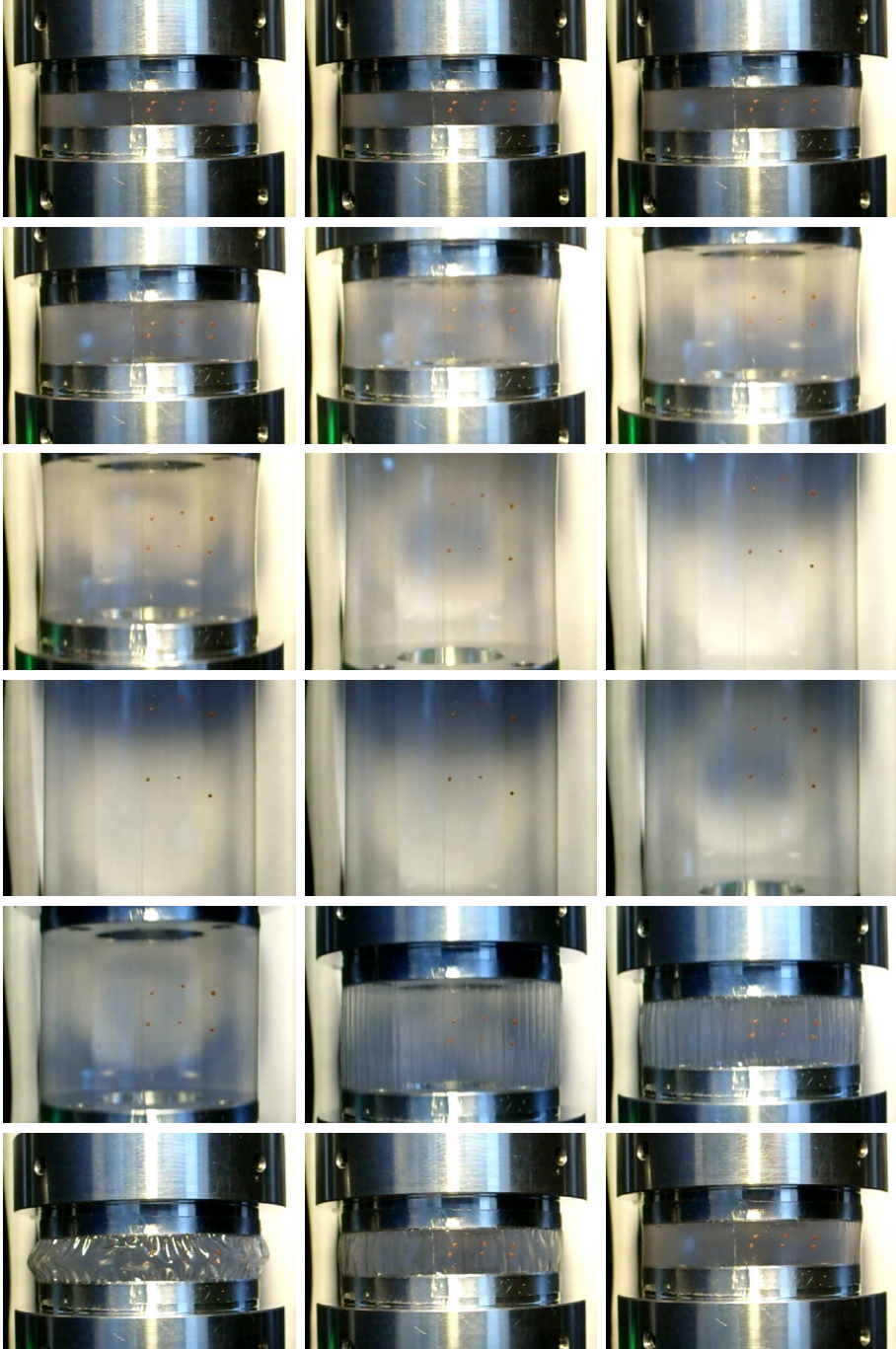


Figure 4.3: Snapshots of the experiment corresponding to the data shown in figure 4.2.B and D, at times $t \cdot \nu = \{0, 0.033, 0.067, 0.1, 0.127, 0.153, 0.2, 0.233, 0.267, 0.3, 0.333, 0.367, 0.433, 0.467, 0.533, 0.667, 1.027\}$

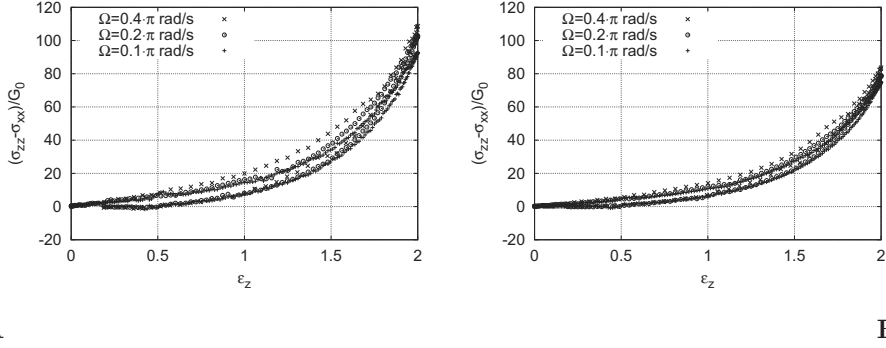


Figure 4.4: Normalized stress difference vs. normalized strain with $\Lambda = 2$, for sample A (A) and sample B (B). Sample details are specified in table 4.1.

Table 4.1: Characteristic parameters for sample A and sample B at 25 °C.

	sample A	sample B
r	0.57	0.60
G_0 [Pa]	2500 ± 60	5840 ± 80
C [Pa·s ^{n}]	1800 ± 60	3840 ± 50
n	0.484 ± 0.007	0.435 ± 0.002
$\tau = (C/G_0)^{1/n}$ [s]	0.5072 ± 0.0007	0.3814 ± 0.0002
w_{SS}	0.57	0.36

4.2.2 Experimental Setup

For the planar elongation experiments we choose the sample dimension for the two samples to be; $d_0 \simeq 200$ [μm], and $h_0 = 5450$ [μm]. This choice is based on the results in chapter 3 where this was found as an optimal choice to achieve nearly ideal planar elongation.

The experimental procedure is identical to the one in chapter 3 where we use particle tracking to validate the strain in the stretching direction, ϵ_z , and digital imaging to measure the sample diameter, $D(t)$. The primary difference from the experiments in chapter 3 is that the Hencky strain rate is a function of time

$$\dot{\epsilon}(t) = \Lambda/2\Omega \sin(\Omega t) \quad (4.9)$$

4.2.3 Nonlinear Analysis

In chapter 3 we found that the amount of bending of the cylindrical probe depends critically on the nonlinear strain behavior of the polymer networks. This conclusion was achieved from finite element model (FEM) simulations with the modified MSF model, and the modified Lodge model¹, both used within

¹Both models are explained in details in chapter 3

the frame-work of the K-BKZ constitutive equation [64, 65]. The MSF model largely overpredicted the deformation of the cylindrical probe, while the Lodge model resulted in a slight underestimation. We will extend this analysis here, by introducing a new nonlinear strain tensor. We use the same K-BKZ constitutive equation and the same memory function as in chapter 3.

$$\boldsymbol{\sigma} = - \int_{-\infty}^t M(t-t') \left(\phi_1 \boldsymbol{\gamma}_{[0]} + \phi_2 \boldsymbol{\gamma}^{[0]} \right)_{t,t'} dt' \quad (4.10)$$

$$M(s) = C n s^{-(1+n)} + G_0 \delta(t-s), \quad (4.11)$$

where ϕ_1 and ϕ_2 are the partial derivatives of the potential function V^2 .

For the nonlinear strain behavior we will use the modified Lodge model ($\phi_1 = 1$ and $\phi_2 = 0$), while we as a second choice, will use a new approximation to the Doi-Edwards (DE) model without independent alignment (IA). This model is derived by Hassager and Hansen [80], and will be described as the DE network model without IA or simply the DE network model. The expressions for ϕ_1 and ϕ_2 are

$$\begin{aligned} \phi_1 &= \frac{15}{16} \left(1 - \frac{3}{2} \frac{I_2^{3/2}}{I_1^3} + \frac{I_2}{I_1^2} \left(\frac{9}{8} - \log I_1 + \frac{1}{2} \log I_2 \right) - \frac{4a_1}{I_1^2} \right) \\ \phi_2 &= \frac{15}{16} \left(\frac{9}{8} \frac{I_2^{1/2}}{I_1^2} + \frac{1}{I_1} \left(-\frac{5}{8} + \log I_1 - \frac{1}{2} \log I_2 \right) - \frac{4a_2}{I_2^2} \right), \end{aligned} \quad (4.12)$$

where the constants a_1 and a_2 are given by

$$\begin{aligned} a_1 &= \frac{1161}{1120} - \frac{3\sqrt{3}}{8} - \frac{3}{8} \log 3 \\ a_2 &= -\frac{909}{1120} + \frac{9\sqrt{3}}{32} + \frac{3}{8} \log 3 \end{aligned} \quad (4.13)$$

This approximation was derived by following the same approach as Currie [67] however, without the IA assumption. It shows 2.3% deviation from the exact expressions in both uni- and biaxial extension and 2.2% on the damping function and 1.8% on the normal stress ratio [80]. In comparison the Currie approximation do not have the correct asymptotic behavior and do thus, have unbounded errors when the strain goes to infinity.

The DE network model includes a non-zero weighting on the lower convected strain tensor. We therefore expect that it will predict a larger cylindrical deformation than the Lodge model in FEM simulations. In ideal planar simulations, *i.e.*, when $\epsilon_\theta = 0$ and $I_1 = I_2$ by definition, it can be shown that the nonlinear strain tensor in the DE network model is approximately equal to the strain tensor in the Lodge model.

²See chapter 5 for description

4.2.4 Numerical Modeling

We use the same finite element approach as in chapter 3, to study the quantitative deformation on the cylindrical probe. It is a FEM based on a Lagrangian kinematics description and is therefore time-dependent.

We use the non-dimensional variables $\mathbf{x}^* = \mathbf{x}/R_0$, $t^* = t \cdot \nu$, $\boldsymbol{\sigma}^* = \boldsymbol{\sigma}/G_0$, and $p^* = p/G_0$, where p is the pressure. The dimensionless equation of motion is given by

$$\nabla^* \cdot \boldsymbol{\sigma}^* + \nabla^* p^* = \mathbf{0}, \quad (4.14)$$

where

$$\begin{aligned} \boldsymbol{\sigma}^*(t^*) = & -n\text{De}^n \int_{-\infty}^{t^*} (t^* - t^{*'})^{-(1+n)} \left(\phi_1 \boldsymbol{\gamma}_{[0]} + \phi_2 \boldsymbol{\gamma}^{[0]} \right)_{t^*, t^{*'}} dt^{*'} \\ & - \left(\phi_1 \boldsymbol{\gamma}_{[0]} + \phi_2 \boldsymbol{\gamma}^{[0]} \right)_{t^*, 0}, \end{aligned} \quad (4.15)$$

Here the Deborah number, De , is given by $\nu\tau$, where τ is the viscoelastic time scale listed in table 4.1. More details about the FEM method are given in chapter 3.

4.3 Results and Discussion

We would like to characterize the nonlinear viscoelastic behavior of the soft networks, and it is therefore important to measure sample stresses at high strain values. However, the maximum strain value must not result in sample rupture in order to perform reversible flow.

In figure 4.4 we show the stress difference obtained for $\Lambda = 2$ at three angular frequencies. The stress is normalized with the equilibrium modulus, G_0 , and plotted versus $\epsilon(t)$. Figure 4.4.A shows results for sample A and figure 4.4.B shows results for sample B. We observe that the stress increases slightly as Ω increases, but more importantly we see strain hardening due to the highly nonlinear deformation. The normalized stress for the softest sample A is higher than for sample B, and the energy loss, defined as the area of the hysteresis cycle, is also larger for sample A. The reason for these observations is that the viscous contribution to stress is higher for sample A, which will result in a higher amount of energy loss. To elaborate more on the elastic versus viscous character of the samples, we will make a numerical analysis based on the constitutive models presented in the previous section.

In all the experiments we observed that $\epsilon_z = \epsilon_N$. We will therefore, in the following, only focus on the strain validation of ϵ_θ . In chapter 3 we derived the following relation between the diameter and the strain normal to the stretching direction

$$\epsilon_\theta \approx \frac{D(t) - D_0}{D_0}. \quad (4.16)$$

4.3.1 Diameter Measurements

To illustrate the fact that the deformation obtained with the PEF is nearly planar, we show the deformation of the cylindrical probe in figure 4.5.A. The experimental data in this figure corresponds to the stress data shown in figure 4.4.B. Before discussing the comparison to FEM predictions, we will point out some limitations observed in the experimental data.

At first we have a start-up problem in the experimental setup. It is observed that the initial data points are not zero. The reason for this is that as the sample is mounted in the FSR, deformation of the sample can easily take place. In the three cases shown in figure 4.5.A this initial deformation decreased the initial outer diameter compared to D_0 . This will however, only have an effect on the initial data points, while it will be negligible as the sample stresses increases. Secondly we must consider the accuracy of the data. To do so we compare the results with those given in figure 4.5.B. The data points in this plot are obtained from steady planar elongation at three different experimental conditions denoted TEST2B, 3B and 4B. Details about these test conditions are listed in table 3.6 in chapter 3. The variance on these data are obtained from triple determination, and they indicate that the scattering on the data lies within ~ 0.02 , *i.e.*, the data are labeled with considerable uncertainties. With an uncertainty of ~ 0.02 on the reversible data in figure 4.5.A, all the data sets can be considered equal within the scattering. The latter corresponds well with the FEM predictions, since both the Lodge model and the DE network model suggests that the bending on the probe is frequency independent. We also observe that the Lodge model underpredicts the data in both reversible and steady elongation. In chapter 3 it was found that the lower convected strain tensor, $\gamma^{[0]}$, should be present in the K-BKZ constitutive equation (see equation 3.7) to increase the cylindrical deformation compared to the Lodge model. This is the case for the DE network model and we see that it captures the order of magnitude of the cylindrical deformation very well in both figure 4.5.A and B.

4.3.2 Measured Stresses

Figure 4.6 shows the stress difference obtained with sample B, with $\Lambda = 2$ and $\Omega = 0.4 \cdot \pi$ rad/s. The red line is a numerical representation of *ideal* large amplitude oscillatory planar elongation using the DE network model. The green line represents the corresponding FEM result, with the same model without oscillations, while the blue line is the FEM result obtained with the Lodge model. We observe that both models captures the stress difference very well. Additionally we see that the numerical FEM simulations replicate the buckling of the sample by slowly approaching a zero stress, but never crossing zero. In the ideal prediction the stress curve tends to shift downwards after the first cycle, and reaches steady state after the second cycle. Hence, some energy is lost in the first cycle and cannot be gained later.

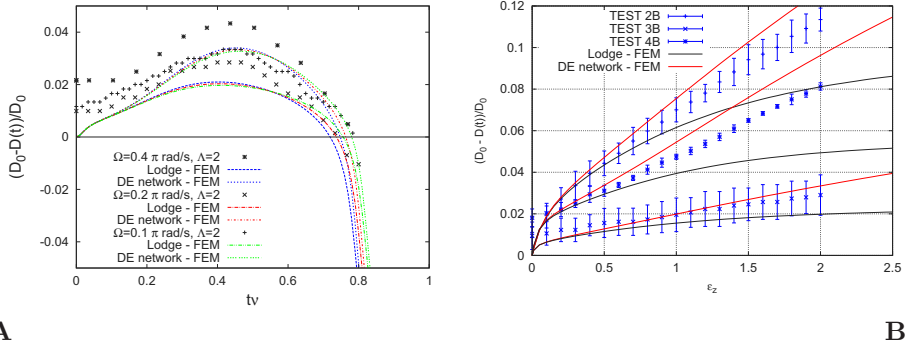


Figure 4.5: (A) Evolution of the relative outer diameter vs. dimensionless time for $\Lambda = 2$ and three different angular frequencies. The dashed lines represent FEM simulations for the Lodge and DE network model. (B) Evolution of the relative outer diameter during steady elongation. The experimental data are the same as those in figure 3.13, the curves are obtained with FEM simulations with DE network model and the Lodge model. All the experimental data are obtained with sample B.

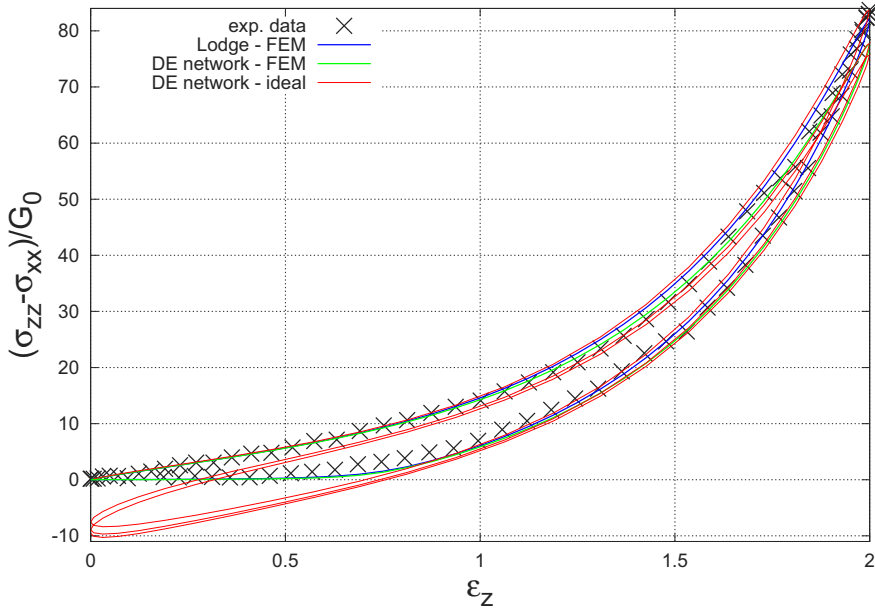


Figure 4.6: Measured stress differences obtained with sample B. $\Lambda = 2$, and $\Omega = 0.4 \cdot \pi \text{ rad/s}$. The blue and green line are the numerical FEM results, obtained with the Lodge and DE network model respectively. The red is ideal numerical planar oscillatory elongation obtained using the DE network model, *i.e.*, $\epsilon_\theta = 0$ and $I_1 = I_2$ by definition.

Elastic Recovery

We can derive the amount of work performed during one cycle. Let the deformation per unit time and the work per unit deformation be given by

$$\frac{dl}{dt} = l\Lambda/2\Omega \sin \Omega t, \quad dw/dl = f, \quad (4.17)$$

where the force, f , is equal to the cross-sectional area times the stress difference. A combination of the expressions above leads to

$$dw = l_0 A_0 (\sigma_{zz} - \sigma_{xx}) \Lambda / 2\Omega \sin \Omega t dt, \quad (4.18)$$

where l_0 and A_0 is the initial sample height and cross-sectional area, respectively. In the above derivation we have assumed that the material is incompressible. The total amount of work used during the specified time is obtained by solving the differential equation:

$$W(t) = \frac{V_0 \Lambda \Omega}{2} \int_0^t (\sigma_{zz} - \sigma_{xx}) \sin(\Omega t') dt', \quad (4.19)$$

here $V_0 = l_0 A_0$ is the initial sample volume.

We integrate the data presented in figure 4.6 and calculate the work, and the results are shown in figure 4.7.A. The amount of work increases monotonically during stretching, while we see a large energy recovery after reversing the flow ($t\nu > 0.5$). Due to viscous relaxation the sample will not recover completely to its initial state. As the red curve represent ideal reversible flow the local minimum represent the point where the force in figure 4.6 becomes negative. Still considering ideal deformation, we see that some of the energy used to squeeze the sample in the first cycle is also stored, and causes the curve to decrease again when starting a new cycle ($t\nu > 1$). The ideal prediction compares well to experimental data (black crosses) until the red curves reaches the local minima. In reality the sample is not squeezed but buckles and the work will therefore not increase again as predicted in the ideal case. The FEM predictions with both the Lodge model and the DE network model captures this trend and predicts the data very accurately. However, the final amount of work needed at the end of the first cycle is slightly overestimated compared to experimental data.

In figure 4.8 we show experimental results for sample A and B at three different frequencies, and at two different strain amplitudes for sample A. The data obtained with sample B shown in figure 4.8.A, are compared to the FEM results obtained with both the Lodge model and the DE network model.

A general observation in figure 4.8 is that besides frequency dependency we also see a large strain dependency. To analyze this further we will look at the relative amount of elastic recovery. To do so we define the relative amount of work performed by the sample as

$$XW_{ER} = \frac{\left(\frac{W}{V_0 G_0}\right)_{\max} - \left(\frac{W}{V_0 G_0}\right)_{\min}}{\left(\frac{W}{V_0 G_0}\right)_{\max}}, \quad (4.20)$$

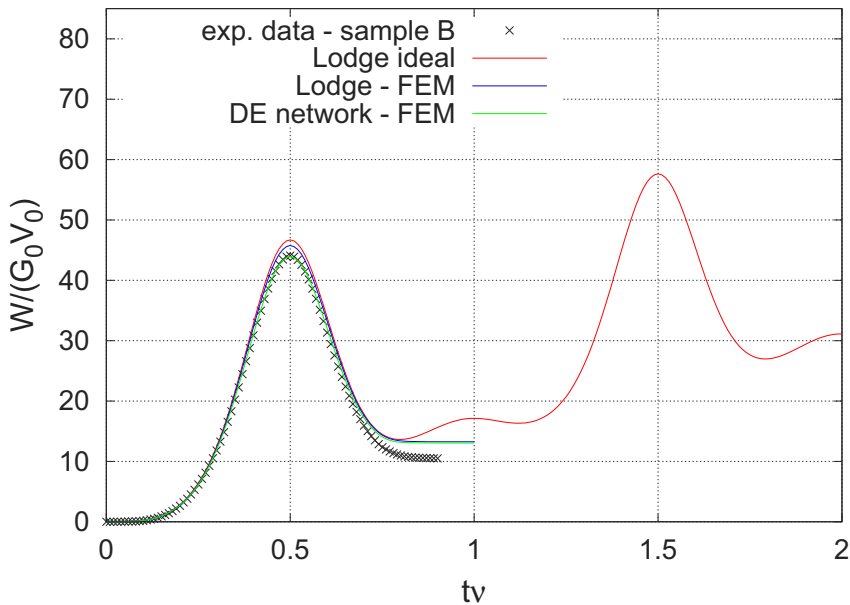


Figure 4.7: Work performed for sample B, when $\Omega = 0.4 \cdot \pi$ rad/s and $\Lambda = 2$. The red curve is the ideal Lodge prediction for two cycles, while the blue and green curves represent the FEM results obtained with the Lodge and the DE network models, respectively. The black crosses are experimental data.

where *max* and *min* denotes the local maxima and the final plateau of the experimental data in figure 4.8. The results for XW_{ER} are shown in figure 4.9. We observe that the elastic storage show little angular frequency dependency, however, it reaches a plateau as the frequency decreases. We can explain this by referring to the linear viscoelastic data presented in the previous chapter in figure 3.4 and 3.5. The mechanical response is dominated by the frequency independent plateau modulus at low frequencies, while at intermediate to high frequencies, G' and G'' , are of the same order of magnitude, and the viscous response will thus also be important. This change in mechanical response is causing the frequency behavior in figure 4.9. Comparing the results for sample A obtained at two strain amplitudes, shows that the elastic recovery is highly dependent on this parameter.

To understand this result better, we will look at the work expressions for two extreme cases; namely deformation of a purely elastic material and a Newtonian material. We will in both cases assume small deformations, *i.e.*, $\epsilon \ll 1$, hence, the stretch ratio can be simplified

$$\lambda = \exp \epsilon \simeq 1 + \epsilon. \quad (4.21)$$

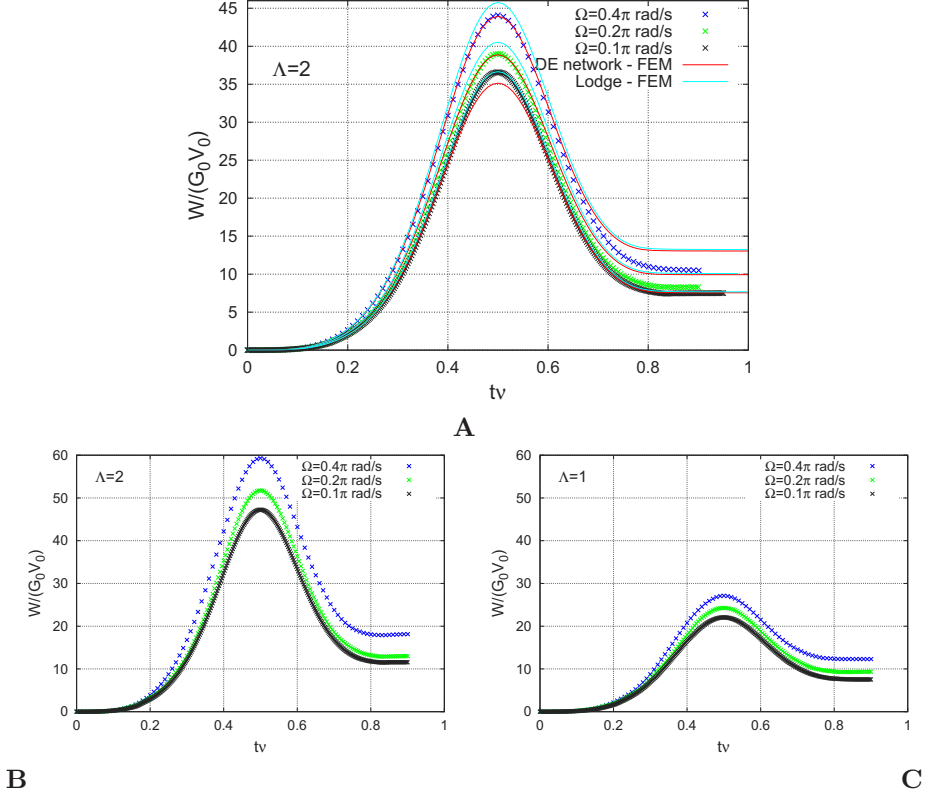


Figure 4.8: (A) Work needed to elongate sample B at three different frequencies with $\Lambda = 2$. The red curves represent FEM predictions with the DE network model, while the cyan curves represent FEM results obtained with the Lodge model. (B) Work needed to elongate sample A at three different frequencies with $\Lambda = 2$ and (C) Work needed to elongate sample A at three different frequencies with $\Lambda = 1$.

The stress difference in the purely elastic case is then

$$(\sigma_{zz} - \sigma_{xx})_E = 4G\epsilon, \quad (4.22)$$

when the nonlinear strain tensor is the Lodge model. G is the elastic modulus. The work needed to deform an elastic material is obtained by inserting the above expression into equation 4.19

$$\frac{W(t)}{V_0 G} = 2\Lambda^2 \left(\frac{3}{4} - \cos \Omega t + \frac{1}{4} \cos 2\Omega t \right). \quad (4.23)$$

We see from this equation that the work is frequency independent, while highly dependent on the strain amplitude. In the viscous case we assume that the stress difference is

$$(\sigma_{zz} - \sigma_{xx})_V = 4\eta\dot{\epsilon}, \quad (4.24)$$

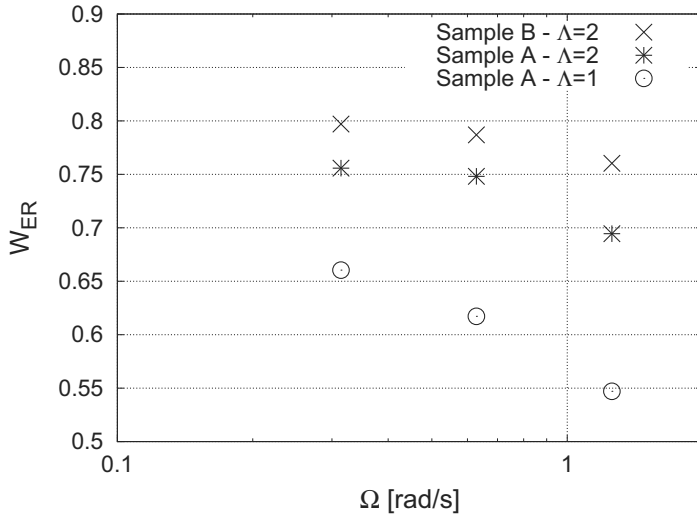


Figure 4.9: The relative amount of work performed by the samples upon flow reversal versus angular frequency.

with η as the viscosity. Inserting this into equation 4.19 gives

$$\frac{W(t)}{V_0(\eta\Omega)} = \Lambda^2 \left(\Omega t - \frac{1}{2} \sin 2\Omega t \right), \quad (4.25)$$

Once again we see a high dependency on the strain amplitude, but in this case there is also a frequency dependency. Hence, the frequency dependency obtained with our material are due to viscous material responses. However, the frequency dependency is not very pronounced, as the samples are primarily elastic.

Time-Strain Separation

To illustrate that the time-strain separability is largely an effect of dominant elastic behavior, we will compare the Lodge model and the DE network model to the calculated stress-differences for each of the two samples and discuss the differences.

Figure 4.10 shows that both the Lodge and the DE network model captures the calculated stress-differences of sample B very well. Due to the remarkable comparison, it has been shown that the material stress is nearly time-strain separable (some time time dependency is observed as the frequency increases). As a consequence, the energy loss can be described solely based on the linear viscoelastic relaxation. In contrast, Nielsen *et al.* [54], used a MSF constitutive formulation, to describe the stress in reversible flow of a polystyrene (PS) melt. The MSF formulation is not time-strain separable, which clearly states that some nonlinear relaxation behavior takes place for this type of fluid.

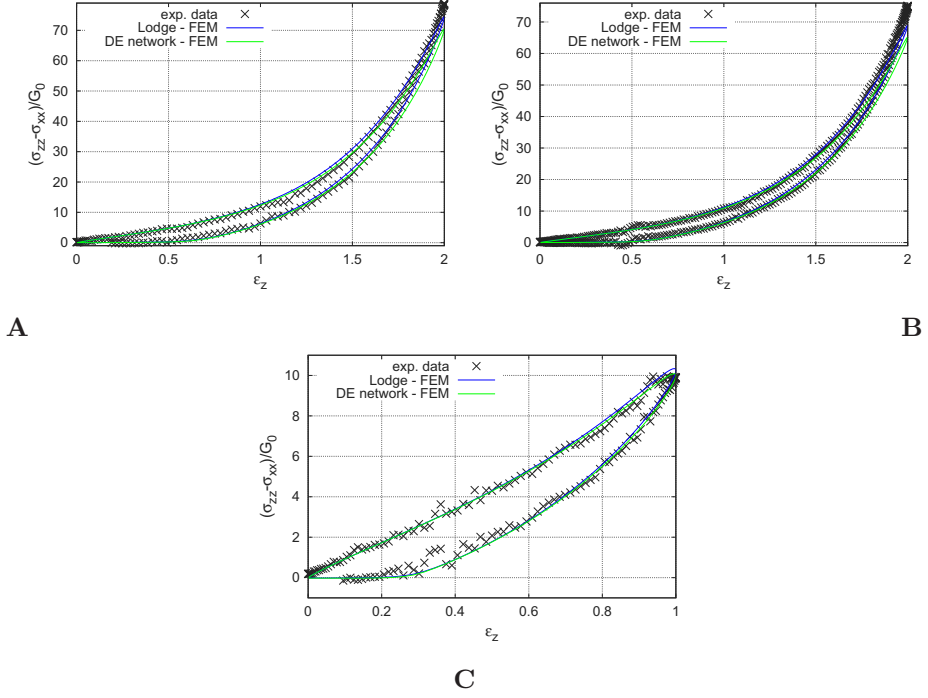


Figure 4.10: The stress difference for sample B, when (A) $\Omega = 0.2 \cdot \pi$ rad/s and $\Lambda = 2$ and (B) $\Omega = 0.1 \cdot \pi$ rad/s and $\Lambda = 2$ and finally (C) $\Omega = 0.2 \cdot \pi$ rad/s and $\Lambda = 1$. The blue line is the FEM simulation with the Lodge model, while the green is obtained using the DE network model.

Figure 4.11 shows the stress differences obtained with sample A for $\Lambda = 1$ and 2 and $\Omega = 0.2\pi$ rad/s. The ideal predictions of the DE network model and Lodge model are compared to the data. In contrast to the results for sample B, it is observed that the models slightly underestimates the stress, even at low strains. We expect this deviation to be due to the more viscous character of sample A compared to B. Hence the softer the network, the more will it deviate from a behavior described by the two models, which are time-strain separable. This observation is not unusual, since the networks will start to behave more like highly branched melts as $r \rightarrow r_c$, and we cannot expect the stress for melts to be time-strain separable.

4.4 Conclusion

The newly developed test fixture, designed to measure planar elongation on soft polymeric networks, has been used to measure reversible planar elongation on a FSR. This measuring technique gives information about the elastic recovery of the samples, *i.e.*, we can extract how much work the sample perform on the

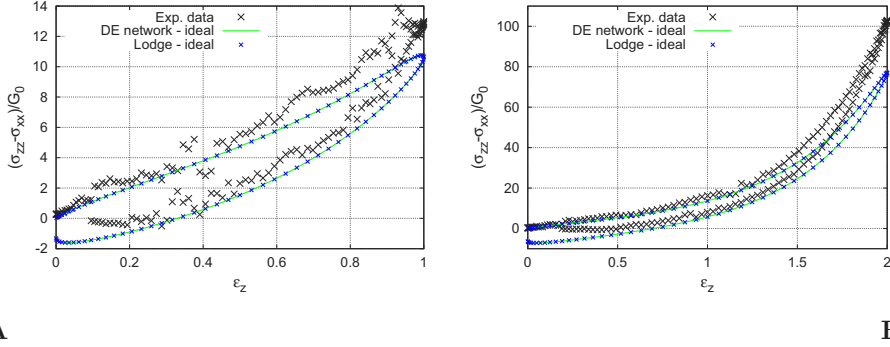


Figure 4.11: The stress difference for sample A, when $\Omega = 0.2 \cdot \pi$ rad/s and (A) $\Lambda = 1$ and (B) $\Lambda = 2$. The green is the ideal prediction of the DE network model.

external system, when reversing the flow.

We found that the deformation on the cylindrical probe was negligible compared to the overall deformation, and we thus, concluded that the deformation can be considered as nearly planar. A finite element approach, based on the K-BKZ constitutive equation, was used to analyze this deformation. We used two choices of strain tensors; a modified Lodge model and a new approximation to the Doi-Edwards model without independent alignment, called the DE network model. It was found that this new DE network model described the cylindrical deformation very well, which demonstrated, once again, that the choice of strain tensor is very important when looking at this deformation.

The measured stress differences were used to analyze the elastic recovery of the samples. This was done by calculating the work needed to deform the samples. It was found that the work added to stretch the samples was almost regained when reversing the flow. However, due to some viscous relaxation we do not recover all the energy. An estimate of the relative elastic recovery shows that this parameter is highly sensitive to the strain amplitude, while little frequency dependency is observed. In particular it is observed that the frequency dependency vanishes as the frequency reaches the equilibrium plateau regime in linear viscoelastic measurements, which is where elastic material behavior is dominant. This implies that no nonlinear effects influences the energy loss.

The FEM predictions with both models capture the measured stresses well, and by that we can state that the stress of polymeric networks is nearly time-strain separable especially at low frequencies. Hence, the energy loss of soft polymeric networks, can be described solely by the linear viscoelastic relaxation.

Chapter 5

Self-consistent modeling of entangled networks

Linear viscoelastic (LVE) measurements as well as non-linear elongation measurements have been performed on stoichiometrically imbalanced polymeric networks to gain insight into the structural influence on the rheological response. In particular we seek knowledge about the effect of dangling ends and soluble structures.

To interpret our recent experimental results we exploit a molecular model that can predict LVE data as well as non-linear stress-strain data. The discrete slip-link model (DSM) has proven to be a robust tool for both LVE and non-linear stress-strain predictions for linear chains, and it is thus used to analyze the experimental results. The relaxation modulus, $G(t)$, is obtained from Green-Kubo simulations of the model and a modified Baumgaertel, Schausberger and Winter (BSW) spectrum converts the relaxation modulus into the storage, G' , and loss, G'' , moduli in the frequency domain.

We divide the LVE response into three frequency domains; 1) the low frequency region, where G' is approaching a rubbery plateau, G_0 , 2) the intermediate region, where G' and G'' are parallel and 3) the third region is where G' levels off to an entanglement plateau, G_N^0 , close to that of the linear polymer. The latter region is seldom obtained in LVE experiments, although it is expected theoretically.

Initially we consider a stoichiometrically balanced network, i.e., all strands in the ensemble are attached to the network in both ends. We call this an ideal entangled network (IEN). Hereafter we add dangling strands to the network representing the stoichiometric imbalance, or imperfections during curing.

By considering monodisperse network strands without dangling ends, we find that the relative plateau, G_0/G_N^0 , decreases linearly with the average number of entanglements. The decrease from G_N^0 to G_0 is a result of monomer fluctuations between entanglements, which is similar to “longitudinal fluctuations” in tube

theory. Additionally we observe that, when transferring $G(t)$ into the frequency domain, G' is dominating at all frequencies compared to G'' . Experimental observations of stoichiometrically imbalanced networks show that G'' and G' are of the same order of magnitude at intermediate frequencies. Hence, the DSM suggests that energy dissipation at intermediate to low frequencies is almost entirely a result of dangling ends and soluble structures.

Energy dissipation is increased by adding a fraction of dangling ends, w_{DS} , to the ensemble, which suggests that the fraction of network strands, $w_{\text{NS}} = 1 - w_{\text{DS}}$, largely influences the plateau value at low frequencies. It is further found that the slope of G' is dependent on w_{NS} and the structural distribution of the network. The power-law behavior of G'' is not yet captured quantitatively by the model, but it suggests that it is a result of polydisperse dangling and soluble structures.

5.1 Introduction

Over the past four to five decades researchers have studied the influence of molecular structure in polymer networks on their mechanical properties [6–8, 22, 30, 33, 81, 82], and it is known that dangling ends and soluble structures have a large impact on the network relaxation behavior. Experimental evidence has shown that the equilibrium modulus, G_0 , obtained at long time scales is largely influenced by; 1) the concentration of effective network strands, *i.e.*, linear polymers connected to the elastically active network at both ends and 2) the fraction of trapped entanglements [22, 23, 34]. Several models have been proposed to describe the elasticity of polymer networks [34]. However, despite great effort the time dependent entanglement effect on relaxation of polymeric networks remains unresolved [83].

Modeling is hindered by the fact that real networks will never be perfectly cross-linked and thus consist of very complicated structures. This is either a result of “imperfect” reactions, such as looping, or because the cross-linking reaction is hindered by stoichiometry (*i.e.*, an excess of one of the components) or inhibition of the cross-linking reaction [45].

Depending on the stoichiometry of the system the dangling sub-structures and soluble sub-structures (also called the sol fraction) will have a range of compositions of linear and branched molecules which contribute differently to the material behavior [33]. For a detailed description of stochastic models describing this composition, see references [22, 25–27, 29].

The present work is a theoretical study of the entanglement contribution to stress relaxation of stoichiometrically imbalanced networks. The study is based on the discrete slip-link model (DSM) introduced by Schieber, Neergaard and Gupta in 2003 for melts [84, 85], and further developed by Khaliullin *et al.* [86, 87]. The application of the DSM model used here is nearly identical to the one for melts except here we will introduce two applications of the DSM; first an ideal entangled network (IEN) model where we consider a model network that is stoichiometrically cross-linked and no dangling ends or soluble sub-structures

are present. A sketch of of a small portion of such a model network is shown in figure 5.1 where gray circles indicate entanglements between network strands and black crosses represents the cross-links. The entanglements will be permanent (or trapped), since all strands are attached to the permanent network at the ends.

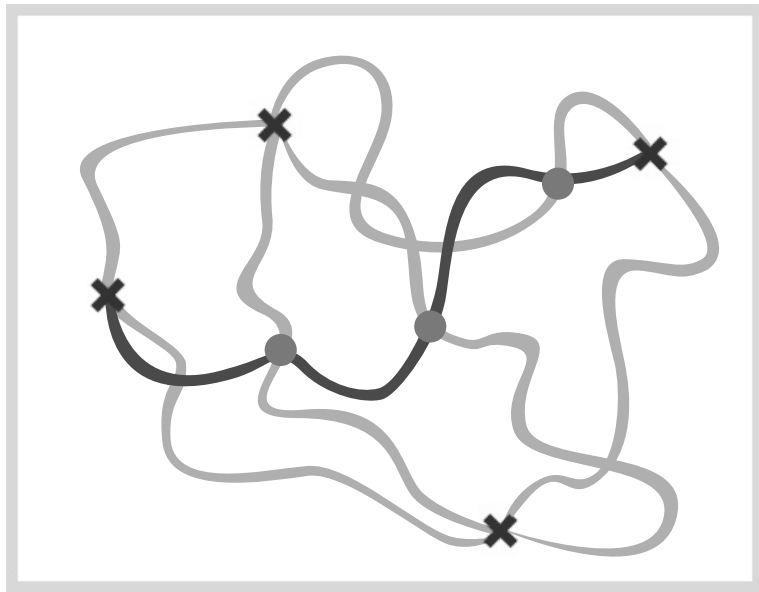


Figure 5.1: Drawing of an ideal entangled network (IEN). All cross-linking points are reacted and no dangling ends, are present. The cross-linkers are represented as discrete points (black crosses) and gray circles are marking the trapped entanglements.

Secondly we introduce an application of the DSM for entangled networks with dangling strands, this application is a coupling of two network architectures; 1) entangled network strands (ENS) and 2) entangled dangling strands (EDS). In the ENS architecture the entanglements can be destroyed by a process called constraint dynamics (CD). This process arises from the presence of entangled dangling strands (EDS).

As mentioned in the introduction, these dangling structures tend to have a broad molecular-weight distribution and can differ very much in architecture [22], *e.g.*, a dangling end can be highly branched or linear. All these different types of architectures will add a very broad relaxation time spectrum to the network rheological response. For convenience, we will simplify the system and assume that all dangling strands are linear and monodisperse. The illustration in figure 5.2 shows the two types of strands that will be described by the ENS and EDS architectures respectively. Two types of entanglements are also shown, where the trapped ones are marked with black rings.

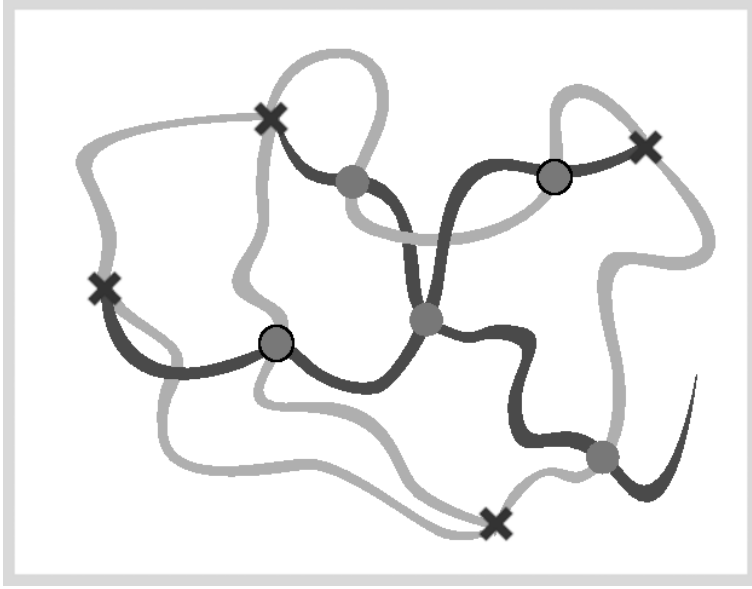


Figure 5.2: Illustration of a network with elastic active network strands and a dangling strand. Gray circles mark entanglements, where the trapped have been marked additionally with black rings. The cross-linking points are considered as discrete points and marked as black crosses.

5.2 The Discrete Slip-link Model

5.2.1 Ideal Entangled Network

The network strands are described by random walk statistics. This is expected to hold for polymeric chains with contour length and entanglement spacing larger than several Kuhn steps. The model is a single-strand mean field model, where figure 5.3 shows cartoons of the coarse-graining process of the real network strand. First the strand is coarse-grained by random walk statistics, hereafter the primitive path length due to entanglements is defined. The entanglements are added randomly with probability $1/(\beta + 1)$, where β is a model parameter related to the entanglement density of the surrounding chains, and will be defined later in this section. The primitive path defines the entanglement spacing, while the random walk chain defines the number of Kuhn steps between each entanglement.

The parameters and variables used for the coarse-grained entangled strand are listed in Table 5.1. Since all entanglements are trapped in the IEN model, Z for a given strand is constant, though chosen from a distribution, while the monomer density, N_i , fluctuates due to Kuhn step shuffling through the slip-links. This process is called sliding dynamics (SD) and is illustrated in figure 5.4.

The random walk of N_i Kuhn steps between two slip-links of separation

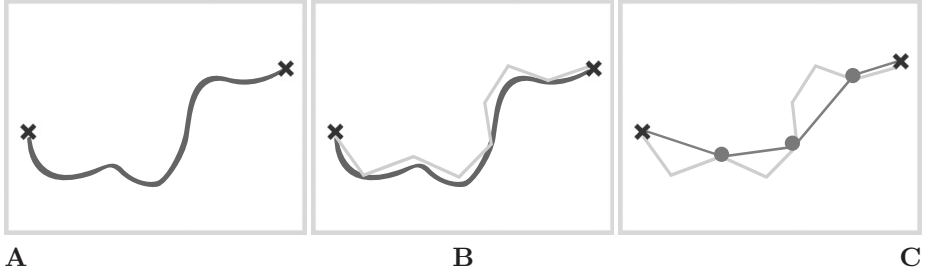


Figure 5.3: A: A single network strand between two cross-links. B: A coarse-grained random walk chain (light gray) imaged above the real chain (dark gray). C: The primitive path chain (dark gray) imaged above the random walk chain. The primitive path is longer than the end-to-end distance between cross-links (black crosses) due to entanglements (gray circles).

Table 5.1: Parameters and variables of the coarse-grained chain.

Parameters	Description
Z	Number of entangled segments
N_K^γ	Total number of Kuhn steps in one strand ^a
a_K	Length of a Kuhn step
N_i	Number of Kuhn steps in segment i
Q_i	Orientation vector between entanglements i and $i + 1$

^a $\gamma \equiv N, D$ indicates that we can work with two different architectures in the second model application.

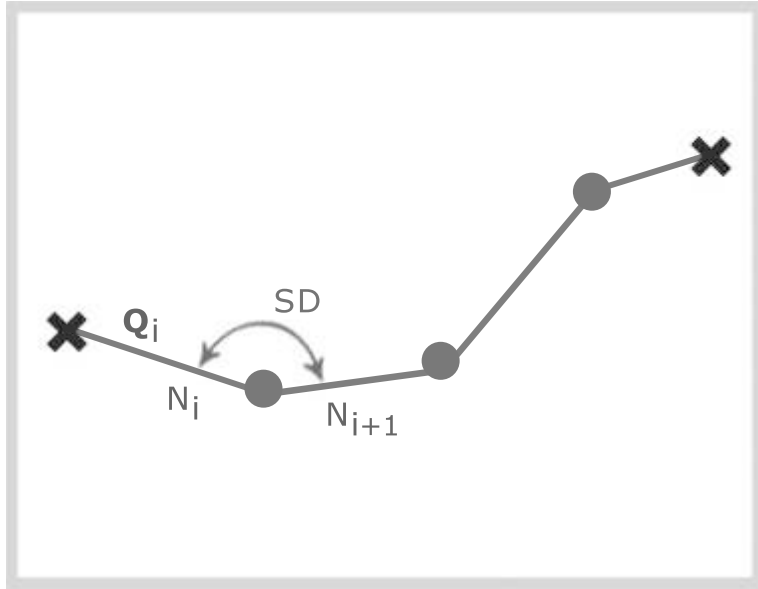


Figure 5.4: Entangled network chain with primitive path statistics. The number of strands, Z , is 4. Kuhn steps can shuffle through the slip-links due to sliding dynamics.

$|\mathbf{Q}_i| = Q_i$ can be approximated by a Gaussian free energy

$$\frac{F_i(\mathbf{Q}_i, N_i)}{k_B T} = \frac{3Q_i^2}{2N_i a_K^2} + \frac{3}{2} \ln \left(\frac{2\pi N_i a_K^2}{3} \right), \quad (5.1)$$

where k_B is the Boltzmann constant and T the absolute temperature. a_K is the length of a Kuhn step. The free energy of the network strand (NS) is thus the sum over all the entangled segments

$$F(\Omega) = \sum_{i=1}^Z F_i(\mathbf{Q}_i, N_i), \quad (5.2)$$

where $\Omega \equiv (Z, \{N_i\}, \{\mathbf{Q}_i\}, \{\tau_i^{\text{CD}}\})$ is the strand conformation. The equilibrium distribution for such a strand is given by the modified Maxwell-Boltzmann relation [86]

$$p_{\text{eq}}^\gamma(\Omega) = \frac{\delta \left(N_K^\gamma, \sum_{i=1}^Z N_i \right)}{J} \exp \left[-\frac{F(\Omega)}{k_B T} \right] \exp \left[\frac{\mu^{\text{E}}(Z-1)}{k_B T} \right] \prod_{i=1}^{Z-1} p^{\text{CD}}(\tau_i^{\text{CD}}). \quad (5.3)$$

where $\delta(i, j) := \delta_{i,j}$ is the Kronecker delta function which conserves the number of Kuhn steps in a cross-linked strand and $J = (1 + 1/\beta)^{N_K-1}$ is a normalization constant. $p^{\text{CD}}(\tau_i^{\text{CD}})$ is a probability density for the i^{th} entanglement to have a characteristic CD lifetime τ_i^{CD} . In the IEN application entanglements will never be destroyed by CD; hence, τ_i^{CD} is infinitely large and $p^{\text{CD}}(\tau^{\text{CD}}) = \delta(1/\tau^{\text{CD}})/(\tau^{\text{CD}})^2$. The second exponential in equation 5.3, which includes the entanglement chemical potential of the surroundings, μ^{E} , acts as a process of entanglement exchange with a bath of entanglements on the mean-field chain. For later derivations it is convenient to define $\beta := \exp(-\mu^{\text{E}}/k_B T)$. For infinitely long linear chains, $\beta + 1$ is equal to the average number of Kuhn steps in an entangled segment, $N_e := \lim_{N_K \rightarrow 0} \langle N_i \rangle_{\text{eq}}$. We relate it to the pure uncross-linked polymer by

$$G_N^0 \simeq \frac{\rho R T}{M_K(\beta + 1)}, \quad (5.4)$$

which is derived for long uncross-linked linear polymers [86]. G_N^0 is the plateau modulus of the uncross-linked polymer melt and comparable to, but larger than, the apparent plateau modulus observed experimentally [85, 86]. M_K is the molecular weight of a Kuhn step, ρ the density and R the ideal gas constant.

Stress Relaxation for Network Strands

The relaxation modulus, $G(t)$, is obtained using the Green-Kubo expression

$$G(t) = \frac{1}{nk_B T} \langle \tau_{xy}(0) \tau_{xy}(t) \rangle_{\text{eq}}, \quad (5.5)$$

where n is the number density of strands and τ_{xy} is any off-diagonal component of the stress tensor. The stress tensor is obtained from the strand free energy

$$\boldsymbol{\tau}(t) = -n \left\langle \sum_{i=1}^Z \mathbf{Q}_i \left(\frac{\partial F(\boldsymbol{\Omega})}{\partial \mathbf{Q}_i} \right)_{T, \{N_i\}, \{\mathbf{Q}_{j \neq i}\}} \right\rangle, \quad (5.6)$$

where $\langle \dots \rangle$ is an ensemble average.

Equilibrium Dynamics for IEN

At equilibrium, Kuhn steps can shuffle through entanglements driven by Brownian forces and free energy differences between entangled segments. The evolution equation for the probability density describing the conformation of a chain is given by the master equation [84]

$$\begin{aligned} \frac{\partial p(\Omega, t | \Omega_0, t_0)}{\partial t} &= - \sum_{i=1}^Z \frac{\partial}{\partial \mathbf{Q}_i} \cdot [\boldsymbol{\kappa} \cdot \mathbf{Q}_i] p(\Omega, t) + \int W(\Omega | \Omega') p(\Omega', t | \Omega_0, t_0) d\Omega' \\ &- \int W(\Omega' | \Omega) p(\Omega, t | \Omega_0, t_0) d\Omega', \end{aligned} \quad (5.7)$$

where $\boldsymbol{\kappa}$ is the transpose of the velocity gradient. We assume affine entanglement motion which means that $d\mathbf{Q}_i/dt = \boldsymbol{\kappa} \cdot \mathbf{Q}_i$. $p(\Omega, t | \Omega_0, t_0)$ is the probability density of having conformation Ω given that the previous conformation was Ω_0 . $W(\Omega' | \Omega)$ is a transition probability from conformation Ω to conformation Ω' per unit time, and it is given by

$$W = \sum_{i=1}^{Z-1} W_{\text{sh}}^i, \quad (5.8)$$

where W_{sh}^i is the transition rate probability for Kuhn-step shuffling through entanglement i . When deriving expressions for the transition probability we satisfy detailed balance

$$W(\Omega' | \Omega) = W(\Omega | \Omega') \frac{p_{\text{eq}}(\Omega')}{p_{\text{eq}}(\Omega)}, \quad (5.9)$$

which yields that $\partial p_{\text{eq}}(\Omega, t | \Omega_0, t_0) / \partial t = 0$ in equation 5.7.

Since Kuhn step shuffling is symmetric the transition probability to shift a Kuhn step between segments i and $i + 1$ is given by

$$\begin{aligned} W_{\text{sh}}^i(\Omega' | \Omega) &= \delta_{Z, Z'} \prod_{j=1}^Z \delta(\mathbf{Q}_j - \mathbf{Q}'_j) \sum_{j=1}^{Z-1} \delta(\boldsymbol{\tau}_j^{\text{CD}} - \boldsymbol{\tau}_j^{\text{CD}'}) \prod_{j=1, j \neq i, i+1}^Z \delta_{N_j, N'_j} \times \\ &\quad \left(\delta_{N_i, N'_i-1} \delta_{N_{i+1}, N'_{i+1}+1} + \delta_{N_i, N'_i+1} \delta_{N_{i+1}, N'_{i+1}-1} \right) \times \\ &\quad \frac{2(\beta + 1)}{\tau_K(N_i + N_{i+1})} \exp \left[\frac{F(\Omega') - F(\Omega)}{2k_B T} \right], \end{aligned} \quad (5.10)$$

The first line in the equation preserves conformations of the segments that are not involved in the Kuhn step shuffling. The second line ensures that only one Kuhn step can slide through entanglement i at a time. The exponential in the last line is obtained from detailed balance, equation 5.9, and the symmetry assumption and shows that Kuhn step shuffling is a result of free energy differences. The underlined term is related to the friction coefficient of the strand, where it is assumed that the total chain friction is proportional to N_K , hence, we have constant chain friction. τ_K is a time constant equal to the average time it takes for one Kuhn step to slide through an entanglement and it is dependent only on chemistry, temperature and concentration, if solvent is present. The friction coefficient related to shuffling from strand i to $i+1$ is therefore assumed to be proportional to $\tau_K(N_i + N_{i+1})$. For more details, see Khaliullin *et al.* [86].

5.2.2 Entangled Network Strands and Entangled Dangling Strands

In this section we introduce the second application of the DSM, where we combine two architectures of network strands: one for entangled network strands (ENS) and one for entangled dangling strands (EDS). The dangling strands will have one free-end segment where entanglements can be created and destroyed by SD, while some fraction of entanglements can be created and destroyed anywhere on the strand by CD. This latter process is caused by the SD of surrounding dangling strands. These two processes are illustrated in figure 5.5 where drawings of a coarse-grained network strand and a dangling strand are shown.

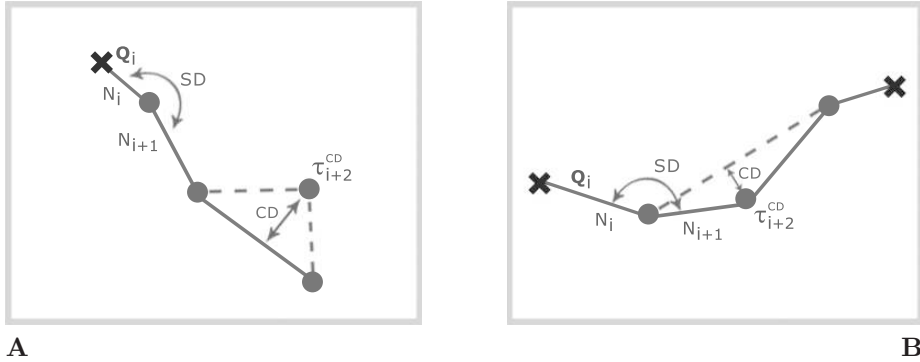


Figure 5.5: **A:** An entangled dangling strand (EDS). **B:** An entangled network strand (ENS). Gray circles are marking the entanglements, while black crosses resembles the cross-links.

Due to SD and CD the number of entangled strands, Z , can now fluctuate for a given strand. Compared to the IEN model, only minor changes need to be made in the ENS model, where only CD has to be introduced, while more modifications are necessary for the dangling strands; e.g. the free energy and the creation and destruction of entanglements by SD. The free energy for each of

the entangled segments is the same as in equation 5.1, however the free energy of the whole dangling strand will be the sum over all segments except the free end segment

$$F(\Omega) = \sum_{i=1}^{Z-1} F_i(Q_i, N_i). \quad (5.11)$$

Stress Relaxation of Dangling Strands

The dangling strand contribution to stress is equivalent to that of the network strand (equation 5.6)

The relaxation modulus for each structure, G_{NS} and G_{DS} respectively, will be obtained from Green-Kubo simulations of the two ensembles, while $G(t)$ for the combined system is a linear superposition of the relaxation moduli of the two components

$$G(t) = w_{\text{NS}}G_{\text{NS}}(t) + w_{\text{DS}}G_{\text{DS}}(t), \quad (5.12)$$

where w_{NS} and w_{DS} is the fraction of network strands and dangling strands respectively. It is important to note that the network strands and dangling strands do influence each other through CD.

Equilibrium Dynamics for ENS and EDS

As was done for melts [86] we mimic the process of spontaneous destruction and creation of entanglements on a strand without pairing different ensemble members. This is done by assigning each entanglement on the strand a characteristic lifetime τ^{CD} upon its creation. Hence in contrast to the IEN application, τ^{CD} in equation 5.3 might now be assigned a finite value. The transition probability $W(\Omega'|\Omega)$ can now be separated into several parts

$$W = \left(\sum_{i=1}^{Z-1} W_{\text{sh}}^i \right) + W_{\text{d}}^{\text{SD}} + W_{\text{c}}^{\text{SD}} + W_{\text{d}}^{\text{CD}} + W_{\text{c}}^{\text{CD}}. \quad (5.13)$$

W_{d}^{SD} and W_{c}^{SD} represent destruction and creation of the entanglements on the end of the dangling strand due to SD (these terms are zero in the ENS model), and W_{d}^{CD} and W_{c}^{CD} represent destruction and creation of the entanglements anywhere on the strand due to CD.

We assume a simple form for the destruction rate by SD such that it only depends on the friction of one Kuhn step. As a result, the creation transition probability calculated from detailed balance yields a Gaussian distribution for

the newly entangled segments

$$W_d^{\text{SD}}(\Omega'|\Omega) = \delta_{Z,Z'+1} \delta_{N_Z-1, N'_Z-1} \delta_{N_Z,1} \frac{2(\beta+1)}{\tau_K (N_{Z-1}+1)} \prod_{j=1}^{Z-1} \delta_{\Omega_j, \Omega'_{j-1}}, \quad (5.14)$$

$$\begin{aligned} W_c^{\text{SD}}(\Omega'|\Omega) &= \delta_{Z,Z'-1} \delta_{N_Z, N'_Z+1} H(N_Z-2) \frac{2(\beta+1) p^{\text{CD}}(\tau_1^{\text{CD}'})}{\tau_K \beta N_Z} \\ &\times \left[\frac{3}{2\pi(N_Z-1)a_K^2} \right]^{3/2} \exp \left[-\frac{3Q_{Z-1}'^2}{2(N_Z-1)a_K^2} \right] \prod_{j=2}^Z \delta_{\Omega_j, \Omega'_{j+1}}, \end{aligned} \quad (5.15)$$

where $\delta_{\Omega_i, \Omega'_k}$ is short hand for the preservation of the conformation of a single segment

$$\delta_{\Omega_i, \Omega'_k} := \delta_{N_i, N'_k} \delta(\tau_i^{\text{CD}} - \tau_k^{\text{CD}'}) \delta(\mathbf{Q}_i - \mathbf{Q}'_k). \quad (5.16)$$

W_c^{SD} follows from W_d^{SD} and detailed balance equation 5.9.

The destruction rate transition probability for CD for the i^{th} entanglement is modeled similar to a first-order reaction

$$\begin{aligned} W_d^{\text{CD}}(\Omega'|\Omega) &= \frac{1}{\tau_i^{\text{CD}}} \delta_{Z,Z'+1} \sum_{i=1}^{Z-1} \prod_{j=1}^{i-1} \delta_{\Omega_j, \Omega'_j} \prod_{j=i+2}^Z \delta_{\Omega_j, \Omega'_{j-1}} \times \\ &\delta(\mathbf{Q}_i + \mathbf{Q}_{i-1} - \mathbf{Q}'_i) \delta_{N_i+N_{i-1}, N'_i}. \end{aligned} \quad (5.17)$$

The delta functions in the second line preserve the location and total number of Kuhn steps in the neighboring strands involved in the destruction process. From detailed balance we get the transition probability to create an entanglement by CD

$$\begin{aligned} W_c^{\text{CD}}(\Omega'|\Omega) &= \delta_{Z,Z'-1} \sum_{i=1}^Z \prod_{j=1}^{i-1} \delta_{\Omega_j, \Omega'_j} \prod_{j=i+1}^Z \delta_{\Omega_j, \Omega'_{j+1}} \times \\ &\delta(\mathbf{Q}_i - \mathbf{Q}'_i - \mathbf{Q}'_{i+1}) \delta_{N_i, N'_i+N'_{i+1}} \frac{p^{\text{CD}}(\tau_i^{\text{CD}'})}{\tau_i^{\text{CD}'}\beta} \times \\ &\left[\frac{3}{2\pi N'_i \left(1 - \frac{N'_i}{N'_{i+1}}\right)} \right]^{3/2} \exp \left[-\frac{3 \left(\mathbf{Q}'_i - \frac{N'_i}{N'_{i+1}} \mathbf{Q}'_{i+1} \right)^2}{2N'_i \left(1 - \frac{N'_i}{N'_{i+1}}\right)} \right]. \end{aligned} \quad (5.18)$$

5.2.3 Constraint Dynamics spectrum

Our aim is to obtain a CD spectrum $p^{\text{CD}}(\tau)$ such that, by assuming binary entanglements, the destruction of entanglements by SD and CD will be equal in time as seen in figure 5.6.

Doi and Takimoto [88] obtain this self-consistency by assuming that entanglements are binary events, where each entanglement is a pairing of two chains in the simulation ensemble. We also assume binary events. However, since

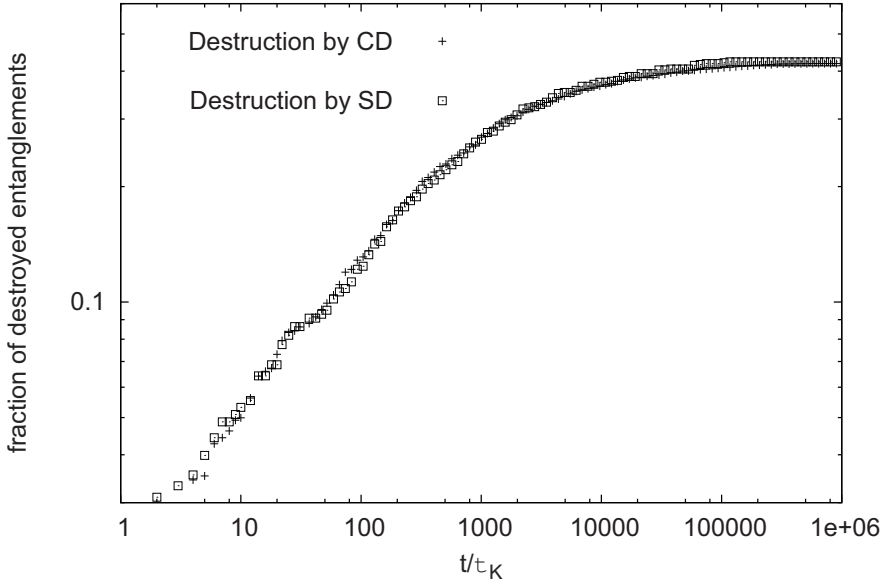


Figure 5.6: The fraction of destroyed entanglements by SD and CD. $N_K = 60$, $\beta = 20$ and $w_{DS} = 0.6$. The CD spectrum is that obtained in figure 5.7

single-chain simulations are computationally more efficient, we will construct $p^{\text{CD}}(\tau_i^{\text{CD}})$ self-consistently without pairing the chains.

There are two methods to obtain $p^{\text{CD}}(\tau_i^{\text{CD}})$; one is to follow the fraction, $f(t)$, of survived entanglements by SD which counts the number of entanglements from an arbitrary point in time until their destruction. The probability density is then constructed from

$$f(t) = \int_0^\infty p^{\text{CD}}(\tau^{\text{CD}}) \exp\left(-\frac{t}{\tau^{\text{CD}}}\right) d\tau^{\text{CD}}. \quad (5.19)$$

Another method is to keep track of the entanglements from their individual time of creation to their individual time of destruction. By doing so we weight the short-lived entanglements more than long-lived ones. From this we can get the cumulative distribution of lifetimes, $\mathbb{P}(t)$, which is related to $p^{\text{CD}}(\tau^{\text{CD}})$ through the following

$$f_d(t) = 1 - \mathbb{P}(t) = \frac{\int_0^\infty \frac{p^{\text{CD}}(\tau^{\text{CD}})}{\tau^{\text{CD}}} \exp\left(-\frac{t}{\tau^{\text{CD}}}\right) d\tau^{\text{CD}}}{\int_0^\infty \frac{p^{\text{CD}}(\tau^{\text{CD}})}{\tau^{\text{CD}}} d\tau^{\text{CD}}}. \quad (5.20)$$

Due to the weighting of lifetimes in $f_d(t)$, and since it is computationally much more efficient to track $f_d(t)$ rather than $f(t)$, we will use $f_d(t)$ to determine the CD spectrum.

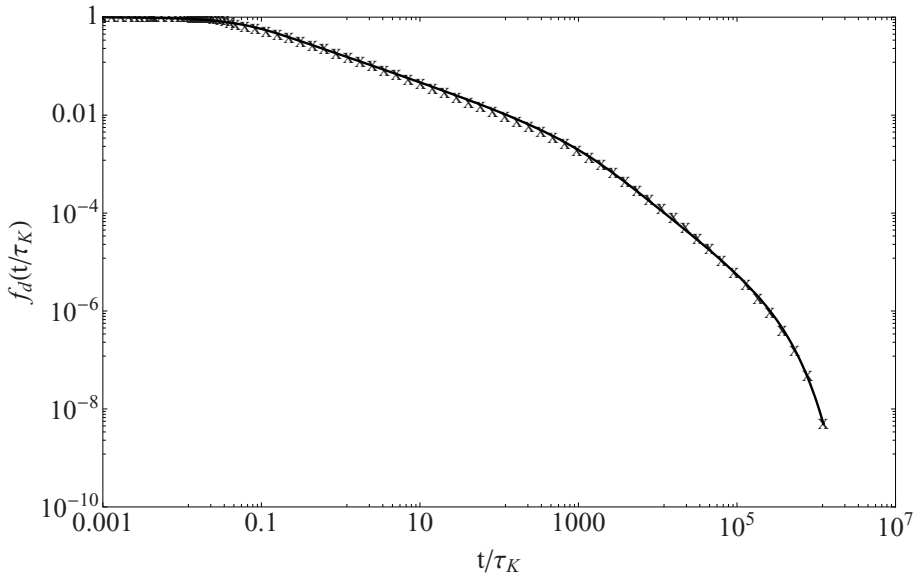


Figure 5.7: $f_d(t)$ obtained from a simulation of the EDS model with $N_K = 60$ and $\beta = 20$ and an ensemble of 100 chains. The crosses are simulated data, while the full line is a fitted spectrum: $\tau_0 = 0.0498$, $\tau_1 = 1151$, $\tau_2 = 264451$, $\alpha_1 = 0.453$ and $\alpha_2 = -0.271$

Since we will later compare the simulated results with experimental polypropylene oxide (PPO) data, we perform simulations with $N_K = 60$ and $\beta = 20$. The estimate of these parameters will be described later in section 5.3. The resulting $f_d(t)$ from a dangling strand simulation without CD is shown in figure 5.7. The curve differs from that of linear chains by having two power-law regions instead of one [86]. We assign the first power-law region to contour length fluctuations (CLF), and find that the slope is the same as the one for linear chains [86]. The reason for this is that the cross-link point does not have an influence on CLF at these short time scales. For linear chains, $f_d(t)$, drops very fast, like a single exponential, after the first power-law region, which is likely a result of reptation-like motion [86]. In the case of dangling strands another power-law region is observed. We also assign this to CLF but is faster than CLF for linear chains. This second region proves that the destruction of entanglements has been slowed down compared to reptation-like motion for linear chains. The increase in the slope as observed in figure 5.7 is, however, not yet understood. Milner and McLeish [89] found a similar tendency of slow and fast CLF.

Based on the observations of the $f_d(t)$ curve, we assume the following nor-

malized lifetime distribution probability

$$p^{\text{CD}}(\tau) = w_{\text{DS}} \left(\frac{\tau^{\alpha_1-1} H(\tau - \tau_0) H(\tau_1 - \tau)}{\frac{\tau_1^{\alpha_1} - \tau_0^{\alpha_1}}{\alpha_1} + \frac{\tau_2^{\alpha_2} - \tau_1^{\alpha_2}}{\alpha_2} \tau_1^{\alpha_1 - \alpha_2}} + \frac{\tau^{\alpha_2-1} H(\tau - \tau_1) H(\tau_2 - \tau) \tau_1^{\alpha_1 - \alpha_2}}{\frac{\tau_1^{\alpha_1} - \tau_0^{\alpha_1}}{\alpha_1} + \frac{\tau_2^{\alpha_2} - \tau_1^{\alpha_2}}{\alpha_2} \tau_1^{\alpha_1 - \alpha_2}} \right) + w_{\text{NS}} \frac{\delta(1/\tau)}{\tau^2}. \quad (5.21)$$

The delta function assigns an infinite lifetime to a fraction w_{NS} of entanglements. $\tau_0, \tau_1, \tau_2, \alpha_1$ and α_2 are fitting parameters used as the CD spectrum of the combined system (ENS + EDS). These parameters are found self-consistently and not by fitting to experimental data.

The fraction of destroyed entanglements by SD and CD for simulations of 1000 entangled network strands and 1000 entangled dangling strands with $N_K = 60$, $\beta = 20$ and $w_{\text{DS}} = 0.6$ is shown in figure 5.6. It is observed that the destruction by the two processes are equal in time, which confirms that our CD spectrum equation 5.21 is sufficiently accurate.

5.3 Results

We will transform the relaxation modulus into the frequency domain, $G^*(\omega) := i\omega \mathcal{F}\{G(t)\}$, since this is how experiments are most often performed. The analysis of the simulated results is divided into three frequency regimes; 1) the entanglement plateau, G_N^0 , regime obtained at high frequencies, 2) the power-law region at intermediate frequencies and 3) the equilibrium plateau, G_0 , regime obtained at short frequencies.

5.3.1 BSW spectrum

To estimate the Fourier transform of $G(t)$, we fit the simulated data with a mathematical expression. We use a modified Baumgaertel, Schausberger and Winter (BSW) spectrum [90], for which the relaxation time spectrum, $h(\tau)$, is given by

$$h(\tau) = \frac{\sum_{i=1}^m \tau^{\alpha_i} H(\tau_{i-1} - \tau) H(\tau - \tau_i) \prod_{j=1}^{i-1} \tau_j^{\alpha_j - \alpha_{j+1}}}{\sum_{i=1}^m \frac{\tau_i^{\alpha_i} - \tau_{i-1}^{\alpha_i}}{\alpha_i} \prod_{j=1}^{i-1} \tau_j^{\alpha_j - \alpha_{j+1}}}, \quad (5.22)$$

m is the number of modes in the spectrum, $H(\dots)$ the Heaviside stepfunction and τ_i and α_i are corresponding time constants and power-law exponents respectively. The denominator is a normalization and keeps $h(\tau)$ continuous.

For the IEN results we will only fit one mode, and equation 5.22 reduces to

$$h(\tau) = \frac{\alpha \tau^\alpha}{\tau_1^\alpha - \tau_0^\alpha} H(\tau_1 - \tau) H(\tau - \tau_0), \quad (5.23)$$

where τ_1 and τ_0 is the longest and shortest relaxation time respectively. The relaxation modulus is given by

$$G(t) = (G_N^0 - G_0) \int_0^\infty \frac{h(\tau)}{\tau} \exp\left(-\frac{t}{\tau}\right) d\tau + G_0, \quad (5.24)$$

where G_N^0 is the entanglement plateau.

5.3.2 Ideal Entangled Network

Our aim is to understand the entanglement effect on the rheological response of entangled networks. The entanglements studied here are divided into two classes; 1) trapped entanglements and 2) temporary entanglements. In the ideal network we have only trapped entanglements, and to study the effect of these on the relaxation behavior, we perform simulations on a number of ideal monodisperse model networks, where we vary N_K and β .

In figure 5.8 we show the Green-Kubo results of simulating 1000 IEN strands for different values of N_K and β . The results are normalized with the entanglement plateau modulus which is determined analytically as [84–86]

$$\frac{G_N^0}{\rho RT/M} = \langle Z \rangle_{\text{eq}} = \frac{N_K + \beta}{\beta + 1}, \quad (5.25)$$

All the lines represents the respective BWS fits, where the BSW parameters are listed in table 5.2. It is seen that the absolute value of G_0 increases with the number of entanglements. However, since G_N^0 also increases we see that the relative plateau, G_0/G_N^0 , decreases. Hence, the overall amount of relaxation increases linearly with the average number of entanglements. The equilibrium plateau is plotted versus the average number of entangled strands in figure 5.9. The amount of relaxation from G_N^0 to G_0 in these cases lies within $\sim 15\%$ to $\sim 25\%$. Together with the IEN data is a linear fit

$$\frac{G_{0,\text{IEN}}}{\rho RT/M} = 0.74(\langle Z \rangle_{\text{eq}} - 1) + 1, \quad (5.26)$$

which shows how the plateau modulus is related to the average number of (trapped) strands.

Figure 5.10 shows the power-law exponent, α , and the relaxation time, τ_1 , versus the average number of entanglements. It is expected that the more entanglements present, the longer time it takes to reach the equilibrium plateau. Likewise we find that the negative slope, $(\alpha - 1)$, of $G(t)$ becomes higher as the number of entangled strands increases, hence, α decreases. The errorbars on α , τ_0 and τ_1 appear big compared to their actual values. They are determined from a rather conservative estimation, where uncertainties on the simulated data points are not included. With a proper weighting based on the fluctuations in the simulated data, we expect the actual errorbars to be reduced considerably.

The resulting G^* spectrum, for $N_K = 60$ and $\beta = 20$, is shown in figure 5.11. It is seen that G' is dominating at all frequencies and it is difficult to see

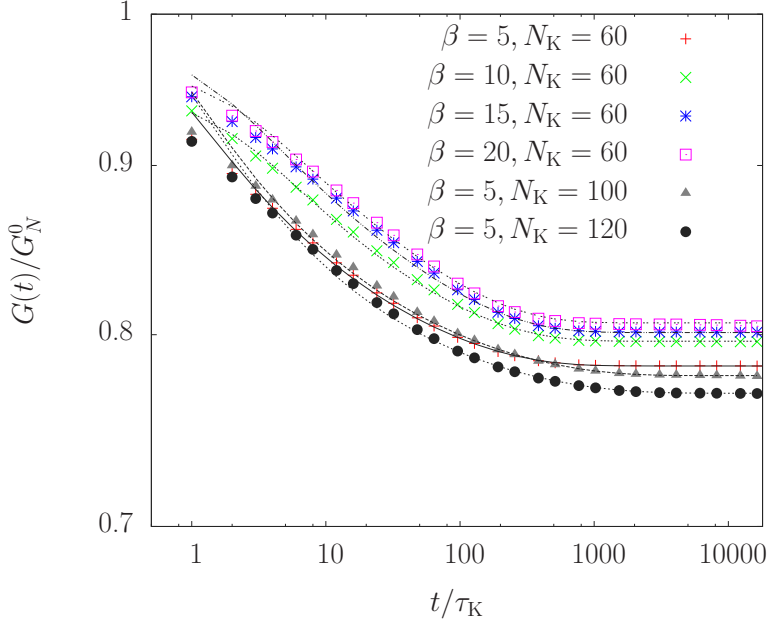


Figure 5.8: Relaxation modulus produced by the IEN model with $N_K = \{60, 100, 120\}$ and $\beta = \{5, 10, 15, 20\}$. All the black lines are the BSW fits of each data set.

Table 5.2: BSW parameters obtained by fitting equation 5.23 combined with equation 5.24 to the simulated data presented in figure 5.8.

N_K	β	G_0	α	τ_0	τ_1
60	5	8.3836 ± 0.0007	-0.29 ± 0.06	0.5 ± 0.2	410 ± 90
60	10	5.3263 ± 0.0001	-0.22 ± 0.09	2 ± 1	380 ± 60
60	15	3.80697 ± 0.00009	-0.15 ± 0.07	1.0 ± 0.7	370 ± 50
60	20	3.174 ± 0.001	-0.1 ± 0.1	2 ± 1	330 ± 80
100	5	13.111 ± 0.003	-0.33 ± 0.05	0.5 ± 0.2	1300 ± 300
120	5	15.490 ± 0.002	-0.37 ± 0.04	0.6 ± 0.2	1700 ± 500

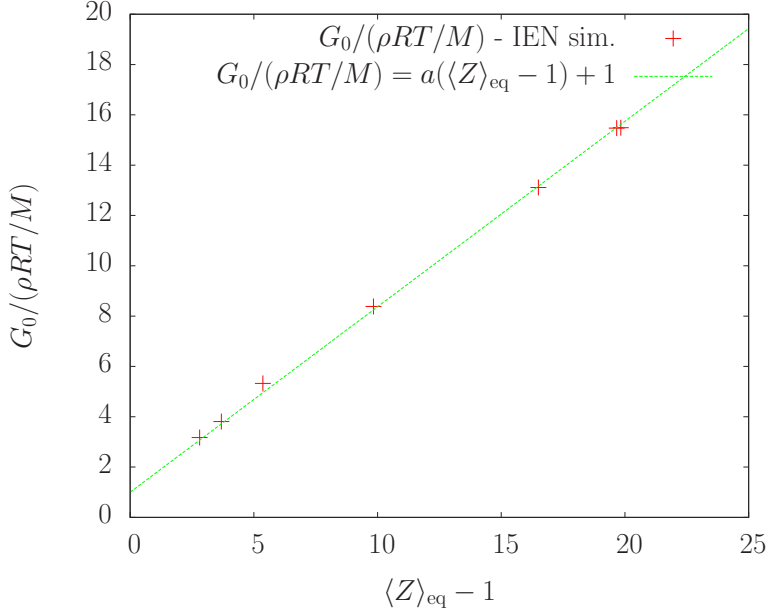


Figure 5.9: Equilibrium plateau modulus, G_0 , vs. the average number of entanglements, the line represents a linear fit to G_0 with $a = 0.74 \pm 0.05$.

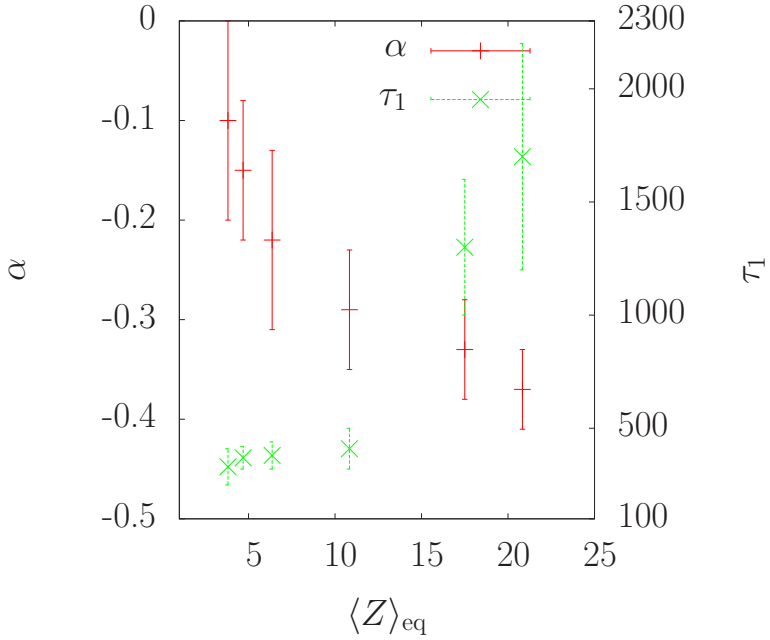


Figure 5.10: Power-law exponent, α , and the relaxation time, τ_1 , vs. the average number of entanglements.

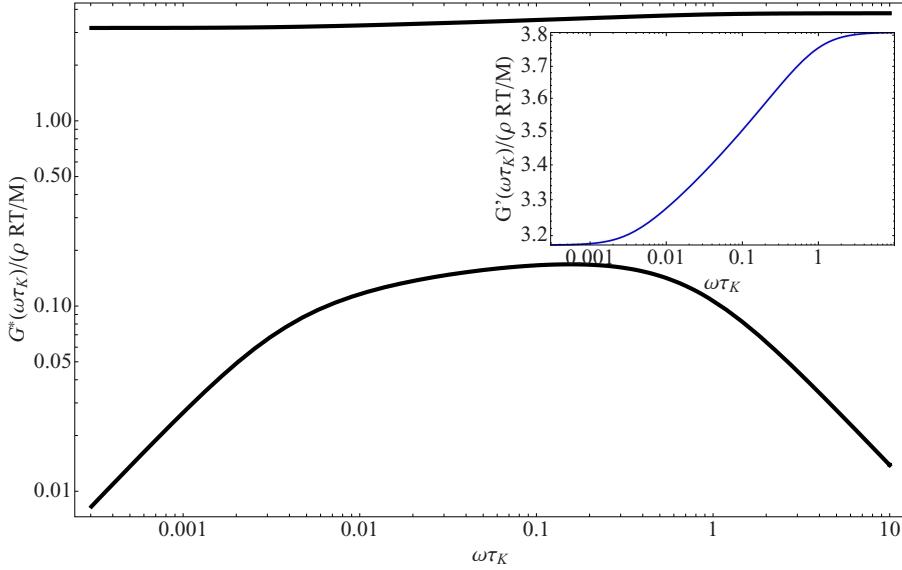


Figure 5.11: Dynamic relaxation spectrum for $N_K = 60$ and $\beta = 20$ obtained with the IEN model. G' is several orders of magnitudes larger than G'' , the shape of G' can be seen in the inset. The BSW parameters are listed in table 5.2.

the shape of the curve. To compensate for this the inset shows a blow up of G' which reveals the three frequency regimes.

Experimental observations of stoichiometrically imbalanced networks shows that G'' and G' are of the same order of magnitude at intermediate frequencies [22, 33], hence, the DSM suggests that energy dissipation is largely a result of dangling ends and soluble structures. It is also expected that such structures will diminish G_0/G_N^0 further since the number of trapped entanglements will decrease.

5.3.3 Entangled Network with Dangling Strands

Our motivation is to capture qualitatively the trends of experimental data at time scales slower than glassy modes. An example of experimental data is shown in figure 5.12 for a polypropylene oxide (PPO) network. The entanglement plateau is not observed. However, assuming it is equal to the entanglement plateau for the linear PPO melt, which is reported by Fetters *et al.* [1] to be 700 kPa, we find that $G_0/G_N^0 \simeq 0.0086$, hence we observe $\sim 99\%$ relaxation from G_N^0 to G_0 .

We simulate network strands and dangling strands with the same parameters used for the results in figure 5.6, *i.e.*, $N_K = 60$, $\beta = 20$ and $w_{DS} = 0.60$. The Green-Kubo results from these simulations are shown in figure 5.13 together with the corresponding G_{IEN} obtained in the previous section. It is observed

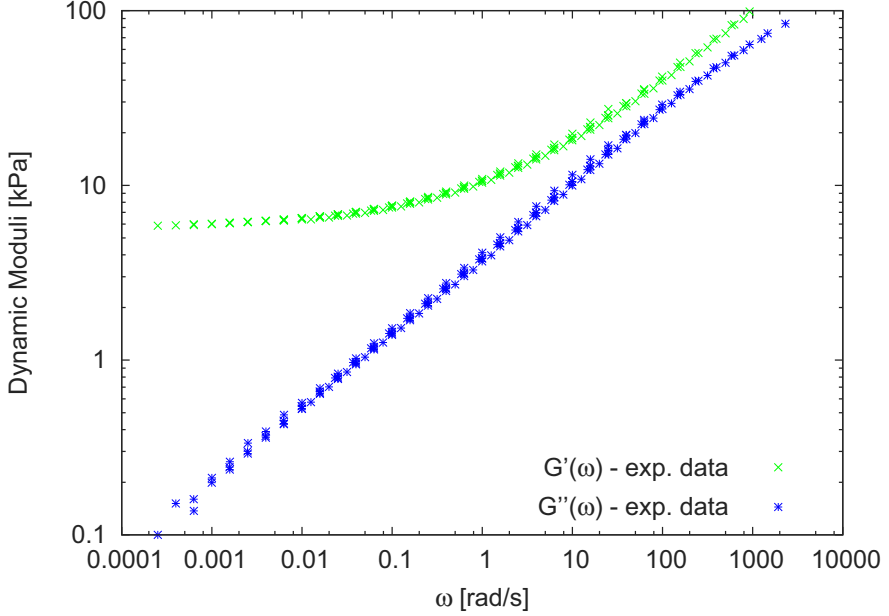


Figure 5.12: G' and G'' obtained from small amplitude oscillatory shear experiments with a polypropylene oxide (PPO) network. We assume that the entanglement plateau, G_N^0 , is equal to 700 kPa, which is for the pure PPO melt [1].

that the amount of relaxation is increased significantly when adding dangling strands, as expected. A comparison of G_{IEN} and G_{NS} clearly shows the CD effect on the network strands, namely that G_0 is reached at a much longer time scale and that it has been reduced. Additionally we find that the presence of dangling strands diminishes G_N^0 . The reason for this is that the free energy of the free end segments is zero, and the analytical expression for G_N^0 is now

$$\begin{aligned} \frac{G_N^0}{\rho RT/M_K} &= \frac{w_{\text{NS}}}{N_K^{\text{N}}} \langle Z_{\text{ENS}} \rangle_{\text{eq}} + \frac{w_{\text{DS}}}{N_K^{\text{D}}} (\langle Z_{\text{EDS}} \rangle_{\text{eq}} - 1) \\ &= \frac{w_{\text{NS}}}{N_K^{\text{N}}} \frac{N_K^{\text{N}} + \beta}{\beta + 1} + \frac{w_{\text{DS}}}{N_K^{\text{D}}} \left(\frac{N_K^{\text{D}} + \beta}{\beta + 1} - 1 \right) \end{aligned} \quad (5.27)$$

$\langle Z_{\text{ENS}} \rangle_{\text{eq}}$ and $\langle Z_{\text{EDS}} \rangle_{\text{eq}}$ are the average number of entangled strands for the network and dangling strands, respectively, while N_K^{N} and N_K^{D} are the total number of Kuhn steps in the network strands and dangling strands respectively. The horizontal dashed line in figure 5.13 is an analytic estimate of the plateau modulus, $G_{0,\text{NS}}$. It is obtained from equation 5.26, where the average number of entanglements have been replaced with the average number of trapped entanglements, Z_{T} :

$$\frac{G_{0,\text{NS}}}{\rho RT/M} = 0.74 Z_{\text{T}} + 1, \quad (5.28)$$

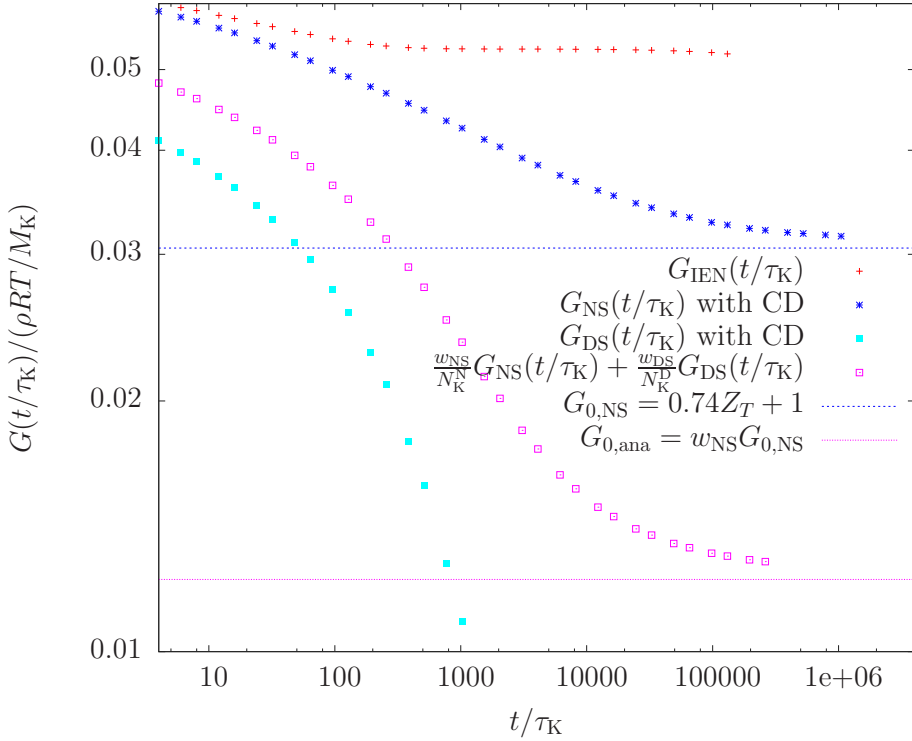


Figure 5.13: Green-Kubo simulation results obtained with both model applications. $N_K^N = N_K^D = 60$, $\beta = 20$ and $w_{DS} = 0.6$.

where Z_T is defined as

$$Z_T = w_{NS}(\langle Z_{ENS} \rangle_{eq} - 1) \quad (5.29)$$

The solid horizontal line in figure 5.13 represents the estimated analytic plateau modulus, $G_{0,ana}$, of the network with dangling strands, which is given by

$$\frac{G_{0,ana}}{\rho RT/M} = w_{NS} \frac{G_{0,NS}}{\rho RT/M} = w_{NS}(0.74 Z_T + 1). \quad (5.30)$$

We observe that equations 5.28 and 5.30 give good estimates for $G_{0,NS}$ and $G_{0,ana}$, which suggests that G_0 is a function of trapped entanglements only.

As for the IEN we convert $G(t)$ into the frequency domain. We do this by converting G_{NS} and G_{DS} individually, where for the dangling strands we set G_0 equal to zero in equation 5.24. The resulting parameters are listed in Tables 5.3 and 5.4. From figure 5.14 we see a relaxation of $\sim 77\%$ until the plateau modulus is reached. Figure 5.14 shows the G^* result, and it is seen that G' has decreased significantly compared to G'' , since they are now of the same order of magnitude at the intermediate frequency regime.

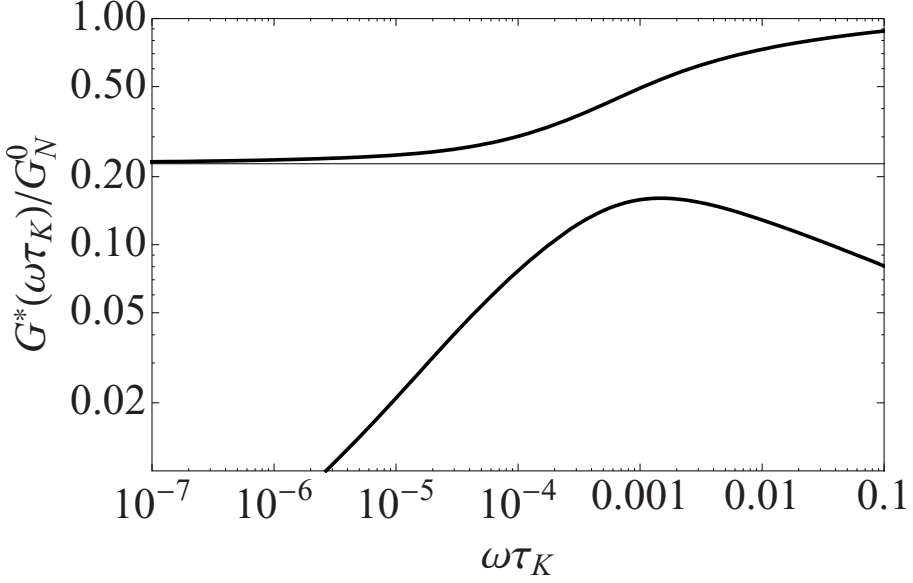


Figure 5.14: G^* result for $N_K^N = N_K^D = 60$, $\beta = 20$ and $w_{DS} = 0.6$. The BSW parameters are listed in tables 5.3 and 5.4. The black horizontal line is $G_{0,ana} = w_{NS}G_{0,NS}$, where $G_{0,NS}$ is obtained from equation 5.28.

Table 5.3: BSW parameters for EDS, $N_K^N = 60$ for the network strands

N_K^D	β	w_{DS}	τ_0	α_1	τ_1	α_2	τ_2
60	20	0.60	0.1 ± 0.9	0.3 ± 0.1	1200 ± 500	-0.9 ± 0.3	$4 \cdot 10^4 \pm 9 \cdot 10^4$
60	20	0.83	0 ± 1	0.3 ± 0.1	1000 ± 500	-1.0 ± 0.5	$2 \cdot 10^4 \pm 6 \cdot 10^4$
60	10	0.83	0.1 ± 0.4	0.17 ± 0.05	3000 ± 1000	-0.8 ± 0.2	$1 \cdot 10^5 \pm 2 \cdot 10^5$
120	10	0.83	0.1 ± 0.2	0.14 ± 0.02	16000 ± 6000	-0.36 ± 0.07	$3 \cdot 10^6 \pm 1 \cdot 10^6$
60	20	0.90	0.1 ± 0.9	0.3 ± 0.1	1000 ± 500	-1.0 ± 0.5	$2 \cdot 10^4 \pm 5 \cdot 10^4$

Table 5.4: BSW parameters for ENS, $N_K^N = 60$ for the network strands

N_K^D	β	w_{DS}	τ_0	α_1	τ_1	α_2	$G_{0,ENS}$
60	20	0.60	1 ± 2	0.04 ± 0.07	5000 ± 4000	-0.44 ± 0.07	1.84 ± 0.04
60	20	0.83	0.3 ± 0.6	0.07 ± 0.05	12000 ± 8000	-0.7 ± 0.2	1.22 ± 0.03
60	10	0.83	0.2 ± 0.3	0.07 ± 0.03	12000 ± 6000	-0.30 ± 0.02	1.44 ± 0.05
120	10	0.83	0.1 ± 0.2	0.07 ± 0.02	30000 ± 20000	-0.126 ± 0.006	1.4 ± 0.1
60	20	0.90	0.3 ± 0.7	0.09 ± 0.05	7000 ± 4000	-0.52 ± 0.06	1.09 ± 0.03

In our recent experimental results the weight fraction of network strands is estimated to be lower than 0.4. We estimate w_{NS} for the experimental data shown in figure 5.12 from a recursive method developed by Macosko and Miller [25, 26]. The methodology is: Let the cross-linking process proceed to a given extent of reaction, p . Then pick a cross-link x at random and let F_x be the event that this cross-linker leads to a finite chain, *i.e.*, x is either unreacted or connected to a dangling structure. The method is based on Flory's [27] three simplifying assumptions:

1. All functional groups of the same type are equally reactive
2. All groups react independently of each other
3. No intra-molecular reactions occur in finite species

From this it is possible to derive the probability of x being connected to a finite chain:

$$P(F_x) = pP(F_x)^{f-1} + (1 - p), \quad (5.31)$$

where f is the functionality of the cross-linker. The second term is a probability that the structure is a dangling end. The fraction of network strands is thus,

$$w_{\text{NS}} = (1 - P(F_x))^2. \quad (5.32)$$

For this derivation it has been assumed that the polymer is end-linked and added in excess, and it reacts exclusively with reactive cross-linker sites. More details about the derivation can be found in references [25, 26]. $p = 0.6$ and $f = 3.2$ for the experimental data shown in figure 5.12, and from that we get $w_{\text{NS}} \cong 0.17$.

Due to lack of experimental G^* data for a pure PPO melt N_K and β are based on polyethylene oxide (PEO) Kuhn parameters, *i.e.*, the length of a Kuhn step, a_K , for a PPO chain is assumed to be the same as for a PEO chain [91]. The bond length is also based on a PEO chain for which the C-C and C-O bond lengths and bond angles are obtained from Takahashi *et al.* [92]

$$\begin{aligned} l_{\text{O-C}} &= 1.43 \text{ \AA} & l_{\text{C-C}} &= 1.54 \text{ \AA} \\ \theta_{\text{C-O-C}} &= 112^\circ & \theta_{\text{O-C-C}} &= 112^\circ. \end{aligned}$$

Both the bond lengths and the bond angles are used to calculate the C-C-O monomer length, l_0 . The molecular weight of a Kuhn step is given by $M_K = a_K/l_0 \cdot M_0$, where M_0 is the monomer molecular weight. Finally the number of Kuhn steps is given by the ratio between the polymer molecular weight, M , and M_K . All parameters are listed in Table 5.5.

Table 5.5: Kuhn parameters for the PEO chain. The monomer molecular weight, M_0 , is for a PPO chain.

Parameter	a_k	l_0	M_0	M_k	N_k
Value	11 \AA	3.7 \AA	56 Da	166.5 Da	60

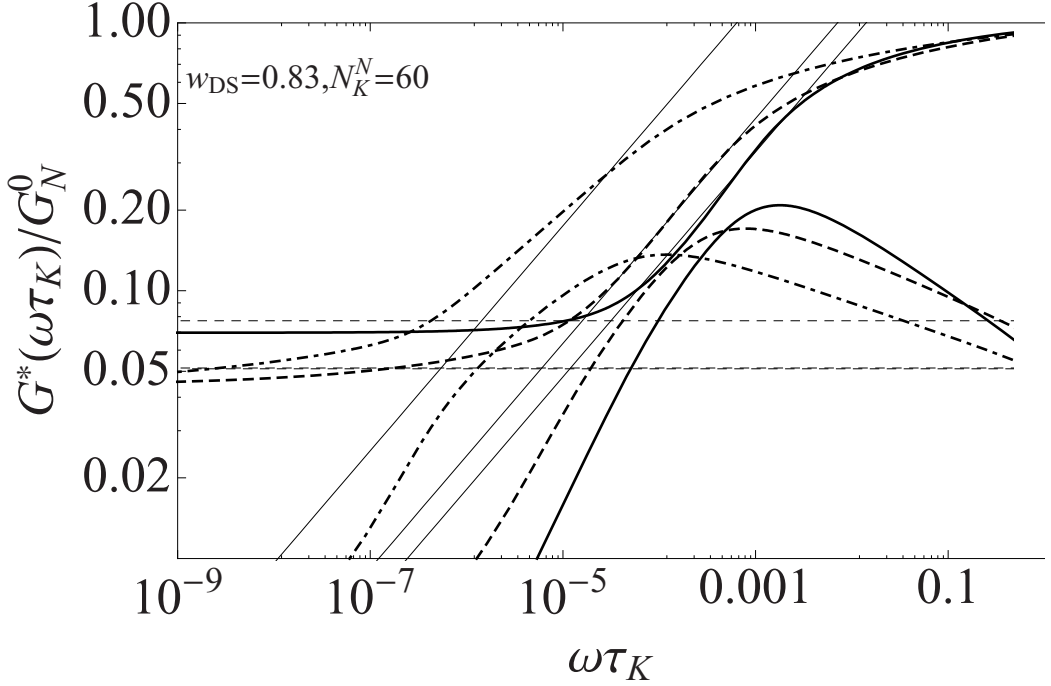


Figure 5.15: G^* results obtained for $w_{DS} = 0.83$. The solid curves are obtained for $\beta = 20$ and $N_K^N = N_K^D = 60$, the dashed for $\beta = 10$ and $N_K^N = N_K^D = 60$, and the dotdashed are for $\beta = 10$, $N_K^N = 60$ and $N_K^D = 120$. The BSW parameters are listed in tables 5.3 and 5.4. The thin black lines are representing the slope of G'' of the experimental data shown in figure 5.12 while the dashed horizontal lines represent the analytical estimation of the plateau.

$\beta = 20$ is calculated from equation 5.4 with the plateau modulus ($G_N^0 = 700$ kPa) and density ($\rho = 1$ g/cm³) reported by Fetters *et al.* [1] for PPO melts. $N_K = 60$ is obtained for $M = 10$ kDa.

The simulated result obtained with $w_{NS} = 0.17$ and $N_K^N = N_K^D = 60$ and $\beta = 20$ is shown with solid black curves in figure 5.15. The G' curve has the same characteristic behavior as experimental data, and we see that the slope at intermediate frequencies is almost the same, which is illustrated with the thin black line. In spite of this very good prediction of the slope, we are overpredicting G_0/G_N^0 , which is equal to 0.070 ± 0.002 and thus, about a decade too high. This overprediction might be reasonable, given the uncertainties in our estimates of N_K , β and G_N^0 .

Considering G'' , we see that this is only parallel to G' in a short frequency window, and we thus do not capture the characteristic power-law behavior of G'' at the intermediate and low frequencies, as seen in experiments.

To understand the reason for the discrepancies between the theory and experimental data, we must consider a number of assumptions, which are listed

below:

Kuhn parameters The estimated value of β might be off, due to the assumption that the PPO chain can be described by PEO Kuhn parameters.

Linear strands All the dangling strands are treated as linear and monodisperse strands. This is a crude simplification since dangling structures can have a wide distribution of architectures, ranging from hyper-branched structures to linears.

Soluble structures Besides dangling structures there are soluble structures present, which have not yet been included. So far the weight fraction of solubles has been included in w_{DS} .

Weight fractions The weight fraction of network strands is estimated from the percolation theory proposed by Macosko and Miller [25, 26]. This theory is very simplified and does not account for intra-molecular reactions, looping or other network “imperfections”. We expect that w_{NS} , in reality, should be lower than the one estimated by the percolation theory.

Influence of β

If the value of β is too high, we are simulating a chain that is too stiff, *i.e.*, the average number of entanglements is too low. We know from the IEN simulations that G_0 relative to G_N^0 will decrease as the number of entanglements increases. The result obtained with $\beta = 10$ and $N_K = 60$ is shown in figure 5.15 with dashed curves. As expected we see that G_0/G_N^0 is reduced. However, we still do not capture the characteristic behavior of G'' , which must be due to some other dynamics not yet included.

Monodisperse Linear Dangling Strands

Another reason why the prediction of G'' is off, could be that we simulate monodisperse linear dangling strands. We expect that some of the dangling structures are branched, which would change the dynamics significantly. We mimic branched dangling strands using linear strands that are twice as long, *i.e.*, $N_K^D = 120$. The result obtained with $\beta = 10$ is shown with dotdashed curves in figure 5.15. We observe a very significant change in the shape of G'' , where the slope at the intermediate frequency region has decreased, hereafter it increases again when G' approaches a plateau. A comparison of the theoretical results shown in figure 5.15, suggests that a power-law behavior of G'' is an effect of a distribution of relaxation times, which seemingly can be achieved by modeling a polydisperse ensemble of dangling strands. We also observe that the slope of G' has decreased compared to the experimental slope, while the plateau is unchanged compared to the monodisperse system.

Soluble Structures

If we normalize the experimental data in figure 5.12 with $G_N^0 = 700$ kPa, we find that the experimental data lie about one decade below the theoretical results in figure 5.15. We believe that one reason for this is the missing soluble structures in the simulations. These are, in contrast to network strands, able to relax completely, and will therefore reduce the dynamic moduli in a similar way as dangling strands. Addition of soluble structures to the ensemble will also introduce shorter relaxation times than dangling strands and we thus, expect that soluble structures will also contribute to the power-law of G'' .

Influence of w_{NS}

Finally the estimation of w_{NS} is based on an idealized percolation theory, and it is expected that looping and other network “imperfections” will reduce w_{NS} compared to the percolation estimate. To study the effect of the size of w_{NS} we simulate chains with $N_K^{\text{N}} = N_K^{\text{D}} = 60$, $\beta = 20$ and $w_{\text{DS}} = 0.90$. The result is shown in figure 5.16 together with the results for the same N_K values and β , but with $w_{\text{DS}} = 0.83$. It is seen that both G_0 and the slope of G' is largely affected by changes in w_{DS} , while only small changes are observed for G'' .

At a first glance this results seem to be worse compared to experimental data than when $w_{\text{NS}} = 0.17$, however, we found earlier that inclusion of more complicated structures has the opposite effect on the slope of G' , while it does not affect G_0 . Hence, since G_0 is still overpredicted when $w_{\text{NS}} = 0.1$ we need to decrease this fraction further as well as include soluble structures to reach the correct value of G_0 . Additionally we must introduce strands with shorter and longer relaxation times than just a single monodisperse strand, to capture the power law behavior of G'' .

Analytical Estimation of $G_{0,\text{ana}}$

In figures 5.13 to 5.16 we show the analytical estimate of the equilibrium modulus, $G_{0,\text{ana}}$, as horizontal lines. We find that for $\beta = 20$, $N_K = 60$ and $w_{\text{NS}} = 0.60$ that the analytical estimate based on equation 5.28 predict the exact value. In all other cases $G_{0,\text{ana}}$ is slightly overestimated compared to the exact results. The estimate of $G_{0,\text{ana}}$ is only dependent on the average number of trapped entanglements, and is derived from simulation results of ideal entangled networks with the number of trapped entanglements from about 3 and up. The overestimation of $G_{0,\text{ana}}$ is seemingly a consequence of the low value of trapped entanglements, $Z_{\text{T}} \leq 1$, for which we do not expect equation 5.28 to be exact, though it predicts the correct order of magnitude of G_0 .

It is obvious from figures 5.15 and 5.16 that the slope of G' is dependent on both w_{NS} and the structural distribution of the network and that they work in opposite direction, *i.e.*, decreasing w_{NS} increases the slope while a wider distribution of structures will decrease the slope. In the present case the model is overpredicting G_0 since the value of trapped entanglements is too high. Assuming that the analytical expression in equation 5.28 is exact we can estimate w_{NS}

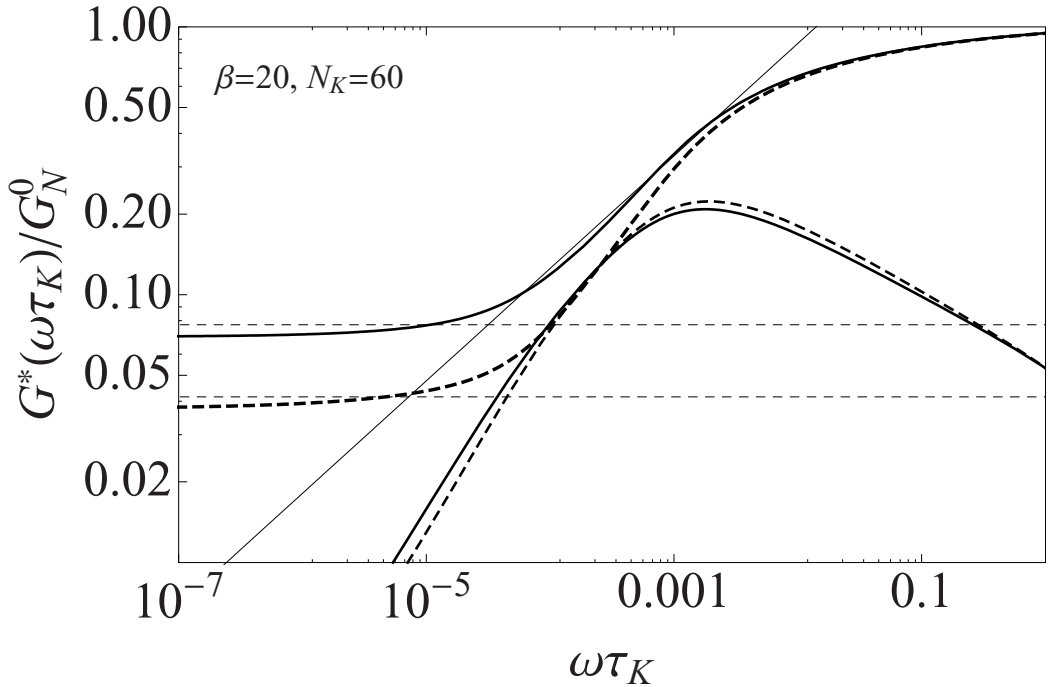


Figure 5.16: G^* results obtained for $w_{\text{DS}} = 0.83$ (solid curves) and $w_{\text{DS}} = 0.90$ (dashed curves). The model parameters are in both cases $\beta = 20$ and $N_K^{\text{N}} = N_K^{\text{D}} = 60$. The thin black line shows the slope of G'' from the experimental data in figure 5.12. The BSW parameters are listed in tables 5.3 and 5.4.

based on the experimental equilibrium plateau. For the experimental data in figure 5.12 we know that $G_0/G_N^0 = 0.0086$, where G_N^0 is for a PPO melt. Hence, if $N_K = 60$ and $\beta = 20$ we get $w_{\text{NS}} = 0.015$, which is much lower than the weight fractions used so far. A simulation with $w_{\text{NS}} = 0.015$ will increase the slope of G' significantly, however, simulations of structures with different relaxation times will have the opposite effect.

5.4 Conclusion

In our attempts to understand the entanglement effect on the dynamic moduli of cross-linked polymeric networks, we have presented two applications of the discrete slip-link model. The first is used to model ideal entangled networks (IEN), from which we derived a linear relation between the plateau modulus and the number of trapped entanglements.

The other application of the model is a combination of entangled network strands and entangled dangling strands. As a starting point we wish to describe experimental data quantitatively, and for simplicity we assumed that all the

dangling strands were monodisperse and linear.

The results suggest that the features of G^* arise completely from the polymer that is non-active. The height of the plateau at high frequencies is just a function of entanglement density plus cross-link density. The low frequency plateau is a linear function of the density of cross-links plus trapped entanglements. Hence, its value is a strong function of the mass fraction of active structures in the network, in agreement with classical theories. Moreover, the power-law region is very sensitive to the details of curing and the types of soluble and dangling structures that are created. The theory used here requires as input these structures, so additional detailed modeling of the curing process is necessary to make quantitative predictions.

Chapter 6

Summarizing chapter

6.1 Concluding Remarks

In order to understand the macroscopic properties of polymeric networks, it is necessary to have some knowledge about the basic features of the network, namely the architecture of the network structures. The fundamental properties are governed by the scaling between the amount of elastically active network strands, the dangling structures and the soluble structures. The amount of the latter two depends strongly on the initial formulation of the networks, that is; the network stoichiometry, the cross-linker functionality and the molecular weight of the polymer. Changing one of these will have a visible impact on the macroscopic properties of the network.

A common measure of these properties is the linear viscoelastic response, which is very characteristic for polymer networks. While polymer melts relax completely by reptation, this is not the case for networks. Here, the storage modulus will level off to a plateau, called the equilibrium modulus at low frequencies, and at intermediate frequencies the storage and loss modulus will be parallel. It is therefore convenient to use a modified version of the gel equation to describe the moduli. The equilibrium modulus is highly dependent on the cross-link density, while the gel stiffness and the relaxation exponent from the gel equation depend on the molecular weight of the polymer, and thus the number of entanglements.

In the aim of retrieving new standards for characterizing the adhesive performance of soft polymeric networks, we have linked the fundamental linear viscoelastic parameters, to the peel performance. The peel force is known to be proportional to the peel-strip dimensions, however, it is possible to make a universal link to the linear viscoelastic data, which relates the peel force to the bulk properties. Two mechanisms important for adhesives are considered, that is; the bonding and the debonding mechanisms. The bonding mechanism is highly dependent on the adhesives' ability to adapt to a given surface. The time scale of bonding is considered slow, and do therefore, correspond to the

low frequency regime for linear viscoelastic measurements, which is characterized by the equilibrium modulus. On the other hand, the debonding is usually a fast process, and thus, related to the high frequency regime in the linear viscoelastic measurements. The loss tangent is a common measure in the adhesive industry, since it scales the viscous (sticky) properties to the elastic. Hence, a combination of the loss tangent at the peel frequency and the equilibrium modulus, includes both bulk properties on the time scale of debonding and bonding. There is a universal behavior between the peel force and low values of the loss tangent, however, as the loss tangent increases, a dependency on the cross-link density is observed. Comparing the peel force at corresponding values of the loss tangent, shows that it increases as the cross-link density decreases. This observation is due to a nonlinear effect, namely strain hardening.

Following the results in chapter 2, we considered nonlinear measurements on the network samples. Due to limitations concerning already existing measuring techniques, a new fixture, called the planar elongation fixture, was designed. The key concern was to make the sticky nature of the samples an advantage, rather than a disadvantage. The resulting experimental design is a fixture, which elongates a specimen shaped as an annulus. In order to measure pure planar elongation, the perimeter of the annulus must remain constant. As an uplifting result, it was found that this can be achieved by adjusting the initial sample geometry. From numerical finite element simulations, it was found that this is a consequence of the near neo-Hookean behavior of the soft networks.

The new fixture is used to measure both steady and reversible large amplitude elongation. Finite element simulations were used to analyze the measurements. The finite element modeling is done within the frame-work of the K-BKZ constitutive equation, where three different nonlinear strain tensors were considered; 1) The modified MSF model, 2) the Modified Lodge model and 3) a new approximation to the Doi-Edwards model, called the DE network model. All three models described the experimental stress-differences well, while significant differences are observed when looking at the cylindrical probe deformation. It was found that the relative magnitude of the two functions, ϕ_1 and ϕ_2 , is important for this deformation. For instance if $\phi_2 = 0$, as for the Lodge model, little deformation is observed, while the MSF model predicts a much too large deformation. As the Lodge model under-predicts the experimental data, it is obvious that ϕ_2 must be non-zero when describing soft polymeric networks, though ϕ_2 must be lower than for the MSF model. The DE network model proved to be an excellent choice, since it captures the magnitude of the cylindrical deformation.

Reversible planar elongation stresses give more information about the elastic material behavior compared to simple steady elongation. It is possible to extract how much work is gained from the sample, upon flow reversal. Obviously, the more elastically active chains present in the samples, the more energy will be stored. The relative amount of work performed by the sample on the external system is near frequency independent, however, it changes significantly with strain, indicating that the stress is time-strain separable. The latter statement is confirmed by finite element simulations with the Lodge and the DE network model, since they are both time-strain separable, and describes the stress data

very well.

Finally a theoretical study based on the discrete slip-link model was introduced. With this we can model monodisperse entangled networks with dangling strands, and predict our experimental data qualitatively. We find, in particular, that the slope of G' at intermediate frequencies is largely influenced by the fraction of network strands, and that the power-law behavior of G'' is due to a wide distribution of relaxation times. Based on ideal entangled network predictions we derived a linear relation between the plateau modulus and the average number of trapped entanglements, which makes it possible to estimate the plateau modulus analytically when dangling strands are present. This analytical expression shows that the equilibrium plateau is largely dominated by the average number of trapped entanglements. The level of the dynamic moduli are in general overpredicted compared to experimental data, however, we ascribe this to the lack of solubles in the ensemble.

6.2 Future Work

During this project we have made an extensive investigation of the mechanical properties of polymer networks. While some questions were answered, others gave rise to new and interesting observations that are not yet fully understood. This section will give an overview of what I believe are important future studies.

Peel and non-Linear Rheology

We expect that the deviation from the universal behavior, observed in chapter 2, as the loss tangent increases, is due to the nonlinear strain behavior of the materials. The cross-link density becomes important, which leads our attention to strain hardening of the material. It could therefore be interesting to investigate how the molecular weight, the functionality and the stoichiometric imbalance affect this. The obvious method to do this, is to use the planar elongation fixture introduced in chapter 3.

The strain hardening nature of a material introduces an interesting observation, that is; as the stress differences increases dramatically in elongation at the point of strain hardening, we only see a modest increase in peel experiments. The reason is, as the word *hardening* indicates, that the materials do become harder, and thus, loses some of the stickiness, which will naturally decrease the resistance to peel.

Obviously, we would like to include the stress-difference in the empirical relation to the peel force. To do so, it is necessary to specify a characteristic strain, where a natural choice could be strain of the material at the peel front.

Monodisperse Network Reactants and Chemistry

To test the universality of the results in chapter 2, it would be favorable to perform a similar analysis, on a different type of network chemistry, for instance poly(dimethyl siloxane) (PDMS) networks. Preferable this should be done with

well defined cross-linkers and monodisperse polymers, which would also be a better model system. The usage of a well defined model system would make a structural analysis and characterization of the networks more exact.

With a better model system, we can extend the analysis of the gel equation parameters from chapter 2. Here it was found that the gel stiffness and the relaxation exponent depends only on the molecular weight of the polymer, and not on the cross-linker functionality. It could be interesting to investigate this dependency further.

Another strength of monodisperse networks is that the cross-link density is easily determined.

The Discrete Slip-link Model

The DSM, as described in chapter 5, can describe the mechanical properties of entangled monodisperse networks with dangling strands. However, as the dangling strands often consist of a wide distribution of branched structures it is of interest to model dangling strands as, for instance, monodisperse branches, or bi-disperse linears or maybe a combination of the two. By doing so we will introduce a distribution of relaxation times, which should have an effect on the shape of G'' .

Additionally we should include soluble structures. Such structures can relax in both ends, and is therefore expected to reduce the dynamic moduli over the entire frequency window. As for the dangling strands, it is interesting to see the effect of modeling branched solubles or bi-disperse solubles. This should also have an effect on the shape of G'' , since more relaxation patterns are added to the system.

Structural Analysis

To further develop the theoretical analysis of polymer networks, it is an advantage to have a good statistical description of the networks. Even though the percolation theory described by Macosko and Miller [25, 26] seemingly predict the weight fractions of network, dangling and soluble structures accurately, it does not reveal information about the branched structures. This can be obtained from the seniority distribution, however, this is also based on the same idealized assumptions as the percolation theory.

To account for looping and intra-molecular reactions it can therefore be necessary to consider another statistical approach. One method is to use the Bond fluctuation Model (BFM), which has already been used extensively for networks [93–96]. The BFM can be used to prepare model networks on a lattice with a random walk configuration. Such lattice configuration can give insight into the looping probability and the probability of having unreacted sites.

Joint Author Declarations

*Technical University of Denmark**Research and Innovation, PhD programme**April 2009***Joint author statement**

If a thesis contains articles made in collaboration with other researchers, a joint author statement about the PhD-student's part of the article shall be made by each of the co-authors, cf. article 12, section 4 of the Ministerial Order No. 18 February 2008 about the PhD degree

Title of the article: Linear Rheology of Cross-linked Polypropylene Oxide Oxide as a Pressure Sensitive Adhesives

Author(s): Mette Krog Jensen, Ole Hassager, Anne Ladegaards Skov, Anders Bach

Journal: Int. J. of Adhesion & Adhesives

PhD-student: Mette Krog Jensen CPR-no.: 120980-2208

Signature of the PhD-student: _____ Date: 9/9-09

Co-author: Anne Skov Signature: A Skov

Description of each author's contribution to the above-mentioned article:

As co-author of the above article I hereby accept that the first author includes it is a chapter in her Ph.D. Thesis entitled "Linear Rheology of Cross-linked Polypropylene Oxide Oxide as a Pressure Sensitive Adhesives". I verify that the first author carried out experimental work and data treatment.

I contributed to the article by supervising the first author and engaging in discussion about the results and the manuscript. The article was jointly written by Mette Krog Jensen, Anders Bach and me.

Joint author statements shall be delivered to the **PhD administration** together with the PhD thesis.

*Technical University of Denmark**Research and Innovation, PhD programme**April 2009*

Joint author statement

If a thesis contains articles made in collaboration with other researchers, a joint author statement about the PhD-student's part of the article shall be made by each of the co-authors, cf. article 12, section 4 of the Ministerial Order No. 18 February 2008 about the PhD degree

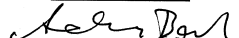
Title of the article: Linear Rheology of Cross-linked Polypropylene Oxide Oxide as a Pressure Sensitive Adhesives

Author(s): Mette Krog Jensen, Ole Hassager, Anne Ladegaards Skov, Anders Bach

Journal: Int. J. of Adhesion & Adhesives

PhD-student: Mette Krog Jensen CPR-no.: 120980-2208

Signature of the PhD-student: _____ Date: _____

Co-author: Anders Bach Signature: 

Description of each author's contribution to the above-mentioned article:

As co-author of the above article I hereby accept that the first author includes it is a chapter in her Ph.D. Thesis entitled "Linear Rheology of Cross-linked Polypropylene Oxide Oxide as a Pressure Sensitive Adhesives". I verify that the first author carried out experimental work and data treatment.

I contributed to the article by supervising the experimental work carried out by the first author and engaging in discussion about the results and the manuscript. The article was jointly written by Mette Krog Jensen, Anne Ladegaard Skov and me.

Joint author statements shall be delivered to the **PhD administration** together with the PhD thesis.

*Technical University of Denmark**Research and Innovation, PhD programme**April 2009***Joint author statement**

If a thesis contains articles made in collaboration with other researchers, a joint author statement about the PhD-student's part of the article shall be made by each of the co-authors, cf. article 12, section 4 of the Ministerial Order No. 18 February 2008 about the PhD degree

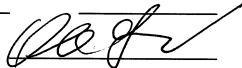
Title of the article: Linear Rheology of Cross-linked Polypropylene Oxide Oxide as a Pressure Sensitive Adhesives

Author(s): Mette Krog Jensen, Ole Hassager, Anne Ladegaards Skov, Anders Bach

Journal: Int. J. of Adhesion & Adhesives

PhD-student: Mette Krog Jensen CPR- 120980-2208
no.: _____

Signature of the PhD-student: _____ Date: _____

Co-author: Ole Hassager Signature: 

Description of each author's contribution to the above-mentioned article:

As co-author of the above article I hereby accept that the first author includes it is a chapter in her Ph.D. Thesis entitled "Linear Rheology of Cross-linked Polypropylene Oxide Oxide as a Pressure Sensitive Adhesives". I verify that the first author carried out experimental work and data treatment.

I contributed to the article by supervising the first author and engaging in discussion about the results and the manuscript. The article was jointly written by Mette Krog Jensen, Anne Ladegaard Skov and Anders Bach.

Joint author statements shall be delivered to the **PhD administration** together with the PhD thesis.

Technical University of Denmark

Research and Innovation, PhD programme

April 2009

Joint author statement

If a thesis contains articles made in collaboration with other researchers, a joint author statement about the PhD-student's part of the article shall be made by each of the co-authors, cf. article 12, section 4 of the Ministerial Order No. 18 February 2008 about the PhD degree


Title of the article: Planar Elongation of Soft Polymeric Networks

Author(s): Mette Krog Jensen, Ole Hassager, Henrik Koblitz Rasmussen, Anne Ladegaards Skov, Anders Bach

Journal: Rheol. Acta

PhD-student: Mette Krog Jensen CPR-no.: 120980-2208

Signature of the PhD-student: _____ Date: _____

Co-author: HENRIK K. RASMUSSEN Signature: 

Description of each author's contribution to the above-mentioned article:

As co-author of the above article I hereby accept that the first author includes it is a chapter in her Ph.D. Thesis entitled "Rheology of Cross-linked Polymer Networks". I verify that the first author carried out experimental work and post-processing of experiments.

I contributed to the article by supervising the experimental work carried out by the first author and engaging in discussion about the results and the manuscript. Further I performed all the numerical simulations. The article was jointly written by Mette Krog Jensen, Ole Hassager, Anne Ladegaard Skov and me.

Joint author statements shall be delivered to the **PhD administration** together with the PhD thesis.

*Technical University of Denmark**Research and Innovation, PhD programme**April 2009***Joint author statement**

If a thesis contains articles made in collaboration with other researchers, a joint author statement about the PhD-student's part of the article shall be made by each of the co-authors, cf. article 12, section 4 of the Ministerial Order No. 18 February 2008 about the PhD degree

Title of the article: Planar Elongation of Soft Polymeric Networks

Author(s): Mette Krog Jensen, Ole Hassager, Henrik Koblitz Rasmussen, Anne Ladegaards Skov, Anders Bach

Journal: Rheol. Acta

PhD-student: Mette Krog Jensen CPR-no.: 120980-2208

Signature of the PhD-student: _____ Date: 9/9-09

Co-author: Anne Skov Signature: A Skov

Description of each author's contribution to the above-mentioned article:

As co-author of the above article I hereby accept that the first author includes it is a chapter in her Ph.D. Thesis entitled "Rheology of Cross-linked Polymer Networks". I verify that the first author carried out experimental work and post-processing of experiments.

I contributed to the article by supervising the first author and engaging in discussion about the results and the manuscript. The article was jointly written by Mette Krog Jensen, Ole Hassager, Henrik Koblitz Rasmussen and me.

Joint author statements shall be delivered to the **PhD administration** together with the PhD thesis.

*Technical University of Denmark**Research and Innovation, PhD programme**April 2009*

Joint author statement

If a thesis contains articles made in collaboration with other researchers, a joint author statement about the PhD-student's part of the article shall be made by each of the co-authors, cf. article 12, section 4 of the Ministerial Order No. 18 February 2008 about the PhD degree

Title of the article: Planar Elongation of Soft Polymeric Networks

Author(s): Mette Krog Jensen, Ole Hassager, Henrik Koblitz Rasmussen, Anne Ladegaards Skov, Anders Bach

Journal: Rheol. Acta

PhD-student: Mette Krog Jensen CPR- 120980-2208
no.: _____

Signature of the _____
PhD-student: _____ Date: _____

Co-author: Anders Bech . Signature: Anders Bech

Description of each author's contribution to the above-mentioned article:

As co-author of the above article I hereby accept that the first author includes it is a chapter in her Ph.D. Thesis entitled "Rheology of Cross-linked Polymer Networks". I verify that the first author carried out experimental work and post-processing of experiments.

I contributed to the article by engaging in discussion about the results and the manuscript. The article was jointly written by Mette Krog Jensen, Ole Hassager, Henrik Koblitz Rasmussen and Anne Ladegaard Skov.

Joint author statements shall be delivered to the **PhD administration** together with the PhD thesis.

Technical University of Denmark

Research and Innovation, PhD programme

April 2009

Joint author statement

If a thesis contains articles made in collaboration with other researchers, a joint author statement about the PhD-student's part of the article shall be made by each of the co-authors, cf. article 12, section 4 of the Ministerial Order No. 18 February 2008 about the PhD degree

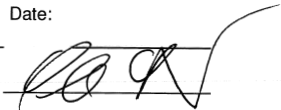
Title of the article: Planar Elongation of Soft Polymeric Networks

Author(s): Mette Krog Jensen, Ole Hassager, Henrik Koblitz Rasmussen, Anne Ladegaards Skov, Anders Bach

Journal: Rheol. Acta

PhD-student: Mette Krog Jensen CPR- no.: 120980-2208

Signature of the PhD-student: _____ Date: _____

Co-author: Ole Hassager Signature: 

Description of each author's contribution to the above-mentioned article:

As co-author of the above article I hereby accept that the first author includes it as a chapter in her Ph.D. Thesis entitled "Rheology of Cross-linked Polymer Networks". I verify that the first author carried out experimental work and post-processing of experiments.

I contributed to the article by supervising the first author and engaging in discussion about the results and the manuscript. The article was jointly written by Mette Krog Jensen, Henrik Koblitz Rasmussen, Anne Ladegaard Skov and me.

Joint author statements shall be delivered to the **PhD administration** together with the PhD thesis.

Bibliography

- [1] L.J. Fetters, D.J. Lohse, D. Richter, T.A. Witten, and A. Zirkel. Connection between Polymer Molecular Weight, Density, Chain Dimensions, and Melt Viscoelastic Properties. *Macromolecules*, 27(17):4639–4647, 1994.
- [2] C. Creton. Pressure-sensitive adhesives: An introductory course. *Mrs. Bulletin*, 28(6):434, 2003.
- [3] S. F. Christensen, H. Everland, O. Hassager, and K. Almdahl. Observations of peeling of a polyisobutylene-based pressure-sensitive adhesive. *Int. J. of Adhesion and Adhesives*, 18:131, 1998.
- [4] Zongming Gao, Julia Schulze Nahrup, James E. Mark, and Adel Sakr. Poly(dimethylsiloxane) coatings for controlled drug release. i. preparation and characterization of pharmaceutically acceptable materials. *Journal of Applied Polymer Science*, 90(3):658–666, 2003.
- [5] RB Noone, RM Goldwyn, M McGrath, S Spear, and GRD Evans. 50th anniversary plastic surgery research council panel on the future of academic plastic surgery. *Plastic and Reconstructive Surgery*, 120(6):1709, 2007.
- [6] E.M. Valls and C.W. Macosko. The effect of network structure in the equation of rubber elasticity. *Rubber Chem. Technol*, 49:1232–1237, 1976.
- [7] S. Wang and J. E. Mark. Unimodal and bimodal networks of poly(dimethyl siloxane) in pure shear. *J. Polymer Science: Part B: Polymer Physics*, 30:801–807, 1992.
- [8] K. Urayama, T. Kawamura, and S. Kohjiya. Structure-mechanical property correlations of model siloxane elastomers with controlled network topology. *Polymer*, 50(2):347–356, January 2009.
- [9] D Satas. Pressure sensitive adhesives and adhesive products in the united states. *Handbook of pressure sensitive adhesives*, pages 2–23.
- [10] D. J. Yarusso. Quantifying the relationship between peel and rheology for pressure sensitive adhesives. *J. of Adhesion*, 70:199, 1999.

- [11] J Renvoise, D Burlot, G Marin, and C Derail. Peeling of psas on viscoelastic substrates: A failure criterion. *The Journal of Adhesion*, 83(4):403–416, 2007.
- [12] J Du, DD Lindeman, and DJ Yarusso. Modeling the peel performance of pressure-sensitive adhesives. *The Journal of Adhesion*, 80(7):601–612, 2004.
- [13] D. H. Kaelble. Theory and analysis of peel adhesion: Mechanisms and mechanics. *Transactions of the Society of Rheology*. **III**, III:161–180, 1959.
- [14] D. H. Kaelble. Theory and analysis of peel adhesion: Rate-temperature dependence of viscoelastic interlayers. *J. of Colloid Science*, 19:413, 1964.
- [15] D. H. Kaelble. Peel adhesion: Micro-fracture mechanics of interfacial unbonding of polymers. *Transactions of the Society of Rheology*, 9(2):135, 1965.
- [16] D. H. Kaelble. Peel adhesion: Rate dependence of micro fracture processes. *J. of Adhesion*, 1:124, 1969.
- [17] A. N. Gent. Adhesion and strength of viscoelastic solids. is there a relationship between adhesion and bulk properties? *Langmuir*, 12:4492, 1996.
- [18] A. N. Gent, E. G. Kim, and P Ye. Autohesion of cross-linked polyethylene. *J. of Polymer Science*, 35(4):615, 1997.
- [19] Didi Derks, Anke Lindner, Costantino Creton, and Daniel Bonn. Cohesive failure of thin layers of soft model adhesives under tension. *J. Appl. Phys.*, 93(3):1557–1566, February 2003.
- [20] M. Rubinstein and R. Colby. *Polymer Physics*. Oxford University Press, 2006.
- [21] PG De Gennes. Reptation of a polymer chain in the presence of fixed obstacles. *The Journal of Chemical Physics*, 55:572, 1971.
- [22] A. Marcelo, M.A. Villar, and E.M Valls. Influence of pendant chains on mechanical properties of model poly(dimethylsiloxane) networks. 2. viscoelastic properties. *Macromolecules*, 29:4081–4089, 1996.
- [23] A. L. Larsen, K. Hansen, P. Sommer-Larsen, O. Hassager, A. Bach, S. Ndoni, and M. Jørgensen. Elastic properties of nonstoichiometric reacted PDMS networks. *Macromolecules*, 36:10063, 2003.
- [24] A. L. Larsen, P. Sommer-Larsen, and O. Hassager. Some experimental results for the end-linked polydimethylsiloxane network system. *e-Polymers*, 050(050):1–18, 2004.
- [25] C. W. Macosko and D. R. Miller. A new derivation of average molecular weights of nonlinear polymers. *Macromolecules*, 9(2):199, 1976.

- [26] D. R. Miller and C. W. Macosko. A new derivation of post gel properties of network polymers. *Macromolecules*, 9(2):206, 1976.
- [27] P.J. Flory. Molecular size distribution in three dimensional polymers. III. Tetrafunctional branching units. *Journal of the American Chemical Society*, 63(11):3096–3100, 1941.
- [28] P.J. Flory. *Principles of polymer chemistry*. Cornell Univ Pr, 1953.
- [29] D.J. Read and T.C.B. McLeish. Molecular rheology and statistics of long chain branched metallocene-catalyzed polyolefins. *Macromolecules*, 34(6):1928–1945, 2001.
- [30] J.E. Mark. Elastic properties of model polymer networks. *Pure & Applied Chemistry*, 53:1495–1503, 1981.
- [31] EM Valls, EJ Rost, and CW Macosko. Small-strain modulus of model trifunctional polydimethylsiloxane networks. *Rubber chemistry and technology*, 57(1):55–62, 1984.
- [32] H. W. H. Yang. *J. of Applied Polymer Science*, 55:645, 1995.
- [33] M.A. Villar, M.A. Bibbó, and E.M Valls. Influence of pendant chains on mechanical properties of model poly(dimethylsiloxane) networks. 1. analysis of the molecular structure of the network. *Macromolecules*, 29:4072–4080, 1996.
- [34] Michael Rubinstein and Sergei Panyukov. Elasticity of polymer networks. *Macromolecules*, 35(17):6670–6686, 2002.
- [35] K. Urayama. Network topology–mechanical properties relationships of model elastomers. *Polymer Journal*, (8):669–678, 2008.
- [36] S. F. Christensen and G. H. McKinley. Rheological modelling of the peeling of pressure-sensitive adhesives and other elastomers. *Int. J. of Adhesion and Adhesives*, 18:333, 1998.
- [37] R. B. Bird, R. C. Armstrong, and O. Hassager. *Dynamics of polymeric liquids, Vol 1: Fluid Dynamics*. Wiley Interscience, New York, 1987.
- [38] F.A. Morrison. *Understanding rheology*. Oxford University Press, USA, 2001.
- [39] C.W. Macosko and G.S. Benjamin. Modulus of three and four functional poly(dimethylsiloxane) networks. *Pure and Applied Chemistry*, 53(8):1505–1518, 1981.
- [40] Suman K. Patel, Shawn Malone, Claude Cohen, Jeffrey R. Gillmor, and Ralph H. Colby. Elastic modulus and equilibrium swelling of poly(dimethylsiloxane) networks. *Macromolecules*, 25(20):5241–5251, September 1992.

- [41] Kenji Urayama, Keisuke Yokoyama, and Shinzo Kohjiya. Viscoelastic relaxation of guest linear poly(dimethylsiloxane) in end-linked poly(dimethylsiloxane) networks. *Macromolecules*, 34(13):4513–4518, June 2001.
- [42] J. L. Sullivan, J. E. Mark, P. G. Hampton, Jr., and R. E. Cohen. Model networks of end-linked polydimethylsiloxane chains. ii. viscoelastic losses. *J. Chem. Phys.*, 68(4):2010–2012, February 1978.
- [43] Kenji Urayama, Takanobu Kawamura, and Shinzo Kohjiya. Elastic modulus and equilibrium swelling of networks crosslinked by end-linking oligodimethylsiloxane at solution state. *J. Chem. Phys.*, 105(11):4833–4840, September 1996.
- [44] C. Rouf-George, J. P. Munch, G. Beinert, F. Isel, A. Pouchelon, J. F. Palierne, F. Bou, and J. Bastide. About “defects” in networks made by end-linking. *Polymer Gels and Networks*, 4(5-6):435–450, 1996.
- [45] H. H. Winter and F. Chambon. Analysis of linear viscoelasticity of a cross-linking polymer at the gel point. *J. of Rheology*, 30(2):367, 1986.
- [46] F. Chambon and H. H. Winter. Linear viscoelasticity at the gel point of a cross-linking pdms with imbalanced stoichiometry. *J. of Rheology*, 31(8):683, 1987.
- [47] J. Meissner and J. Hostettler. A new elongational rheometer for polymer melts and other highly viscoelastic liquids. *Rheologica Acta*, 33(1):1–21, 1994.
- [48] T. Sridhar, V. Tirtaatmadja, DA Nguyen, and RK Gupta. Measurement of extensional viscosity of polymer solutions. *Journal of non-newtonian fluid mechanics*, 40(3):271–280, 1991.
- [49] M.L. Sentmanat. Miniature universal testing platform: from extensional melt rheology to solid-state deformation behavior. *Rheologica Acta*, 43(6):657–669, 2004.
- [50] J. Meissner. Development of a universal extensional rheometer for the uniaxial extension of polymer melts. *Journal of Rheology*, 16:405, 1972.
- [51] Anders Bach, Henrik Koblitz Rasmussen, and Ole Hassager. Extensional viscosity for polymer melts measured in the filament stretching rheometer. *J. Rheol.*, 47(2):429–441, March 2003.
- [52] Jens Kromann Nielsen and Ole Hassager. Observing the chain stretch transition in a highly entangled polyisoprene melt using transient extensional rheometry. Accepted for publikation in J. Rheol., DOI: 10.1122/1.3208073, November/December 2009.

- [53] Kaijia Yu, Josè Manuel Romàn Marín, Henrik Koblitz Rasmussen, and Ole Hassager. 3d modeling of dual wind-up extensional rheometers. Accepted for publication in *Journal of non-Newtonian Fluid Mechanics*, August 2009.
- [54] Jens Kromann Nielsen and Henrik Koblitz Rasmussen. Reversed extension flow. *Journal of Non-Newtonian Fluid Mechanics*, 155(1-2):15–19, November 2008.
- [55] A.B. Bejenariu, H.K. Rasmussen, A.L. Skov, and O. Hassager. Large Amplitude Oscillatory Extension of Soft Polymeric Networks. Submitted for publication in *Rheologica Acta*, August 2009.
- [56] J. J. Bikerman. Theory of peeling through a hookean solid. *J. of Applied Physics*, 28(12):1484, 1957.
- [57] C Verdier and G Ravilly. *J. of Polymer Science: Part B: Polymer Physics*, 45:2113, 2007.
- [58] A. N. Gent and R. P. Petrich. Adhesion of viscoelastic materials to rigid substrates. *Proceedings of the Royal Society of London. Series A, Mathematical and Physical Science*, 310(1502):433, 1969.
- [59] S. Giannis, R. D. Adams, L. J. Clark, and M. A. Taylor. *Int. J. of Adhesion and Adhesives*, 28:158, 2008.
- [60] MH Wagner and J. Schaeffer. Rubbers and polymer melts: Universal aspects of nonlinear stress–strain relations. *Journal of Rheology*, 37:643, 1993.
- [61] J. Meissner. Polymer melt elongation, methods, results, and recent developments. *Polymer engineering and Science*, 27(8):537, 1987.
- [62] H. M. Laun and H Schuch. Transient elongational viscosities and drawability of polymer melts. *J. of Rheology*, 33(1):119, 1989.
- [63] A. Bach, H. K. Rasmussen, P. Longin, and O. hassager. Growth of non-axisymmetric disturbances of the free surface in the filament stretch rheometer: experiments and simulation. *J. of Non-Newtonian Fluid Mech.*, 108:163, 2002.
- [64] A. Kaye. College of aeronautics. *Cranheld*, Note no 134, 1962.
- [65] E.A. Kearsley Bernstein, B. and L.J. Zapas. Study of stress relaxation with finite strain. *Transactions of the Society of Rheology*, 7:391–410, 1963.
- [66] M.H. Wagner, P. Rubio, and H. Bastian. The molecular stress function model for polydisperse polymer melts with dissipative convective constraint release. *J. of Rheol.*, 45(6):1387, 2001.
- [67] PK Currie. Constitutive equations for polymer melts predicted by the Doi–Edwards and Curtiss–Bird kinetic theory models. *J. Non-Newtonian Fluid Mech*, 11:53–68, 1982.

- [68] R.C. Ball, M. Doi, S.F. Edwards, and M. Warner. Elasticity of entangled networks. *Polymer*, 22(8):1010–1018, August 1981.
- [69] Xiangjun Xing, Paul M. Goldbart, and Leo Radzihovsky. Thermal fluctuations and rubber elasticity. *Phys. Rev. Lett.*, 98(7):075502–4, February 2007.
- [70] Rasmus Hansen, Anne Ladegaard Skov, and Ole Hassager. Constitutive equation for polymer networks with phonon fluctuations. *Phys. Rev. E*, 77(1):011802–6, January 2008.
- [71] Ole Hassager, Susanne B. Kristensen, Johannes R. Larsen, and Jesper Neergaard. Inflation and instability of a polymeric membrane. *Journal of Non-Newtonian Fluid Mechanics*, 88(1-2):185–204, December 1999.
- [72] Henrik Koblitz Rasmussen, Jens Horslund Christensen, and Søren Gøttsche. Inflation of polymer melts into elliptic and circular cylinders. *Journal of Non-Newtonian Fluid Mechanics*, 93(2-3):245–263, October 2000.
- [73] H. K. Rasmussen. Time-dependent finite-element method for the simulation of three-dimensional viscoelastic flow with integral models. *Journal of Non-Newtonian Fluid Mechanics*, 84:217–232, 1999.
- [74] H. K. Rasmussen. Lagrangian viscoelastic flow computations using Rivlin-Sawyers constitutive model. *Journal of Non-Newtonian Fluid Mechanics*, 92:227–243, 2000.
- [75] H. K. Rasmussen. Lagrangian viscoelastic flow computations using a generalized molecular stress function model. *Journal of Non-Newtonian Fluid Mechanics*, 106:107–120, 2002.
- [76] J.M.R. Marín and H.K. Rasmussen. Lagrangian finite element method for the simulation of k-bkz fluids with third order accuracy. *Journal of Non-Newtonian Fluid Mechanics*, 156:177–188, 2009.
- [77] M. H. Wagner and J. Schaeffer. Assessment of non-linear strain measures for extensional and shearing flows of polymer melts. *Rheol. Acta*, 33:506–516, 1994.
- [78] K. Mortensen. Structural studies of aqueous solutions of PEO-PPO-PEO triblock copolymers, their micellar aggregates and mesophases; a small-angle neutron scattering study. *Journal of Physics Condensed Matter*, 8:103–124, 1996.
- [79] Henrik Koblitz Rasmussen, Philippe Laillé, and Kaijia Yu. Large amplitude oscillatory elongation flow. *Rheologica Acta*, 47(1):97–103, 2008.
- [80] Ole Hassager and Rasmus Hansen. Constitutive equations for the doiedwards model without independent alignment. Manuscript under preparation, September 2009.

- [81] C Tsenoglou. Rubber elasticity of cross-linked networks with trapped entanglements and dangling chains. *Macromolecules*, 22(1):284–289, 1989.
- [82] M.K. Jensen, A. Bach, O. Hassager, and A.L. Skov. Linear rheology of cross-linked polypropylene oxide as a pressure sensitive adhesive. *International Journal of Adhesion and Adhesives*, 2009.
- [83] T. Kawamura, K. Urayama, and S. Kohjiya. Multiaxial deformations of end-linked poly(dimethylsiloxane) networks. iii. effect of entanglement density on strain-energy density function. *Journal of Polymer Science Part B: Polymer Physics*, 40(24):2780–2790, 2002.
- [84] J.D. Schieber, J. Neergaard, and S. Gupta. A full-chain, temporary network model with sliplinks, chain-length fluctuations, chain connectivity and chain stretching. *J. Rheol.*, 47(1):213–233, January 2003.
- [85] J.D. Schieber. Fluctuations in entanglements of polymer liquids. *Journal of Chemical Physics*, 118(11):5162–, March 2003.
- [86] R.N. Khaliullin and J.D. Schieber. Self-consistent modeling of constraint release in a single-chain mean-field slip-link model. *Macromolecules*, 42(19):7504–7517, October 2009.
- [87] R.N. Khaliullin and J.D. Schieber. Analytic expressions for the statistics of the primitive-path length in entangled polymers. *Phys. Rev. Lett.*, 100(18):188302–4, May 2008.
- [88] M. Doi and J. Takimoto. Molecular modelling of entanglement. *Philosophical Transactions: Mathematical, Physical and Engineering Sciences*, 361(1805):641–652, Apr. 15, 2003.
- [89] S. T. Milner and T. C. B. McLeish. Reptation and contour-length fluctuations in melts of linear polymers. *Phys. Rev. Lett.*, 81(3):725–, July 1998.
- [90] M. Baumgaertel, A. Schausberger, and H.H. Winter. The relaxation of polymers with linear flexible chains of uniform length. *Rheologica Acta*, 29(5):400–408, 1990.
- [91] K Mortensen. PEO-PPO-PEO block polymer in aqueous solution: Micelle formation and crystallization. *Progress in Colloid and Polymer Science*, 91:69–69, 1993.
- [92] Y. Takahashi and H. Tadokoro. Structural studies of polyethers, $-(\text{CH}_2)_m\text{O}-$. X. crystal structure of poly (ethylene oxide). *Macromolecules*, 6(5):672–675, 1973.
- [93] W. Michalke, M. Lang, S. Kreitmeier, and D. G??ritz. Comparison of topological properties between end-linked and statistically cross-linked polymer networks. *Journal of Chemical Physics*, 117(13):6300–, October 2002.

- [94] Dhananjay M. Bhawe, Claude Cohen, and Fernando A. Escobedo. Formation and characterization of semiflexible polymer networks via monte carlo simulations. *Macromolecules*, 37(10):3924–3933, 2004.
- [95] Dhananjay M. Bhawe, Claude Cohen, and Fernando A. Escobedo. Effect of chain stiffness and entanglements on the elastic behavior of end-linked elastomers. *Journal of Chemical Physics*, 123(1):N.PAG–, July 2005.
- [96] Sachin Shanbhag and Ronald G. Larson. Chain retraction potential in a fixed entanglement network. *Phys. Rev. Lett.*, 94(7):076001–, February 2005.

Department of Chemical
and Biochemical Engineering

DTU Building 229
Søltofts Plads
DK-2800 Kgs. Lyngby